

1 A search for sparticles in zero lepton final states

2 Russell W. Smith

3 Submitted in partial fulfillment of the

4 requirements for the degree of

5 Doctor of Philosophy

6 in the Graduate School of Arts and Sciences

7 COLUMBIA UNIVERSITY

8 2016

9

© 2016

10

Russell W. Smith

11

All rights reserved

12

ABSTRACT

13

A search for sparticles in zero lepton final states

14

Russell W. Smith

15 TODO : Here's where your abstract will eventually go. The above text is all in the
16 center, but the abstract itself should be written as a regular paragraph on the page,
17 and it should not have indentation. Just replace this text.

Contents

19	Contents	i
20	1 Introduction	1
21	2 The Standard Model	5
22	2.1 Overview	5
23	2.2 Field Content	6
24	2.3 Deficiencies of the Standard Model	15
25	3 Supersymmetry	21
26	3.1 Supersymmetric theories : from space to superspace	21
27	3.2 Minimally Supersymmetric Standard Model	24
28	3.3 Phenomenology	30
29	3.4 How SUSY solves the problems with the SM	33
30	3.5 Conclusions	35
31	4 The Large Hadron Collider	37
32	4.1 Basics of Accelerator Physics	37
33	4.2 Accelerator Complex	39
34	4.3 Large Hadron Collider	41
35	4.4 Dataset Delivered by the LHC	43
36	5 The ATLAS detector	49

37	5.1	Magnets	50
38	5.2	Inner Detector	52
39	5.3	Calorimetry	56
40	5.4	Muon Spectrometer	61
41	5.5	Trigger System	66
42	6	Event Reconstruction	73
43	6.1	Primitive Object Reconstruction	73
44	6.2	Physics Object Reconstruction and Quality Identification	79
45	6.3	Maybe PFlow?	94
46	7	The Recursive Jigsaw Technique	95
47	7.1	Razor variables	95
48	7.2	SuperRazor variables	95
49	7.3	The Recursive Jigsaw Technique	95
50	7.4	Variables used in the search for zero lepton SUSY	95
51	8	Table of Contents Title	97
52	9	A search for supersymmetric particles in zero lepton final states with the Recursive Jigsaw Technique	99
54	9.1	Object reconstruction	99
55	9.2	Signal regions	100
56	9.3	Background estimation	100
57	10	Results	101
58	10.1	Statistical Analysis	101
59	10.2	Signal Region distributions	101
60	10.3	Pull Plots	101
61	10.4	Systematic Uncertainties	101

62	10.5 Exclusion plots	101
63	Conclusion	103
64	10.6 New Section	103
65	Bibliography	105
66	Quantum Field Theory and Symmetries	115
67	Quantum Field Theory	115
68	Symmetries	116
69	Local symmetries	118

Acknowledgements

Dedication

Introduction

74 Particle physics is a remarkably successful field of scientific inquiry. The ability to
 75 precisely predict the properties of a exceedingly wide range of physical phenomena,
 76 such as the description of the cosmic microwave background [1, 2], the understanding
 77 of the anomalous magnetic dipole moment of the electron [3, 4], and the measurement
 78 of the number of weakly-interacting neutrino flavors [5] is truly amazing.

79 The theory that has allowed this range of predictions is the *Standard Model*
 80 of particle physics (SM). The Standard Model combines the electroweak theory of
 81 Glashow, Weinberg, and Salam [6–8] with the theory of the strong interactions, as
 82 first envisioned by Gell-Mann and Zweig [9, 10]. This quantum field theory (QFT)
 83 contains a tiny number of particles, whose interactions describe phenomena up to at
 84 least the TeV scale. These particles are manifestations of the fields of the Standard
 85 Model, after application of the Higgs Mechanism. The particle content of the SM
 86 consists only of the six quarks, the six leptons, the four gauge bosons, and the scalar
 87 Higgs boson.

88 Despite its impressive range of described phenomena, the Standard Model has
 89 some theoretical and experimental deficiencies. The SM contains 26 free parameters
 90 ¹. It would be more theoretically pleasing to understand these free parameters in
 91 terms of a more fundamental theory. The major theoretical concern of the Standard
 92 Model, as it pertains to this thesis, is the *hierarchy problem*[11–15]. The light mass

¹This is the Standard Model corrected to include neutrino masses. These parameters are the fermion masses (6 leptons, 6 quarks), CKM and PMNS mixing angles (8 angles, 2 CP-violating phases), W/Z/Higgs masses (3), the Higgs field expectation value, and the couplings of the strong, weak, and electromagnetic forces (3 α_{force}).

of the Higgs boson (125 GeV) should be quadratically dependent on the scale of UV physics, due to the quantum corrections from high-energy physics processes. The most perplexing experimental issue is the existence of *dark matter*, as demonstrated by galactic rotation curves [16–22]. This data has shown that there exists additional matter which has not yet been seen interacting with the particles of the Standard Model. There is no particle in the SM which can act as a candidate for dark matter.

Both of these major issues, as well as numerous others, can be solved by the introduction of *supersymmetry* (SUSY) [15, 23–35]. In supersymmetric theories, each SM particles has a so-called *superpartner*, or sparticle partner, differing from given SM particle by 1/2 in spin. These theories solve the hierarchy problem, since the quantum corrections induced from the superpartners exactly cancel those induced by the SM particles. In addition, these theories are usually constructed assuming *R*–parity, which can be thought of as the “charge” of supersymmetry, with SM particles having $R = 1$ and sparticles having $R = -1$. In collider experiments, since the incoming SM particles have total $R = 1$, the resulting sparticles are produced in pairs. This produces a rich phenomenology, which is characterized by significant hadronic activity and large missing transverse energy (E_T^{miss}), which provide significant discrimination against SM backgrounds [36].

Despite the power of searches for supersymmetry where E_T^{miss} is a primary discriminating variable, there has been significant interest in the use of other variables to discriminate against SM backgrounds. These include searches employing variables such as αT , $M_{T,2}$, and the razor variables (M_R, R^2) [37–47]. In this thesis, we will present the first search for supersymmetry using the novel Recursive Jigsaw Reconstruction (RJR) technique. RJR can be considered the conceptual successor of the razor variables. We impose a particular final state “decay tree” on an events, which roughly corresponds to a simplified Feynmann diagram in decays containing weakly-interacting particles. We account for the missing degrees of freedom associated

120 to the weakly-interacting particles by a series of simplifying assumptions, which allow
121 us to calculate our variables of interest at each step in the decay tree. This allows an
122 unprecedented understanding of the internal structure of the decay and the ability to
123 construct additional variables to reject Standard Model backgrounds.

124 This thesis details a search for the superpartners of the gluon and quarks, the
125 gluino and squarks, in final states with zero leptons, with 13.3 fb^{-1} of data using the
126 ATLAS detector. We organize the thesis as follows. The theoretical foundations of
127 the Standard Model and supersymmetry are described in Chapters 2 and 3. The
128 Large Hadron Collider and the ATLAS detector are presented in Chapters 4 and 5.
129 Chapter 5 provides a detailed description of Recursive Jigsaw Reconstruction and a
130 description of the variables used for the particular search presented in this thesis.
131 Chapter 6 presents the details of the analysis, including details of the dataset, object
132 reconstruction, and selections used. In Chapter 7, the final results are presented;
133 since there is no evidence of a supersymmetric signal in the analysis, we present the
134 final exclusion curves in simplified supersymmetric models.

2.1 Overview

A Standard Model is another name for a theory of the internal symmetry group $SU(3)_C \otimes SU(2)_L \otimes U(1)_Y$, with its associated set of parameters. *The Standard Model* refers specifically to a Standard Model with the proper parameters to describe the universe. The SM is the culmination of years of work in both theoretical and experimental particle physics. **TODO: cite** In this thesis, we take the view that theorists construct a model with the field content and symmetries as inputs, and write down the most general Lagrangian consistent with those symmetries. Assuming this model is compatible with nature (in particular, the predictions of the model are consistent with previous experiments), experimentalists are responsible measuring the parameters of this model. This will be applicable for this chapter and the following one.

Additional theoretical background is in 10.6. The philosophy and notations are inspired by [48, 49].

₁₅₁ **2.2 Field Content**

The Standard Model field content is

$$\begin{aligned} \text{Fermions} &: Q_L(3, 2)_{+1/3}, U_R(3, 1)_{+4/3}, D_R(3, 1)_{-2/3}, L_L(1, 2)_{-1}, E_R(1, 1)_{-2} \\ \text{Scalar (Higgs)} &: \phi(1, 2)_{+1} \\ \text{Vector Fields} &: G^\mu(8, 1)_0, W^\mu(1, 3)_0, B^\mu(1, 1)_0 \end{aligned} \tag{2.1}$$

₁₅₂ where the $(A, B)_Y$ notation represents the irreducible representation under $SU(3)$
₁₅₃ and $SU(2)$, with Y being the electroweak hypercharge. Each of these fermion fields
₁₅₄ has an additional index, representing the three generation of fermions.

₁₅₅ We observed that Q_L, U_R , and D_R are triplets under $SU(3)_C$; these are the *quark*
₁₅₆ fields. The *color* group, $SU(3)_C$ is mediated by the *gluon* field $G^\mu(8, 1)_0$, which has
₁₅₇ 8 degrees of freedom. The fermion fields $L_L(1, 2)_{-1}$ and $E_R(1, 1)_{-2}$ are singlets under
₁₅₈ $SU(3)_C$; we call them the *lepton* fields.

₁₅₉ Next, we note the “left-handed” (“right-handed”) fermion fields, denoted by L (R)
₁₆₀ subscript, The left-handed fields form doublets under $SU(2)_L$. These are mediated
₁₆₁ by the three degrees of freedom of the “W” fields $W^\mu(1, 3)_0$. These fields only act
₁₆₂ on the left-handed particles of the Standard Model. This is the reflection of the
₁₆₃ “chirality” of the Standard Model; the left-handed and right-handed particles are
₁₆₄ treated differently by the electroweak forces. The right-handed fields, U_R, D_R , and
₁₆₅ E_R , are singlets under $SU(2)_L$.

₁₆₆ The $U(1)_Y$ symmetry is associated to the $B^\mu(1, 1)_0$ boson with one degree of
₁₆₇ freedom. The charge Y is known as the electroweak hypercharge.

₁₆₈ To better understand the phenomenology of the Standard Model, let us investigate
₁₆₉ each of the *sectors* of the Standard Model separately.

¹⁷⁰ **Electroweak sector**

The electroweak sector refers to the $SU(2)_L \otimes U(1)_Y$ portion of the Standard Model gauge group. Following our philosophy of writing all gauge-invariant and renormalizable terms, the electroweak Lagrangian can be written as

$$\mathcal{L} = W_a^{\mu\nu}W_a^\mu + B^{\mu\nu}B_{\mu\nu} + (D^\mu\phi)^\dagger D_\mu\phi - \mu^2\phi^\dagger\phi - \lambda(\phi^\dagger\phi)^2. \quad (2.2)$$

where $W_a^{\mu\nu}$ are the three ($a = 1, 2, 3$) gauge bosons associated to the $SU(2)_L$ gauge group, $B^{\mu\nu}$ is the one gauge boson of the $U(1)_Y$ gauge group, and ϕ is the complex Higgs multiplet. The covariant derivative D^μ is given by

$$D^\mu = \partial^\mu + \frac{ig}{2}W_a^\mu\sigma_a + \frac{ig'}{2}B^\mu \quad (2.3)$$

where $i\sigma_a$ are the Pauli matrices times the imaginary constant, which are the generators for $SU(2)_L$, and g and g' are the $SU(2)_L$ and $U(1)_Y$ coupling constants, respectively. The field strength tensors $W_a^{\mu\nu}$ and $B^{\mu\nu}$ are given by the commutator of the covariant derivative associated to each field

$$B^{\mu\nu} = \partial^\mu B^\nu - \partial^\nu B^\mu \quad (2.4)$$

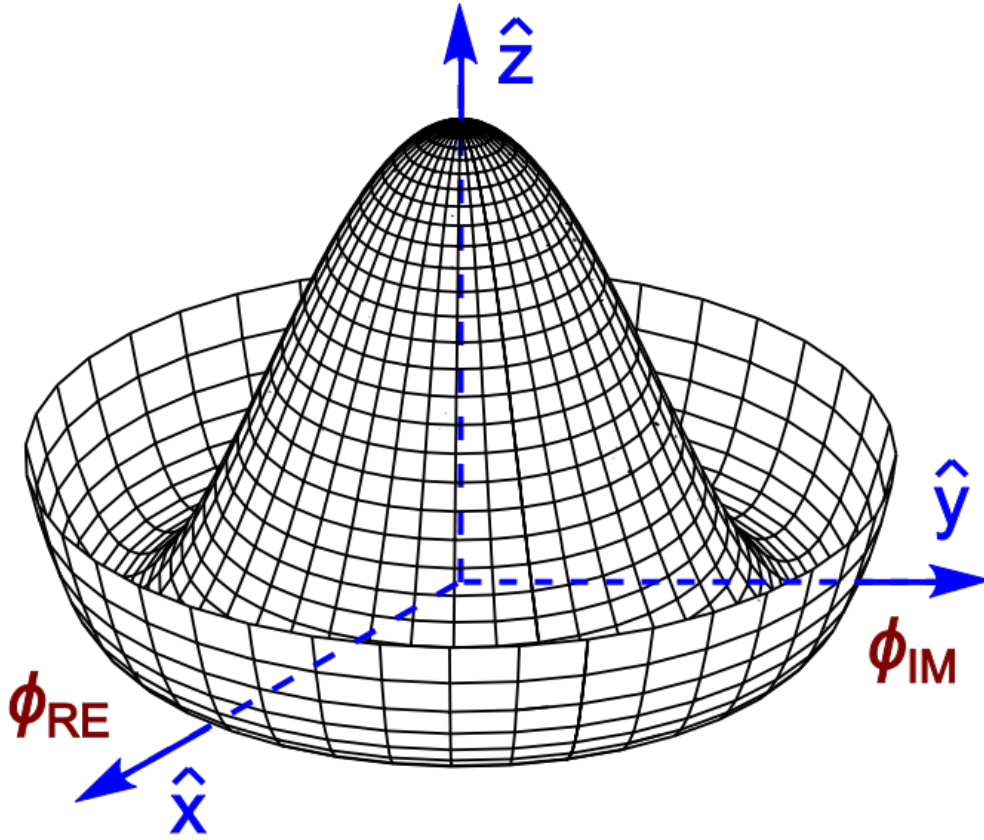
$$W_a^{\mu\nu} = \partial^\mu W_a^\nu - \partial^\nu W_a^\mu - g\epsilon_{abc}W_a^\mu W_b^\nu, \quad i = 1, 2, 3$$

¹⁷¹

¹⁷² The terms in the Lagrangian 2.2 proportional to μ^2 and λ make up the “Higgs
¹⁷³ potential” [50]. As normal (see Appendix 10.6), we restrict $\lambda > 0$ to guarantee our
¹⁷⁴ potential is bounded from below, and we also require $\mu^2 < 0$, which gives us the
¹⁷⁵ standard “sombrero” potential shown in 2.1.

This potential has infinitely many minima at $\langle \phi \rangle = \sqrt{2m/\lambda}$; the ground state is *spontaneously* broken by the choice of ground state, which induces a vacuum expectation value (VEV). Without loss of generality, we can choose the Higgs field ϕ to point in

Figure 2.1: Sombrero potential



the real direction, and write the Higgs field ϕ in the following form :

$$\phi = \frac{1}{\sqrt{2}} \exp\left(\frac{i}{v} \sigma_a \theta_a\right) \begin{pmatrix} 0 \\ v + h(x) \end{pmatrix}. \quad (2.5)$$

We choose a gauge to rotate away the dependence on θ_a , such that we can write simply

$$\phi = \frac{1}{\sqrt{2}} \begin{pmatrix} 0 \\ v + h(x) \end{pmatrix}. \quad (2.6)$$

Now, we can see how the masses of the vector bosons are generated from the application of the Higgs mechanism. We plug Eq.2.6 back into the electroweak Lagrangian, and only showing the relevant mass terms in the vacuum state where

$h(x) = 0$ see that (dropping the Lorentz indices) :

$$\begin{aligned}\mathcal{L}_M &= \frac{1}{8} \left| \begin{pmatrix} gW_3 + g'B & g(W_1 - iW_2) \\ g(W_1 + iW_2) & -gW_3 + g'B \end{pmatrix} \begin{pmatrix} 0 \\ v \end{pmatrix} \right|^2 \\ &= \frac{g^2 v^2}{8} \left[W_1^2 + W_2^2 + \left(\frac{g'}{g} B - W_3 \right)^2 \right]\end{aligned}\quad (2.7)$$

Defining the *Weinberg* angle $\tan(\theta_W) = g'/g$ and the following *physical* fields :

$$\begin{aligned}W^\pm &= \frac{1}{\sqrt{2}}(W_1 \mp iW_2) \\ Z^0 &= \cos \theta_W W_3 - \sin \theta_W B \\ A^0 &= \sin \theta_W W_3 + \cos \theta_W B\end{aligned}\quad (2.8)$$

we can write the piece of the Lagrangian associated to the vector boson masses as

$$\mathcal{L}_{M_V} = \frac{1}{4}g^2 v^2 W^+ W^- + \frac{1}{8}(g^2 + g'^2)v^2 Z^0 Z^0. \quad (2.9)$$

and we have the following values of the masses for the vector bosons :

$$\begin{aligned}m_W^2 &= \frac{1}{4}v^2 g^2 \\ m_Z^2 &= \frac{1}{4}v^2(g^2 + g'^2) \\ m_A^2 &= 0\end{aligned}\quad (2.10)$$

176 We thus see how the Higgs mechanism gives rise to the masses of the W^\pm and Z
 177 boson in the Standard Model; the mass of the photon is zero, as expected. The
 178 $SU(2)_L \otimes U(1)_Y$ symmetry of the initially massless $W_{1,2,3}$ and B fields is broken to
 179 the $U(1)_{EM}$. Of the four degrees of freedom in the complex Higgs doublet, three are
 180 “eaten” when we give mass to the W^\pm and Z_0 , while the other degree of freedom is
 181 the Higgs particle, as found in 2012 by the ATLAS and CMS collaborations [51, 52].

182 Quantum Chromodynamics

Quantum chromodynamics (or the theory of the *strong* force) characterizes the behavior of *colored* particles, collectively known as *partons*. The partons of the

Standard Model are the (fermionic) quarks, and the (bosonic) gluons. The strong force is governed by $SU(3)_C$, an unbroken symmetry in the Standard Model, which implies the gluon remains massless. Defining the covariant derivative for QCD as

$$D^\mu = \partial^\mu + ig_s G_a^\mu L_a, a = 1, \dots, 8 \quad (2.11)$$

where L_a are the generators of $SU(3)_C$, and g_s is the coupling constant of the strong force. The QCD Lagrangian then is given by

$$\mathcal{L}_{\text{QCD}} = i\bar{\psi}_f D_\mu \gamma^\mu \psi_f - \frac{1}{4} G_{a,\mu\nu} G_a^{\mu\nu} \quad (2.12)$$

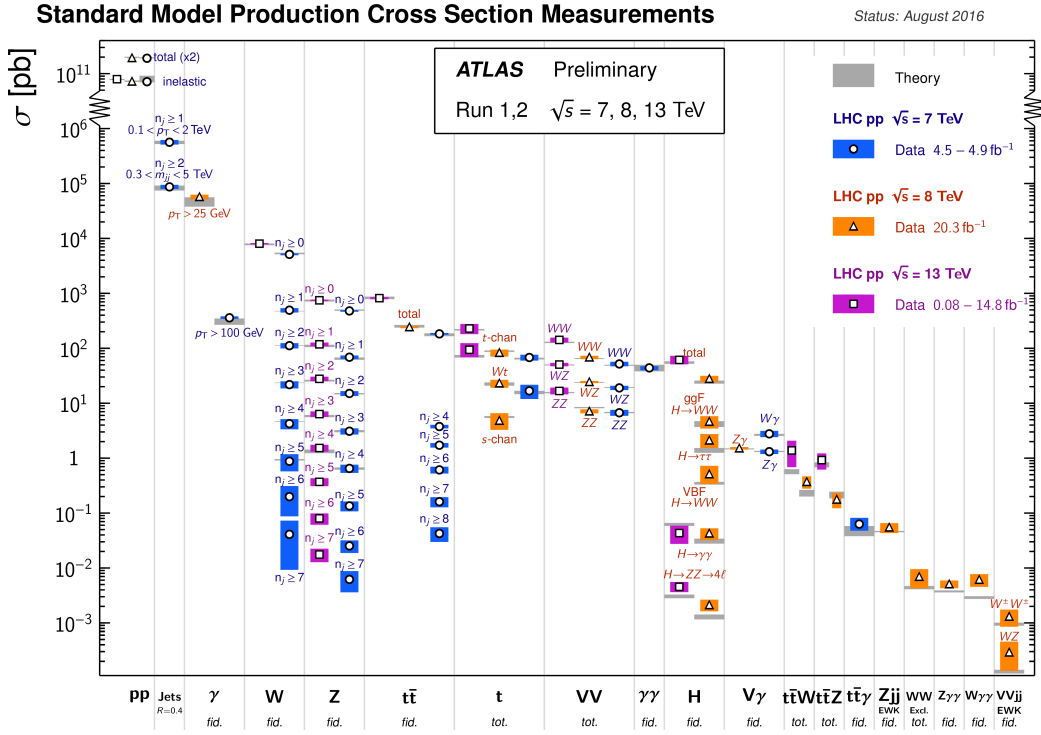
where the summation over f is for quarks *families*, and $G_a^{\mu\nu}$ is the gluon field strength tensor, given by

$$G_a^{\mu\nu} = \partial^\mu G_a^\nu - \partial^\nu G_a^\mu - g_s f^{abc} G_b^\mu G_c^\nu, a, b, c = 1, \dots, 8 \quad (2.13)$$

183 where f^{abc} are the structure constants of $SU(3)_C$, which are analogous to ϵ_{abc} for
 184 $SU(2)_L$. The kinetic term for the quarks is contained in the standard ∂_μ term, while
 185 the field strength term contains the interactions between the quarks and gluons, as
 186 well as the gluon self-interactions.

187 Written down in this simple form, the QCD Lagrangian does not seem much
 188 different from the QED Lagrangian, with the proper adjustments for the different
 189 group structures. The gluon is massless, like the photon, so one could naïvely expect
 190 an infinite range force, and it pays to understand why this is not the case. The
 191 reason for this fundamental difference is the gluon self-interactions arising in the
 192 field strength tensor term of the Lagrangian. This leads to the phenomena of *color*
 193 *confinement*, which describes how one only observes color-neutral particles alone in
 194 nature. In contrast to the electromagnetic force, particles which interact via the
 195 strong force experience a *greater* force as the distance between the particles increases.
 196 At long distances, the potential is given by $V(r) = -kr$. At some point, it is more
 197 energetically favorable to create additional partons out of the vacuum than continue

Figure 2.2: Cross-sections of various Standard Model processes



198 pulling apart the existing partons, and the colored particles undergo *fragmentation*.
199 This leads to *hadronization*. Bare quarks and gluons are actually observed as sprays
200 of hadrons (primarily kaons and pions); these sprays are known as *jets*, which are
201 what are observed by experiments.

202 It is important to recognize the importance of understanding these QCD inter-
203 actions in high-energy hadron colliders such as the LHC. Since protons are hadrons,
204 proton-proton collisions such as those produced by the LHC are primarily governed by
205 the processes of QCD. In particular, by far the most frequent process observed in LHC
206 experiments is dijet production from gluon-gluon interactions (see Fig.2.2). These
207 gluons that interact are part of the *sea* particles inside the proton; the simple $p = uud$
208 model does not apply. The main *valence* uud quarks are constantly interacting via
209 gluons, which can themselves radiate gluons or split into quarks, and so on. A more
210 useful understanding is given by the colloquially-known *bag* model [53, 54], where the
211 proton is seen as a “bag” of (in principle) infinitely many partons, each with energy

212 $E < \sqrt{s} = 6.5$ TeV. One then collides this (proton) bag with another, and views the
213 products of this very complicated collision, where calculations include many loops in
214 nonperturbative QCD calculations.

215 Fortunately, we are generally saved by the QCD factorization theorems [55]. This
216 allows one to understand the hard (i.e. short distance or high energy) $2 \rightarrow 2$ parton
217 process using the tools of perturbative QCD, while making series of approximations
218 known as a *parton shower* model to understand the additional corrections from
219 nonperturbative QCD. We will discuss the reconstruction of jets by experiments in
220 Ch.5.

221 Fermions

222 We will now look more closely at the fermions in the Standard Model [56].

223 As noted earlier in Sec.2.2, the fermions of the Standard Model can be first
224 distinguished between those that interact via the strong force (quarks) and those
225 which do not (leptons).

There are six leptons in the Standard Model, which can be placed into three
generations.

$$\begin{pmatrix} e \\ \nu_e \end{pmatrix}, \begin{pmatrix} \mu \\ \nu_\mu \end{pmatrix}, \begin{pmatrix} \tau \\ \nu_\tau \end{pmatrix} \quad (2.14)$$

226 There is the electron (e), muon (μ), and tau (τ), each of which has an associated
227 neutrino (ν_e, ν_μ, ν_τ). Each of the so-called charged (“electron-like”) leptons has
228 electromagnetic charge -1 , while the neutrinos all have $q_{EM} = 0$.

229 Often in an experimental context, lepton is used to denote the stable electron
230 and metastable muon, due to their striking experimental signatures. Taus are often
231 treated separately, due to their much shorter lifetime of $\tau_\tau \sim 10^{-13}s$; these decay
232 through hadrons or the other leptons, so often physics analyses at the LHC treat
233 them as jets or leptons, as will be done in this thesis.

234 As the neutrinos are electrically neutral, nearly massless, and only interact via the
 235 weak force, it is quite difficult to observe them directly. Since LHC experiments rely
 236 overwhelmingly on electromagnetic interactions to observe particles, the presence of
 237 neutrinos is not observed directly. Neutrinos are instead observed by the conservation
 238 of four-momentum in the plane transverse to the proton-proton collisions, known as
 239 *missing transverse energy*.

There are six quarks in the Standard Model : up, down, charm, strange, top, and bottom. Quarks are similar organized into three generations :

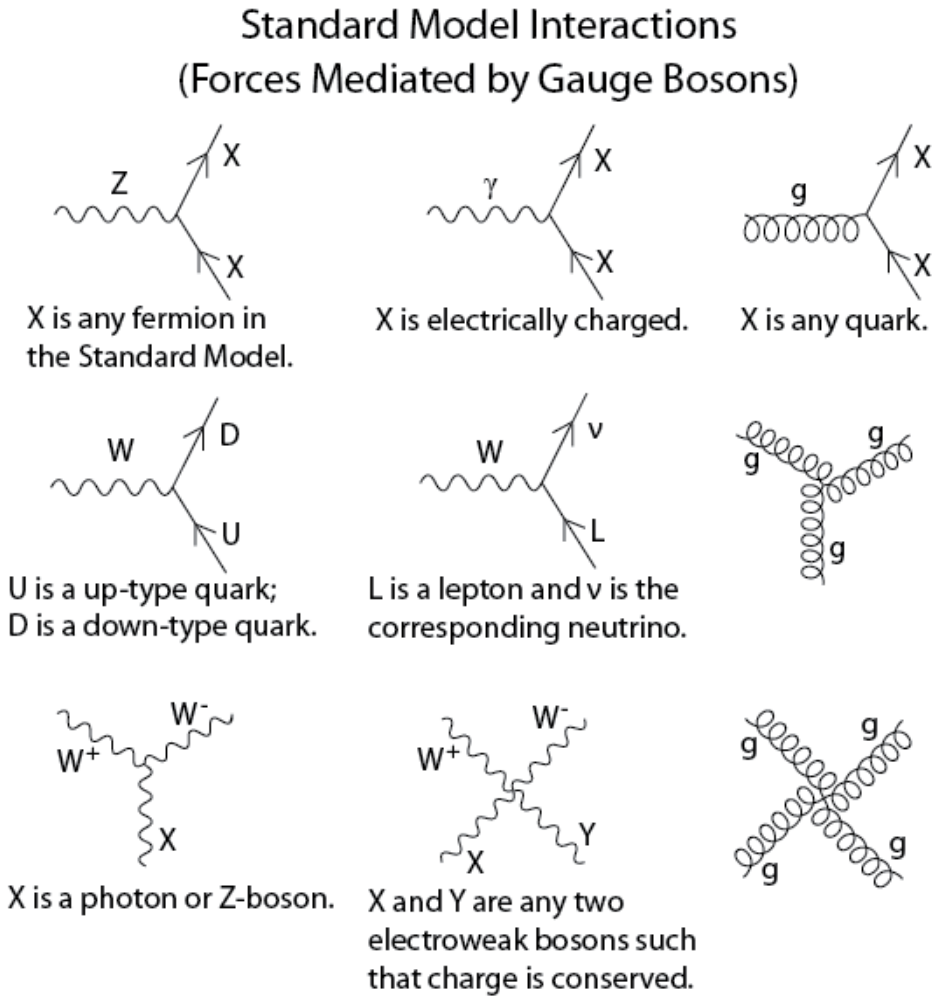
$$\begin{pmatrix} u \\ d \end{pmatrix}, \begin{pmatrix} c \\ s \end{pmatrix}, \begin{pmatrix} t \\ b \end{pmatrix} \quad (2.15)$$

240 where we speak of “up-like” quarks and “down-like” quarks.

241 Each up-like quark has charge $q_{up} = 2/3$, while the down-like quarks have $q_{down} =$
 242 $-1/3$. At the high energies of the LHC, one often makes the distinction between
 243 the light quarks (u, d, c, s), the bottom quark, and top quark. In general, due to
 244 the hadronization process described above, the light quarks, with masses $m_q < \sim$
 245 $1.5 GeV$ are indistinguishable by LHC experiments. Their hadronic decay products
 246 generally have long lifetimes and they are reconstructed as jets.¹. The bottom quark
 247 hadronizes primarily through the B -mesons, which generally travels a short distance
 248 before decaying to other hadrons. This allows one to distinguish decays via b —quarks
 249 from other jets; this procedure is known as *b-tagging* and will be discussed more in
 250 Ch.5. Due to its large mass, the top quark decays before it can hadronize; there
 251 are no bound states associated to the top quark. The top is of particular interest at
 252 the LHC; it has a striking signature through its most common decay mode $t \rightarrow Wb$.
 253 Decays via tops, especially $t\bar{t}$ are frequently an important signal decay mode, or an
 254 important background process.

¹In some contexts, charm quarks are also treated as a separate category, although it is quite difficult to distinguish charm quarks from the other light quarks.

Figure 2.3: The interactions of the Standard Model



255 Interactions in the Standard Model

256 We briefly overview the entirety of the fundamental interactions of the Standard
257 Model; these can also be found in [2.3](#).

258 The electromagnetic force, mediated by the photon, interacts with via a three-
259 point coupling all charged particles in the Standard Model. The photon thus interacts
260 with all the quarks, the charged leptons, and the charged W^\pm bosons.

261 The weak force is mediated by three particles : the W^\pm and the Z^0 . The Z^0 can
262 interact with all fermions via a three-point coupling. A real Z_0 can thus decay to

263 a fermion-antifermion pair of all SM fermions except the top quark, due to its large
264 mass. The W^\pm has two important three-point interactions with fermions. First, the
265 W^\pm can interact with an up-like quark and a down-like quark; an important example
266 in LHC experiments is $t \rightarrow Wb$. The coupling constants for these interactions are
267 encoded in the unitary matrix known as the Cabibbo–Kobayashi–Maskawa (CKM)
268 matrix [57, 58], and are generally known as flavor-changing interactions. Secondly,
269 the W^\pm interacts with a charged lepton and its corresponding neutrino. In this case,
270 the unitary matrix that corresponds to CKM matrix for quarks is the identity matrix,
271 which forbids (fundamental) vertices such as $\mu \rightarrow We$. For leptons, instead this is
272 a two-step process : $\mu \rightarrow \nu_m u W \rightarrow \nu_m u \bar{\nu}_e e$. Finally, there are the self-interactions
273 of the weak gauge bosons. There is a three-point and four-point interaction; all
274 combinations are allowed which conserve electric charge.

275 The strong force is mediated by the gluon, which as discussed above also carries
276 the strong color charge. There is the fundamental three-point interaction, where a
277 quark radiates a gluon. Additionally, there are the three-point and four-point gluon-
278 only interactions.

279 2.3 Deficiencies of the Standard Model

280 At this point, it is quite easy to simply rest on our laurels. This relatively simple
281 theory is capable of explaining a very wide range of phenomena, which ultimately
282 break down only to combinations of nine diagrams shown in Fig.2.3. Unfortunately,
283 there are some unexplained problems with the Standard Model. We cannot go
284 through all of the potential issues in this thesis, but we will motivate the primary
285 issues which naturally lead one to *supersymmetry*, as we will see in Ch.3.

The Standard Model has many free parameters; see Table 2.1. In general, we prefer models with less free parameters. A great example of this fact, and the primary

Table 2.1: Parameters of the Standard Model. For values dependent on the renormalization scheme, we use a combination of the on-shell normalization scheme [59–62] and modified minimal subtraction scheme with $m_{\bar{MS}}$ as indicated in the table[63]

m_e	Electron mass	511 keV
m_μ	Muon mass	105.7 MeV
m_τ	Tau mass	1.78 GeV
m_u	Up quark mass	1.9 MeV ($m_{\bar{MS}} = 2\text{GeV}$)
m_d	Down quark mass	4.4 MeV ($m_{\bar{MS}} = 2\text{GeV}$)
m_s	Strange quark mass	87 MeV ($m_{\bar{MS}} = 2\text{GeV}$)
m_c	Charm quark mass	1.32 GeV ($m_{\bar{MS}} = m_c$)
m_b	Bottom quark mass	4.24 GeV ($m_{\bar{MS}} = m_b$)
m_t	Top quark mass	172.7 GeV (on-shell renormalization)
θ_{12} CKM	12-mixing angle	13.1°
θ_{23} CKM	23-mixing angle	2.4°
θ_{13} CKM	13-mixing angle	0.2°
δ CKM	CP-violating Phase	0.995
g'	U(1) gauge coupling	0.357 ($m_{\bar{MS}} = m_Z$)
g	SU(2) gauge coupling	0.652 ($m_{\bar{MS}} = m_Z$)
g_s	SU(3) gauge coupling	1.221 ($m_{\bar{MS}} = m_Z$)
θ_{QCD}	QCD vacuum angle	~0
VEV	Higgs vacuum expectation value	246 GeV
m_H	Higgs mass	125 GeV

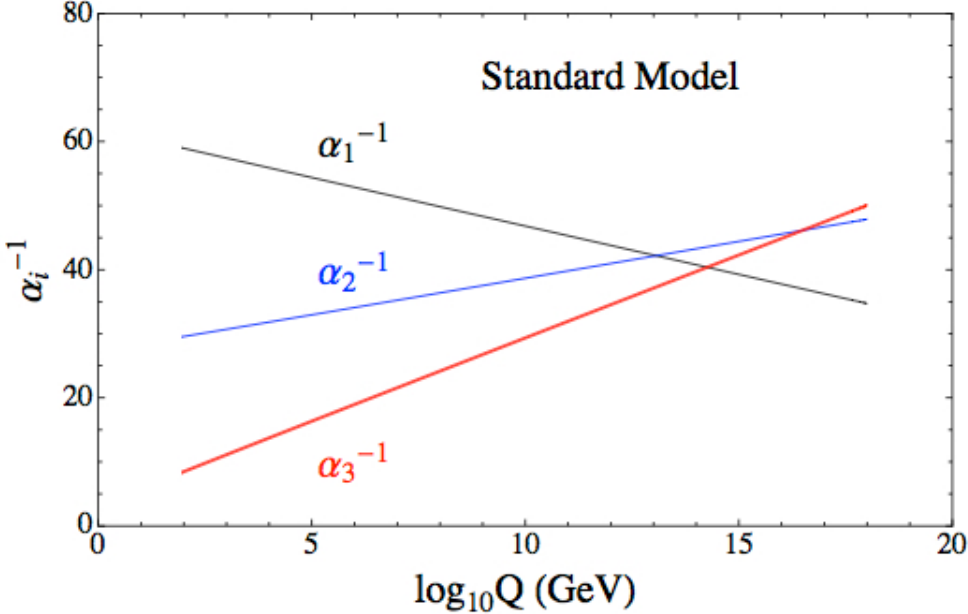
experimental evidence for EWSB, is the relationship between the couplings of the weak force and the masses of the gauge bosons of the weak force :

$$\rho \equiv \frac{m_W^2}{m_Z^2 \cos^2 \theta_W} \stackrel{?}{=} 1 \quad (2.16)$$

where ? indicates that this is a testable prediction of the Standard Model (in particular, that the gauge bosons gain mass through EWSB). This relationship has been measured within experimental and theoretical predictions. We would like to produce additional such relationships, which would exist if the Standard Model is a low-energy approximation of some other theory.

An additional issue is the lack of *gauge coupling unification*. The couplings of any quantum field theory “run” as a function of the distance scales (or inversely, energy scales) of the theory. The idea is closely related to the unification of the

Figure 2.4: The running of Standard Model gauge couplings. The Standard Model couplings do not unify at high energies, which indicates it cannot completely describe nature through the Planck scale.

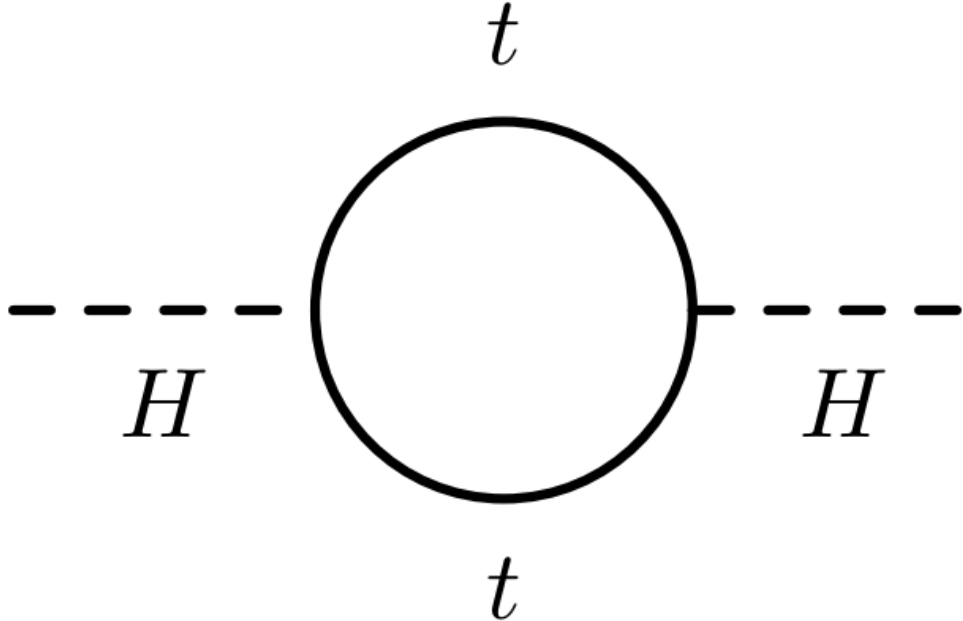


294 electromagnetic and weak forces at the so-called *electroweak scale* of $O(100 \text{ GeV})$.
 295 One would hope this behavior was repeated between the electroweak forces and the
 296 strong force at some suitable energy scale. The Standard Model does automatically
 297 not exhibit this behavior, as we can see in Fig.2.4.

The most significant problem with the Standard Model is the *hierarchy problem*. In its most straightforward incarnation, the Higgs scalar field is subject to quantum corrections through loop diagrams, as shown in Fig.2.5. For demonstration, we use the contributions from the top quark, since the top quark has the largest Higgs Yukawa coupling due to its large mass. In general, we should expect these corrections to be quadratically dependent on the scale of the ultraviolet physics, Λ . Briefly assume there is no new physics before the Planck scale of gravity, $\Lambda_{\text{Planck}} = 10^{19} \text{ GeV}$. In this case, we expect the corrections to the Higgs mass like

$$\delta m_H^2 \approx \left(\frac{m_t}{8\pi^2 \langle \phi \rangle_{VEV}} \right)^2 \Lambda_{\text{Planck}}^2. \quad (2.17)$$

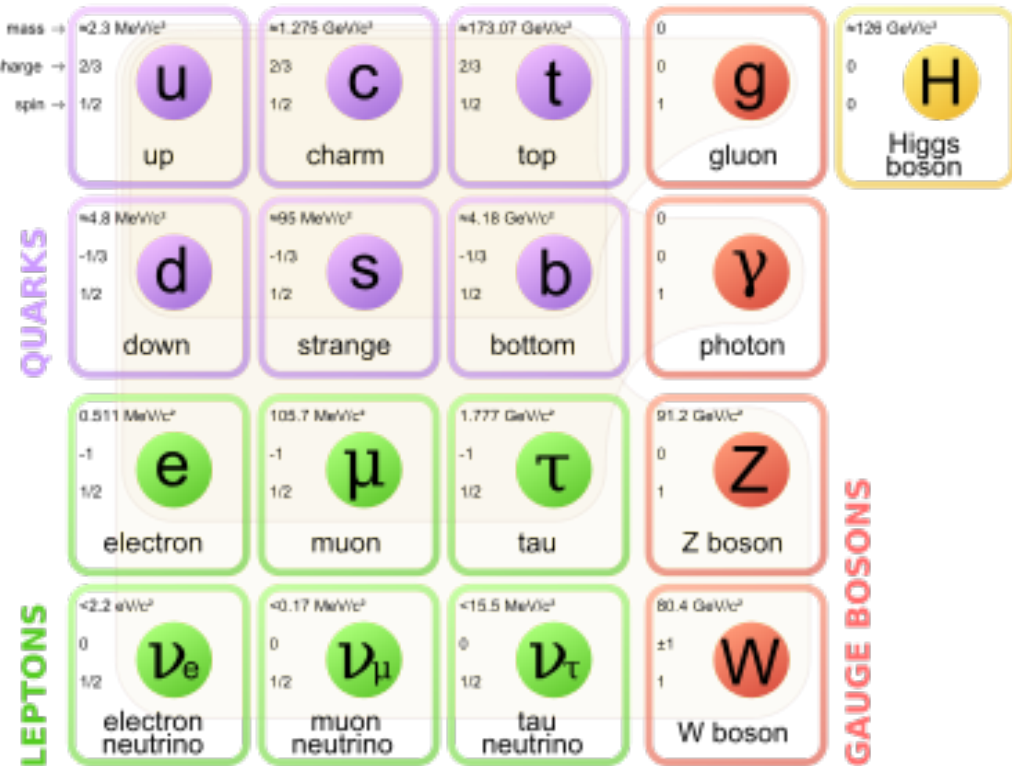
Figure 2.5: The dominant quantum loop correction to the Higgs mass in the Standard Model.



298 To achieve the miraculous cancellation required to get the observed Higgs mass of
299 125 GeV, one needs to then set the bare Higgs mass m_0 , our input to the Standard
300 Model Lagrangian, itself to a *precise* value $\sim 10^{19}$ GeV. This extraordinary level of
301 parameter finetuning is quite undesirable, and within the framework of the Standard
302 Model, there is little that can be done to alleviate this issue.

303 An additional concern, of a different nature, is the lack of a *dark matter* candidate
304 in the Standard Model. Dark matter was discovered by observing galactic rotation
305 curves, which showed that much of the matter that interacted gravitationally was
306 invisible to our (electromagnetic) telescopes [16–22]. The postulation of the existence
307 of dark matter, which interacts at least through gravity, allows one to understand
308 these galactic rotation curves. Unfortunately, no particle in the Standard Model could
309 possibly be the dark matter particle. The only candidate truly worth another look is
310 the neutrino, but it has been shown that the neutrino content of the universe is simply
311 too small to explain the galactic rotation curves [22, 64]. The experimental evidence

Figure 2.6: Particles of the Standard Model



312 from the galactic rotations curves thus show there *must* be additional physics beyond
 313 the Standard Model, which is yet to be understood.

314 In the next chapter, we will see how these problems can be alleviated by the theory
 315 of supersymmetry.

Supersymmetry

318 This chapter will introduce supersymmetry (SUSY) [15, 23–35]. We will begin by
 319 introducing the concept of a *superspace*, and discuss some general ingredients of
 320 supersymmetric theories. This will include a discussion of how the problems with the
 321 Standard Model described in Ch.2 are naturally fixed by these theories.

322 The next step is to discuss the particle content of the *Minimally Supersymmetric*
 323 *Standard Model* (MSSM). As its name implies, this theory contains the minimal
 324 additional particle content to make Standard Model supersymmetric. We then discuss
 325 the important phenomenological consequences of this theory, especially as it would
 326 be observed in experiments at the LHC.

327 **3.1 Supersymmetric theories : from space to
 328 superspace**

329 **Coleman-Mandula “no-go” theorem**

330 We begin the theoretical motivation for supersymmetry by citing the “no-go” theorem
 331 of Coleman and Mandula [65]. This theorem forbids *spin-charge unification*; it
 332 states that all quantum field theories which contain nontrivial interactions must be
 333 a direct product of the Poincaré group of Lorentz symmetries, the internal product
 334 from of gauge symmetries, and the discrete symmetries of parity, charge conjugation,
 335 and time reversal. The assumptions which go into building the Coleman-Mandula

theorem are quite restrictive, but there is one unique way out, which has become known as *supersymmetry* [26, 66]. In particular, we must introduce a *spinorial* group generator Q . Alternatively, and equivalently, this can be viewed as the addition of anti-commuting coordinates; space plus these new anti-commuting coordinates is then called *superspace* [67]. We will not investiage this view in detail, but it is also a quite intuitive and beautiful way to construct supersymmetry[15].

342 Supersymmetry transformations

343 A *supersymmetric* transformation Q transforms a bosonic state into a fermionic state,
 344 and vice versa :

$$Q |\text{Fermion}\rangle = |\text{Boson}\rangle \quad (3.1)$$

$$Q |\text{Boson}\rangle = |\text{Fermion}\rangle \quad (3.2)$$

To ensure this relation holds, Q must be an anticommuting spinor. Additionally, since spinors are inherently complex, Q^\dagger must also be a generator of the supersymmetry transformation. Since Q and Q^\dagger are spinor objects (with $s = 1/2$), we can see that supersymmetry must be a spacetime symmetry. The Haag-Lopuszanski-Sohnius extension [66] of the Coleman-Mandula theorem [65] is quite restrictive about the forms of such a symmetry. Here, we simply write the (anti-) commutation relations [15] :

$$Q_\alpha, Q_{\dot{\alpha}}^\dagger = -2\sigma_{\alpha\dot{\alpha}\mu} P_\mu \quad (3.3)$$

$$Q_\alpha, Q_{\dot{\beta}} = Q_{\dot{\alpha}}^\dagger, Q_{\dot{\beta}}^\dagger = 0 \quad (3.4)$$

$$[P^\mu, Q_\alpha] = [P^\mu, Q_{\dot{\alpha}}^\dagger] = 0 \quad (3.5)$$

345 **Supermultiplets**

346 In a supersymmetric theory, we organize single-particle states into irreducible
347 representations of the supersymmetric algebra which are known as *supermultiplets*.
348 Each supermultiplet contains a fermion state $|F\rangle$ and a boson state $|B\rangle$; these two
349 states are the known as *superpartners*. These are related by some combination of
350 Q and Q^\dagger , up to a spacetime transformation. Q and Q^\dagger commute with the mass-
351 squared operator $-P^2$ and the operators corresponding to the gauge transformations
352 [15]; in particular, the gauge interactions of the Standard Model. In an unbroken
353 supersymmetric theory, this means the states $|F\rangle$ and $|B\rangle$ have exactly the same mass,
354 electromagnetic charge, electroweak isospin, and color charges. One can also prove
355 [15] that each supermultiplet contains the exact same number of bosonic (n_B) and
356 fermion (n_F) degrees of freedom. We now explore the possible types of supermultiples
357 one can find in a renormalizable supersymmetric theory.

358 Since each supermultiplet must contain a fermion state, the simplest type of
359 supermultiplet contains a single Weyl fermion state ($n_F = 2$) which is paired with
360 $n_B = 2$ scalar bosonic degrees of freedom. This is most conveniently constructed as
361 single complex scalar field. We call this construction a *scalar supermultiplet* or *chiral*
362 *supermultiplet*. The second name is indicative; only chiral supermultiplets can contain
363 fermions whose right-handed and left-handed components transform differently under
364 the gauge interactions (as of course happens in the Standard Model).

365 The second type of supermultiplet we construct is known as a *gauge* supermul-
366 tiplet. We take a spin-1 gauge boson (which must be massless due to the gauge
367 symmetry, so $n_B = 2$) and pair this with a single massless Weyl spinor¹. The gauge
368 bosons transform as the adjoint representation of the their respective gauge groups;
369 their fermionic partners, which are known as gauginos, must also. In particular,
370 the left-handed and right-handed components of the gaugino fermions have the same

¹Choosing an $s = 3/2$ massless fermion leads to nonrenormalizable interactions.

371 gauge transformation properties.

372 Excluding gravity, this is the entire list of supermultiplets which can participate
373 in renormalizable interactions in what is known as $N = 1$ supersymmetry. This
374 means there is only one copy of the supersymmetry generators Q and Q^\dagger . This is
375 essentially the only “easy” phenomenological choice, since it is the only choice in four
376 dimensions which allows for the chiral fermions and parity violations built into the
377 Standard Model, and we will not look further into $N > 1$ supersymmetry in this thesis.

378 The primary goal, after understanding the possible structures of the multiplets
379 above, is to fit the Standard Model particles into a multiplet, and therefore make
380 predictions about their supersymmetric partners. We explore this in the next section.

381 **3.2 Minimally Supersymmetric Standard Model**

382 To construct what is known as the MSSM [[susyPrimer](#) , 68–71], we need a few
383 ingredients and assumptions. First, we match the Standard Model particles with
384 their corresponding superpartners of the MSSM. We will also introduce the naming
385 of the superpartners (also known as *sparticles*). We discuss a very common additional
386 restraint imposed on the MSSM, known as R –parity. We also discuss the concept of
387 soft supersymmetry breaking and how it manifests itself in the MSSM.

388 **Chiral supermultiplets**

389 The first thing we deduce is directly from Sec.???. The bosonic superpartners
390 associated to the quarks and leptons *must* be spin 0, since the quarks and leptons must
391 be arranged in a chiral supermultiplet. This is essentially the note above, since the
392 chiral supermultiplet is the only one which can distinguish between the left-handed
393 and right-handed components of the Standard Model particles. The superpartners of
394 the quarks and leptons are known as *squarks* and *sleptons*, or *sfermions* in aggregate.

395 (for ‘‘scalar quarks’’, ‘‘scalar leptons’’, and ‘‘scalar fermion’’²). The ‘‘s-’’ prefix
 396 can also be added to the individual quarks i.e. *selectron*, *sneutrino*, and *stop*. The
 397 notation is to add a \sim over the corresponding Standard Model particle i.e. \tilde{e} , the
 398 selectron is the superpartner of the electron. The two-component Weyl spinors of the
 399 Standard Model must each have their own (complex scalar) partner i.e. e_L, e_R have
 400 two distinct partners : \tilde{e}_L, \tilde{e}_R . As noted above, the gauge interactions of any of the
 401 sfermions are identical to those of their Standard Model partners.

Due to the scalar nature of the Higgs, it must obviously lie in a chiral supermultiplet. To avoid gauge anomalies and ensure the correct Yukawa couplings to the quarks and leptons[15], we must add additional Higgs bosons to any supersymmetric theory. In the MSSM, we have two chiral supermultiplets. The SM (SUSY) parts of the multiplets are denoted $H_u(\tilde{H}_u)$ and $H_d(\tilde{H}_d)$. Writing out H_u and H_d explicitly:

$$H_u = \begin{pmatrix} H_u^+ \\ H_u^0 \end{pmatrix} \quad (3.6)$$

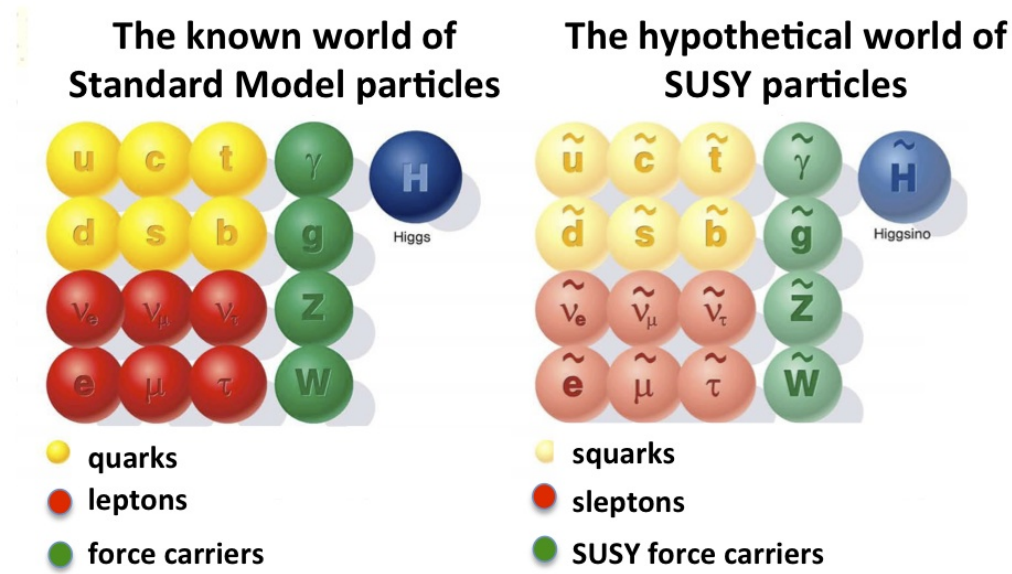
$$H_d = \begin{pmatrix} H_d^0 \\ H_d^- \end{pmatrix} \quad (3.7)$$

(3.8)

402 we see that H_u looks very similar to the SM Higgs with $Y = 1$, and H_d is symmetric
 403 to this with $+ \rightarrow -$, with $Y = -1$. The SM Higgs boson, h_0 , is a linear superposition
 404 of the neutral components of these two doublets. The SUSY parts of the Higgs
 405 multiplets, \tilde{H}_u and \tilde{H}_d , are each left-handed Weyl spinors. For generic spin-1/2
 406 sparticles, we add the ‘‘-ino’’ suffix. We then call the partners of the two Higgs
 407 collectively the *Higgsinos*.

²The last one should probably have bigger scare quotes.

Figure 3.1: Particles of the MSSM



408 Gauge supermultiplets

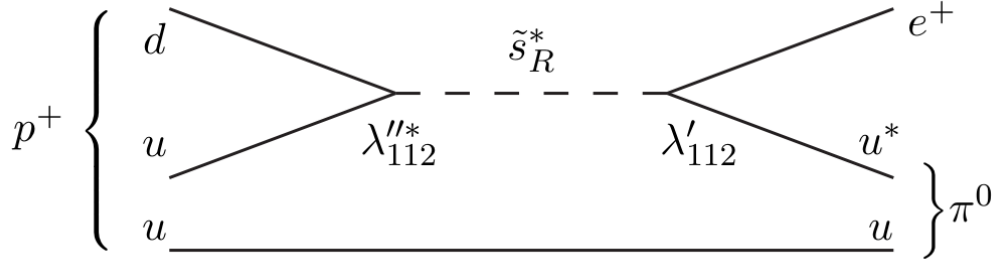
409 The superpartners of the gauge bosons must all be in gauge supermultiplets since
 410 they contain a spin-1 particle. Collectively, we refer to the superpartners of the
 411 gauge bosons as the gauginos.

412 The first gauge supermultiplet contains the gluon, and its superpartner, which is
 413 known as the *gluino*, denoted \tilde{g} . The gluon is of course the SM mediator of $SU(3)_C$;
 414 the gluino is also a colored particle, subject to $SU(3)_C$. From the SM before EWSB,
 415 we have the four gauge bosons of the electroweak symmetry group $SU(2)_L \otimes U(1)_Y$:
 416 $W^{1,2,3}$ and B^0 . The superpartners of these particles are thus the *winos* $W^{\tilde{1},\tilde{2},\tilde{3}}$ and
 417 *bino* \tilde{B}^0 , where each is placed in another gauge supermultiplet with its corresponding
 418 SM particle. After EWSB, without breaking supersymmetry, we would also have the
 419 zino \tilde{Z}^0 and photino $\tilde{\gamma}$.

420 The entire particle content of the MSSM can be seen in Fig.3.1.

421 At this point, it's important to take a step back. Where are these particles?
 422 As stated above, supersymmetric theories require that the masses and all quantum

Figure 3.2: This Feynmann diagram shows how proton decay is induced in the MSSM, if one does not impose R -parity.



423 numbers of the SM particle and its corresponding sparticle are the same. Of course,
 424 we have not observed a selectron, squark, or wino. The answer, as it often is, is that
 425 supersymmetry is *broken* by the vacuum state of nature [15].

426 **R -parity**

This section is a quick aside to the general story. R – parity refers to an additional discrete symmetry which is often imposed on supersymmetric models. For a given particle state, we define

$$R = (-1)^{3(B-L)+2s} \quad (3.9)$$

427 where B, L is the baryon (lepton) number and s is the spin. The imposition of
 428 this symmetry forbids certain terms from the MSSM Lagrangian that would violate
 429 baryon and/or lepton number. This is required in order to prevent proton decay, as
 430 shown in Fig.3.2³. .

431 In supersymmetric models, this is a \mathbb{Z}_2 symmetry, where SM particles have $R = 1$
 432 and sparticles have $R = -1$. We will take R – parity as part of the definition of
 433 the MSSM. We will discuss later the *drastic* consequences of this symmetry on SUSY
 434 phenomenology

³Proton decay can actually be prevented by allowing only one of the four potential R-parity violating terms to survive.

435 **Soft supersymmetry breaking**

The fundamental idea of *soft* supersymmetry breaking[15, 34, 35, 72, 73] is that we would like to break supersymmetry without reintroducing the quadratic divergences we discussed at the end of Chapter 2. We write the Lagrangian in a form :

$$\mathcal{L}_{\text{MSSM}} = \mathcal{L}_{\text{SUSY}} + \mathcal{L}_{\text{soft}} \quad (3.10)$$

436 In this sense, the symmetry breaking is “soft”, since we have separated out the
 437 completely symmetric terms from those soft terms which will not allow the quadratic
 438 divergences to the Higgs mass.

439 The explicitly allowed terms in the soft-breaking Lagrangian are [35].

- 440 • Mass terms for the scalar components of the chiral supermultipletss
 441 • Mass terms for the Weyl spinor components of the gauge supermultipletss
 442 • Trilinear couplings of scalar components of chiral supermultiplets

In particular, using the field content described above for the MSSM, the softly-broken portion of the MSSM Lagrangian can be written

$$\mathcal{L}_{\text{soft}} = -\frac{1}{2} \left(M_3 \tilde{g} \tilde{g} + M_2 \tilde{W} \tilde{W} + M_1 \tilde{B} \tilde{B} + c.c. \right) \quad (3.11)$$

$$- \left(\tilde{u} a_u \tilde{Q} H_u - \tilde{d} a_d \tilde{Q} H_d - \tilde{e} a_e \tilde{L} H_d + c.c. \right) \quad (3.12)$$

$$- \tilde{Q}^\dagger m_Q^2 \tilde{Q} - \tilde{L}^\dagger m_L^2 \tilde{L} - \tilde{u} m_u^2 \tilde{u}^\dagger - \tilde{d} m_d^2 \tilde{d}^\dagger - \tilde{e} m_e^2 \tilde{e}^\dagger \quad (3.13)$$

$$- m_{H_u}^2 H_u^* H_u - m_{H_d}^2 H_d^* H_d - (b H_u H_d + cc). \quad (3.14)$$

443 where we have introduced the following notations :

444 1. M_3, M_2, M_1 are the gluino, wino, and bino masses.

445 2. a_u, a_d, a_e are complex 3×3 matrices in family space.

446 3. $m_Q^2, m_u^2, m_d^2, m_L^2, m_e^2$ are hermitian 3×3 matrices in family space.

447 4. $m_{H_u}^2, m_{H_d}^2, b$ are the SUSY-breaking contributions to the Higgs potential.

448 We have written matrix terms without any sort of additional notational decoration
 449 to indicate their matrix nature, and we now show why. The first term 1 are
 450 straightforward; these are just the straightforward mass terms for these fields. There
 451 are strong constraints on the off-diagonal terms for the matrices of 2 [74, 75]; for
 452 simplicity, we will assume that each $a_i, i = u, d, e$ is proportional to the Yukawa
 453 coupling matrix : $a_i = A_{i0}y_i$. The matrices in ?? can be similarly constrained by
 454 experiments [68, 75–82] Finally, we assume that the elements 4 contributing to the
 455 Higgs potential as well as all of the 1 terms must be real, which limits the possible
 456 CP-violating interactions to those of the Standard Model. We thus only consider
 457 flavor-blind, CP-conserving interactions within the MSSM.

The important mixing for mass and gauge interaction eigenstates in the MSSM occurs within electroweak sector, in a process akin to EWSB in the Standard Model. The neutral portions of the Higgsinos doublets and the neutral gauginos ($\tilde{H}_u^0, \tilde{H}_d^0, \tilde{B}^0, \tilde{W}^0$) of the gauge interaction basis mix to form what are known as the *neutralinos* of mass basis :

$$M_{\tilde{\chi}} = \begin{pmatrix} M_1 & 0 & -c_\beta s_W m_Z & s_\beta s_W m_Z \\ 0 & M_2 & c_\beta c_W m_Z & -s_\beta c_W m_Z \\ -c_\beta s_W m_Z & c_\beta c_W m_Z & 0 & -\mu \\ s_\beta s_W m_Z & -s_\beta c_W m_Z & -\mu & 0 \end{pmatrix} \quad (3.15)$$

458 where $s(c)$ are the sine and cosine of angles related to EWSB, which introduced
 459 masses to the gauginos and higgsinos. Diagonalization of this matrix gives the four
 460 neutralino mass states, listed without loss of generality in order of increasing mass :
 461 $\tilde{\chi}_{1,2,3,4}^0$.

462 The neutralinos, especially the lightest neutralino $\tilde{\chi}_1^0$, are important ingredients
 463 in SUSY phenomenology.

464 The same process can be done for the electrically charged gauginos with
465 the charged portions of the Higgsino doublets along with the charged winos
466 ($\tilde{H}_u^+, \tilde{H}_d^+, \tilde{W}^+, \tilde{W}^-$). This leads to the *charginos*, again in order of increasing mass
467 : $\tilde{\chi}_{1,2}^\pm$.

468

3.3 Phenomenology

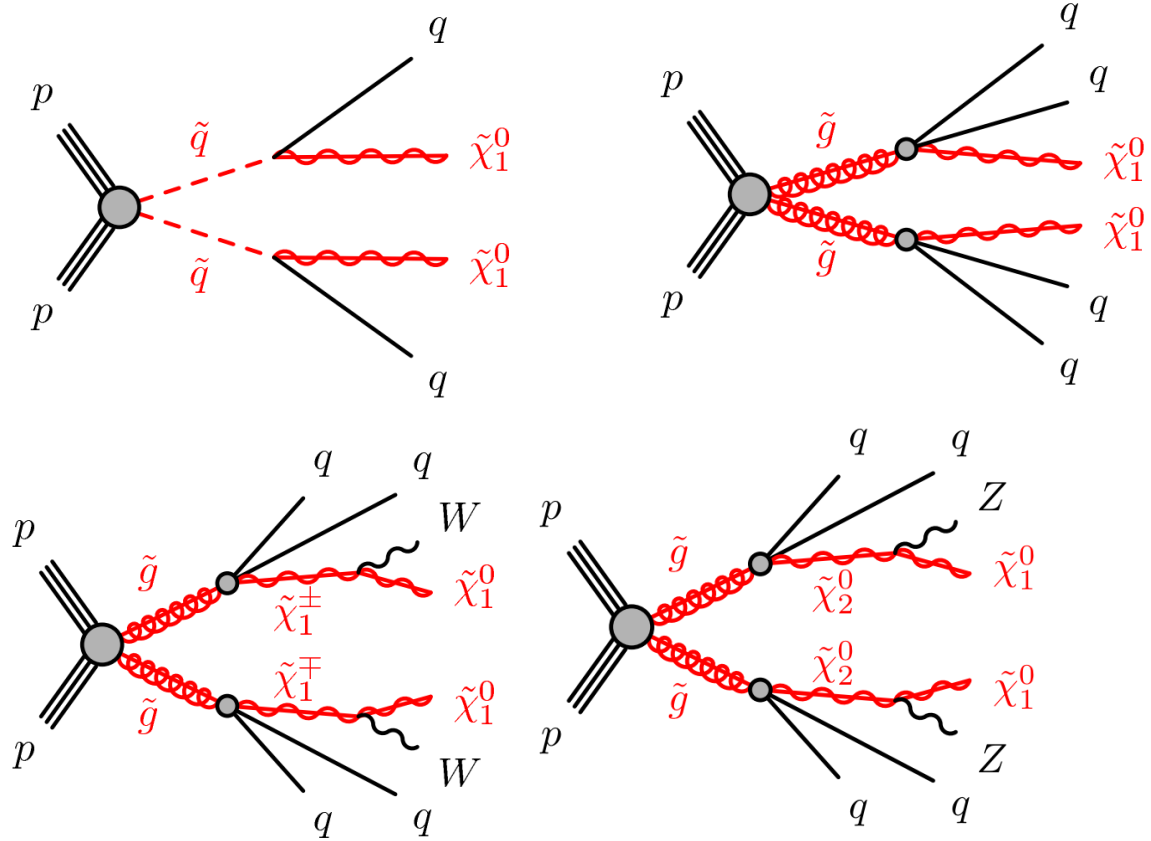
469 We are finally at the point where we can discuss the phenomenology of the MSSM,
470 in particular as it manifests itself at the energy scales of the LHC.

471 As noted above in Sec.3.2, the assumption of *R*–parity has important conse-
472 quences for MSSM phenomenology. The SM particles have $R = 1$, while the sparticles
473 all have $R = -1$. Simply, this is the “charge” of supersymmetry. Since the particles of
474 LHC collisions (pp) have total incoming $R = 1$, we must expect that all sparticles will
475 be produced in *pairs*. An additional consequence of this symmetry is the fact that the
476 lightest supersymmetric particle (LSP) is *stable*. Off each branch of the Feynmann
477 diagram shown in Fig., we have $R = -1$, and this can only decay to another sparticle
478 and a SM particle. Once we reach the lightest sparticle in the decay, it is absolutely
479 stable. This leads to the common signature E_T^{miss} for a generic SUSY signal.

480 For this thesis, we will be presenting an inclusive search for squarks and gluinos
481 with zero leptons in the final state. This is a very interesting decay channel⁴, due
482 to the high cross-sections of $\tilde{g}\tilde{g}$ and $\tilde{q}\tilde{q}$ decays, as can be seen in Fig.?? [83]. This
483 is a direct consequence of the fact that these are the colored particles of the MSSM.
484 Since the sparticles interact with the gauge groups of the SM in the same way as their
485 SM partners, the colored sparticles, the squarks and gluinos, are produced and decay
486 as governed by the color group $SU(3)_C$ with the strong coupling g_S . The digluino
487 production is particularly copious, due to color factor corresponding to the color octet

⁴Prior to Run1, probably the most *most* interesting SUSY decay channel.

Figure 3.3: SUSY signals considered in this thesis



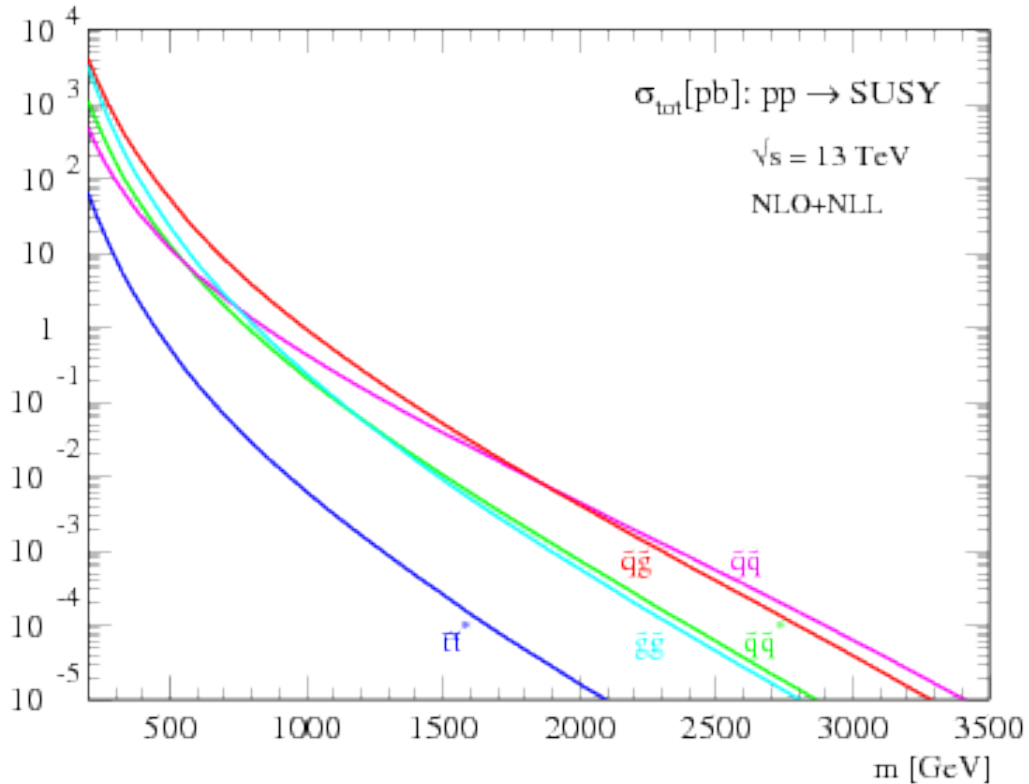
488 of $SU(3)C$.

489 In the case of disquark production, the most common decay mode of the squark in
 490 the MSSM is a decay directly to the LSP plus a single SM quark [15]. This means the
 491 basic search strategy of disquark production is two jets from the final state quarks,
 492 plus missing transverse energy for the LSPs. There are also cascade decays, the most
 493 common of which, and the only one considered in this thesis, is $\tilde{q} \rightarrow q\chi_1^\pm \rightarrow qW^\pm\chi_1^0$.

494 For digluino production, the most common decay is $\tilde{g} \rightarrow g\tilde{q}$, due to the large
 495 g_S coupling. The squark then decays as listed above. In this case, we generically
 496 search for four jets and missing transverse energy from the LSPs. We can also have
 497 the squark decay in association with a W^\pm or Z^0 ; in this thesis, we are interested in
 498 those cases where this vector boson goes hadronically.

499 In the context of experimental searches for SUSY, we often consider *simplified*

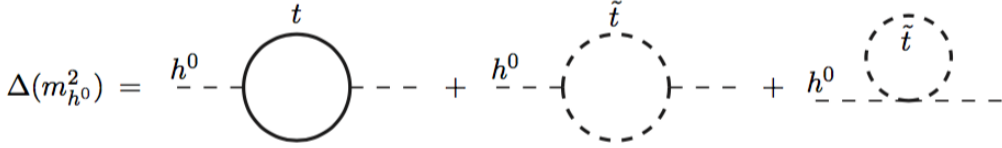
Figure 3.4: SUSY production cross-sections as a function of sparticle mass at $\sqrt{s} = 13$ TeV.



models. These models make certain assumptions which allow easy comparisons of results by theorists and rival experimentalists. In the context of this thesis, the simplified models will make assumptions about the branching ratios described in the preceding paragraphs. In particular, we will often choose a model where the decay of interest occurs with 100% branching ratio. This is entirely for ease of interpretation by other physicists⁵, but it is important to recognize that these are more a useful comparison tool, especially with limits, than a strict statement about the potential masses of sought-after beyond the Standard Model particle.

⁵In the author's opinion, this often leads to more confusion than comprehension. We will revisit the shortcomings of simplified models in the Conclusion to this thesis.

Figure 3.5: Loop diagrams correct the Higgs mass in the MSSM



508 3.4 How SUSY solves the problems with the SM

509 We now return to the issues with the Standard Model as described in Ch.2 to see
 510 how these issues are solved by supersymmetry.

511 Quadratic divergences to the Higgs mass

The quadratic divergences induced by the loop corrections to the Higgs mass, for example from the top Yukawa coupling, goes as

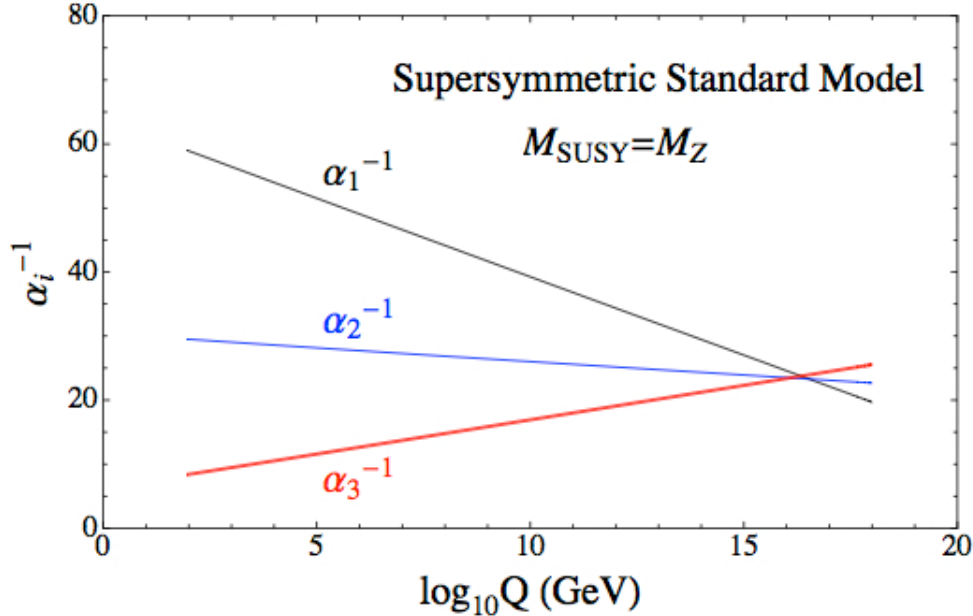
$$\delta m_H^2 \approx \left(\frac{m_t}{8\pi^2 \langle \phi \rangle_{VEV}} \right)^2 \Lambda_{Planck}^2. \quad (3.16)$$

512 The miraculous thing about SUSY is each of these terms *automatically* comes
 513 with a term which exactly cancels this contribution[15]. The fermions and bosons
 514 have opposite signs in this loop diagram to all orders in perturbation theory, which
 515 completely solves the hierarchy problem. This is the most well-motivated reason for
 516 supersymmetry.

517 Gauge coupling unification

518 An additional motivation for supersymmetry is seen by the gauge coupling unification
 519 high scales. In the Standard Model, as we saw the gauge couplings fail to unify at
 520 high energies. In the MSSM and many other forms of supersymmetry, the gauge
 521 couplings unify at high energy, as can be seen in Fig.???. This provides additional
 522 aesthetic motivation for supersymmetric theories.

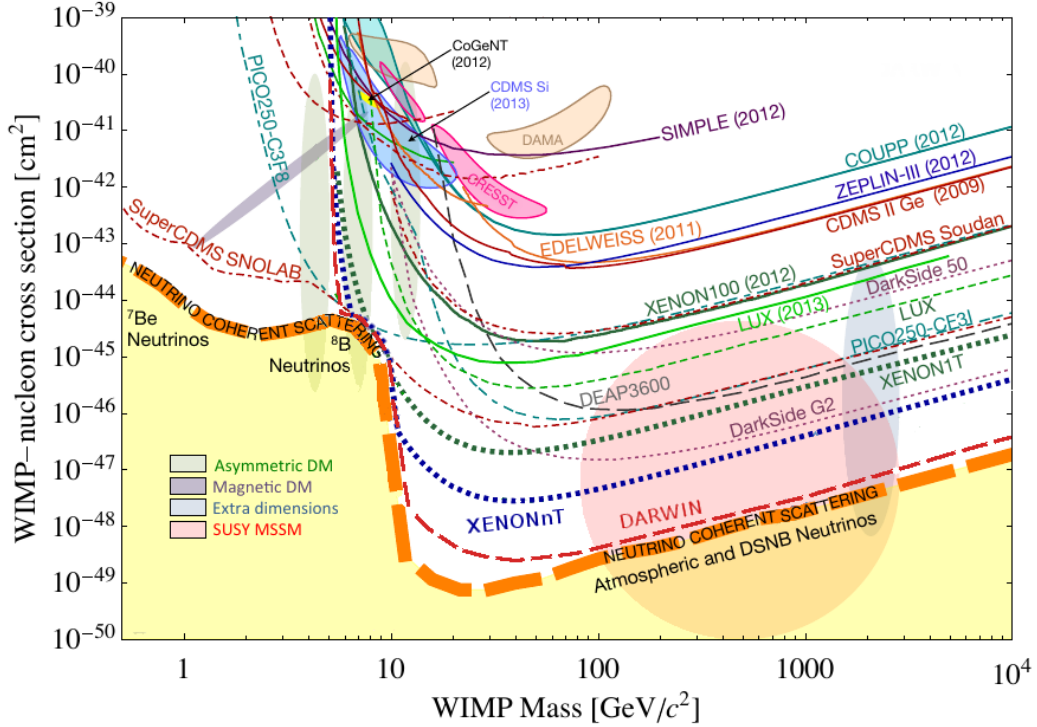
Figure 3.6: The running of Standard Model gauge couplings; compare to Fig.2.4. The MSSM gauge couplings nearly intersect at high energies.



523 Dark matter

524 As we discussed previously, the lack of any dark matter candidate in the Standard
 525 Model naturally leads to beyond the Standard Model theories. In the Standard Model,
 526 there is a natural dark matter candidate in the lightest supersymmetric particle[15]
 527 The LSP would in dark matter experiments be called a *weakly-interacting massive*
 528 *particle* (WIMP), which is a type of cold dark matter [22, 84]. These WIMPS would
 529 only interact through the weak force and gravity, which is exactly as a model like the
 530 MSSM predicts for the neutralino. In Fig.3.7, we can see the current WIMP exclusions
 531 for a given mass. The range of allowed masses which have not been excluded for LSPs
 532 and WIMPs have significant overlap. This provides additional motivation outside of
 533 the context of theoretical details.

Figure 3.7: WIMP exclusions from direct dark matter detection experiments.



534 3.5 Conclusions

535 Supersymmetry is the most well-motivated theory for physics beyond the Standard
 536 Model. It provides a solution to the hierarchy problem, leads to gauge coupling
 537 unification, and provides a dark matter candidate consistent with galactic rotation
 538 curves. As noted in this chapter, due to the LSPs in the final state, most SUSY
 539 searches require a significant amount of missing transverse energy in combination
 540 with jets of high transverse momentum. However, there is some opportunity to do
 541 better than this, especially in final states where one has two weakly-interacting LSPs
 542 on opposite sides of some potentially complicated decay tree. We will see how this is
 543 done in Ch.??.

The Large Hadron Collider

546 The Large Hadron Collider (LHC) produces high-energy protons which are collided
 547 at the center of multiple large experiments at CERN on the outskirts of Geneva,
 548 Switzerland [85]. The LHC produces the highest energy collisions in the world,
 549 with design center-of-mass energy of $\sqrt{s} = 14$ TeV, which allows the experiments
 550 to investigate physics far beyond the reach of previous colliders. This chapter will
 551 summarize the basics of accelerator physics, especially with regards to discovering
 552 physics beyond the Standard Model. We will describe the CERN accelerator complex
 553 and the LHC.

554 **4.1 Basics of Accelerator Physics**

555 This section follows closely the presentation of [86].

Simple particle accelerators simply rely on the acceleration of charged particles in a static electric field. Given a field of strength E , charge q , and mass m , this is simply

$$a = \frac{qE}{m}. \quad (4.1)$$

556 For a given particle with a given mass and charge, this is limited by the static electric
 557 field which can be produced, which in turn is limited by electrical breakdown at high
 558 voltages.

559 There are two complementary solutions to this issue. First, we use the *radio*
 560 *frequency acceleration* technique. We call the devices used for this *RF cavities*. The

561 cavities produce a time-varied electric field, which oscillate such that the charged
 562 particles passing through it are accelerated towards the design energy of the RF
 563 cavity. This oscillation also induces the particles into *bunches*, since particles which
 564 are slightly off in energy from that induced by the RF cavity are accelerated towards
 565 the design energy.

Second, one bends the particles in a magnetic field, which allows them to pass through the same RF cavity over and over. This second process is often limited by *synchrotron radiation*, which describes the radiation produced when a charged particle is accelerated. The power radiated is

$$P \sim \frac{1}{r^2} \left(E/m \right)^4 \quad (4.2)$$

566 where r is the radius of curvature and E, m is the energy (mass) of the charged
 567 particle. Given an energy which can be produced by a given set of RF cavities (which
 568 is *not* limited by the mass of the particle), one then has two options to increase the
 569 actual collision energy : increase the radius of curvature or use a heavier particle.
 570 Practically speaking, the easiest options for particles in a collider are protons and
 571 electrons, since they are (obviously) copious in nature and do not decay¹. Given the
 572 dependence on mass, we can see why protons are used to reach the highest energies.
 573 The tradeoff for this is that protons are not point particles, and we thus we don't
 574 know the exact incoming four-vectors of the protons, as discussed in Ch.2.

The particle *beam* refers to the bunches all together. An important property of a beam of a particular energy E , moving in uniform magnetic field B , containing particles of momentum p is the *beam rigidity* :

$$R \equiv rB = p/c. \quad (4.3)$$

575 The linear relation between r and p , or alternatively B and p have important
 576 consequences for LHC physics. For hadron colliders, this is the limiting factor on

¹Muon colliders are a really cool option at high energies, since the relativistic γ factor gives them a relatively long lifetime in the lab frame.

577 going to higher energy scales; one needs a proportionally larger magnetic field to
578 keep the beam accelerating in a circle.

579 Besides the rigidity of the beam, the most important quantities to characterize
580 a beam are known as the (normalized) *emittance* ϵ_N and the *betatron function* β .
581 These quantities determine the transverse size σ of a relativistic beam $v \gtrsim c$ beam :
582 $\sigma^2 = \beta^* \epsilon_N / \gamma_{\text{rel}}$, where β^* is the value of the betatron function at the collision point
583 and γ_{rel} is the Lorentz factor.

These quantities determine the *instantaneous luminosity* L of a collider, which combined with the cross-section σ of a particular physics process, give the rate of this physics process :

$$R = L\sigma. \quad (4.4)$$

The instantaneous luminosity L is given by :

$$L = \frac{f_{\text{rev}} N_b^2 F}{4\pi\sigma^2} = \frac{f_{\text{rev}} n N_b^2 \gamma_{\text{rel}} F}{4\pi\beta^* \epsilon_N}. \quad (4.5)$$

584 Here we have introduced the frequency of revolutions f_{rev} , the number of bunches n ,
585 the number of protons per bunch N_b^2 , and a geometric factor F related to the crossing
586 angle of the beams.

The *integrated luminosity* $\int L$ gives the total number of a particular physics process P , with cross-section σ_P .

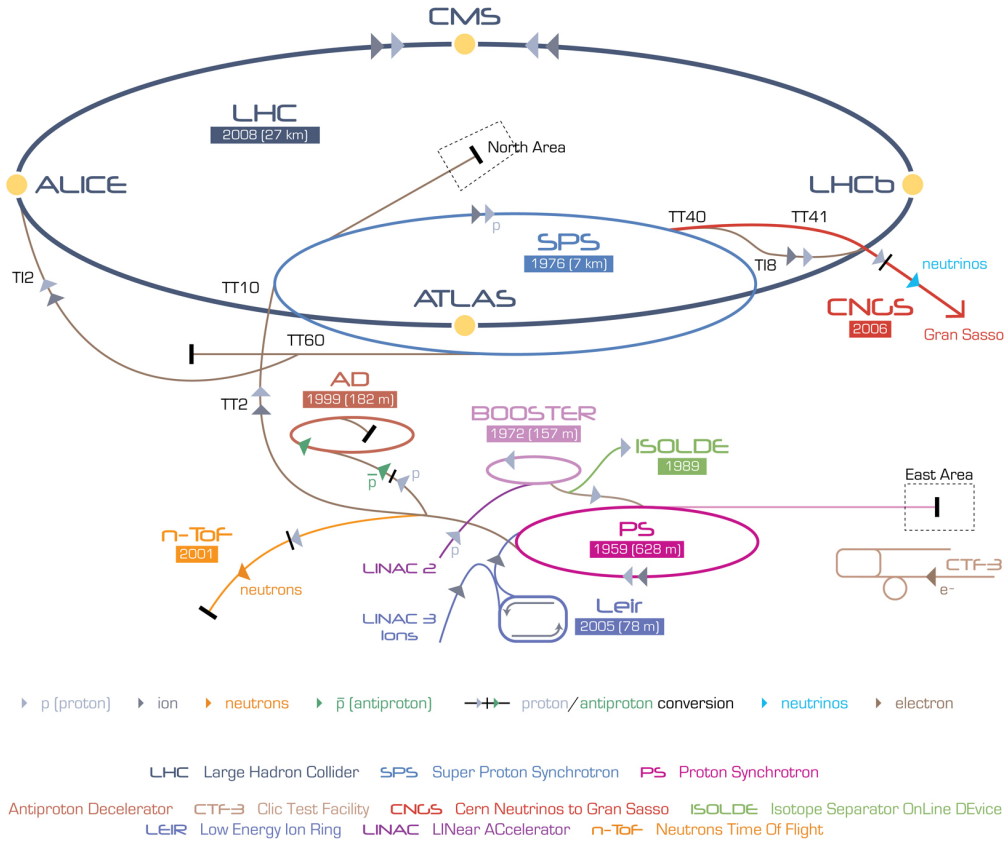
$$N_P = \sigma_P \int L. \quad (4.6)$$

587 Due to this simple relation, one can also quantify the “amount of data delivered” by
588 a collider simply by $\int L$.

589 4.2 Accelerator Complex

590 The Large Hadron Collider is the last accelerator in a chain of accelerators which
591 together form the CERN accelerator complex, which can be seen in 4.1. The protons

Figure 4.1: The CERN accelerator complex.



begin their journey to annihilation in a hydrogen source, where they are subsequently ionized. The first acceleration occurs in the Linac 2, a linear accelerator composed of RF cavities. The protons leave the Linac 2 at an energy of 50 MeV and enter the Proton Synchrotron Booster (PSB). The PSB contains four superimposed rings, which accelerate the protons to 1.4 GeV. The protons are then injected into the Proton Synchrotron (PS). This synchrotron increases the energy up to 25 GeV. After leaving the PS, the protons enter the Super Proton Synchrotron (SPS). This is the last step before entering the LHC ring, and the protons are accelerated to 450 GeV. From the SPS, the protons are injected into the beam pipes of the LHC. The process to fill the LHC rings with proton bunches from start to finish typically takes about four minutes.

603 4.3 Large Hadron Collider

The Large Hadron Collider is the final step in the CERN accelerator complex, and produces the collisions analyzed in this thesis. From the point of view of experimentalists on the general-purpose ATLAS and CMS experiments, the main goal of the LHC is to deliver collisions at the highest possible energy, with the highest possible instantaneous luminosity. The LHC was installed in the existing 27 km tunnel used by the Large Electron Positron (LEP) collider [87]. This allowed the existing accelerator complex at CERN, described in the previous section, to be used as the injection system to prepare the protons up to 450 GeV. Many aspects of the LHC design were decided by this very fact, and specified the options allowed to increase the energy or luminosity. In particular, the radius of the tunnel was already specified; from Eq.4.3, this implies the momentum (or energy) of the beam is entirely determined by the magnetic field. Given the 27 km circumference of the LEP tunnel, one can calculate the required magnetic field to reach the 7 TeV per proton design energy of the LHC :

$$r = C/2\pi = 4.3 \text{ km} \quad (4.7)$$

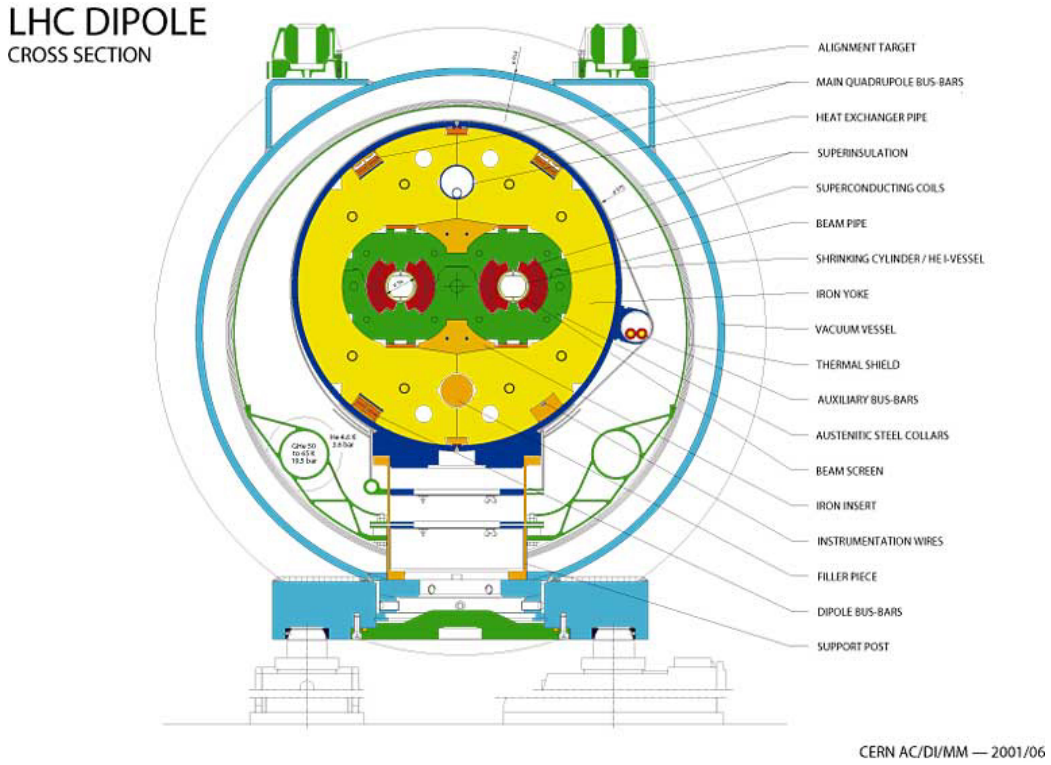
$$\rightarrow B = \frac{p}{rc} = 5 \text{ T} \quad (4.8)$$

604 In fact, the LHC consists of 8 528 m straight portions consisting of RF cavities, used
605 to accelerate the particles, and 8 circular portions which bend the protons around the
606 LHC ring. These circular portions actually have a slightly smaller radius of curvature
607 $r = 2804 \text{ m}$, and we require $B = 8.33 \text{ T}$. To produce this large field, we need to use
608 superconducting magnets, as discussed in the next section.

609 Magnets

610 There are many magnets used by the LHC machine, but the most important are the
611 1232 dipole magnets; a schematic is shown in Fig.4.2 and a photograph is shown in

Figure 4.2: Schematic of an LHC dipole magnet.



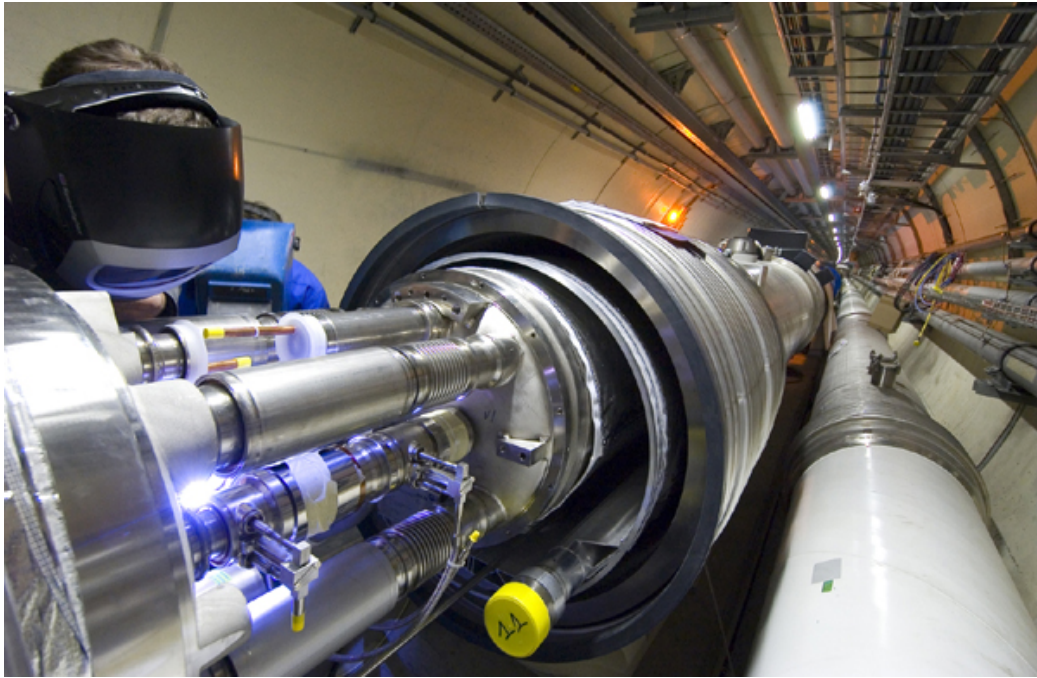
612 Fig.4.3.

613 The magnets are made of Niobium and Titanium. The maximum field strength is
 614 10 T when cooled to 1.9 Kelvin. The magnets are cooled by superfluid helium, which
 615 is supplied by a large cryogenic system. Due to heating between the eight helium
 616 refrigerators and the beampipe, the helium is cooled in the refrigerators to 1.8 K.

617 A failure in the cooling system can cause what is known as a *quench*. If the
 618 temperature goes above the critical superconducting temperature, the metal loses its
 619 superconducting properties, which leads to a large resistance in the metal. This leads
 620 to rapid temperature increases, and can cause extensive damages if not controlled.

621 The dipole magnets are 16.5 meters long with a diameter of 0.57 meters. There
 622 are two individual beam pipes inside each magnet, which allows the dipoles to house
 623 the beams travelling in both directions around the LHC ring. They curve slightly,
 624 at an angle of 5.1 mrad, which carefully matches the curvature of the ring. The

Figure 4.3: Photograph of a technician connecting an LHC dipole magnet.



625 beampipes inside of the magnets are held in high vacuum, to avoid stray particles
626 interacting with the beam.

627 **4.4 Dataset Delivered by the LHC**

628 In this thesis, we analyze the data delivered by the LHC to ATLAS in the 2015 and
629 2016 datasets. The beam parameters relevant to this dataset are available in Table
630 [4.1](#).

631 The peak instantaneous luminosity delivered in 2015 (2016) was $L =$
632 $5.2(11) \text{ cm}^{-2}\text{s}^{-1} \times 10^{33}$. One can note that the instantaneous luminosity delivered in
633 the 2016 dataset exceeds the design luminosity of the LHC. The total integrated
634 luminosity delivered was 13.3 fb^{-1} . In Figure [4.4](#), we display the integrated luminosity
635 as a function of day for 2015 and 2016.

Figure 4.4: Integrated Luminosity delivered by the LHC and collected by ATLAS in the 2015 and 2016 datasets.

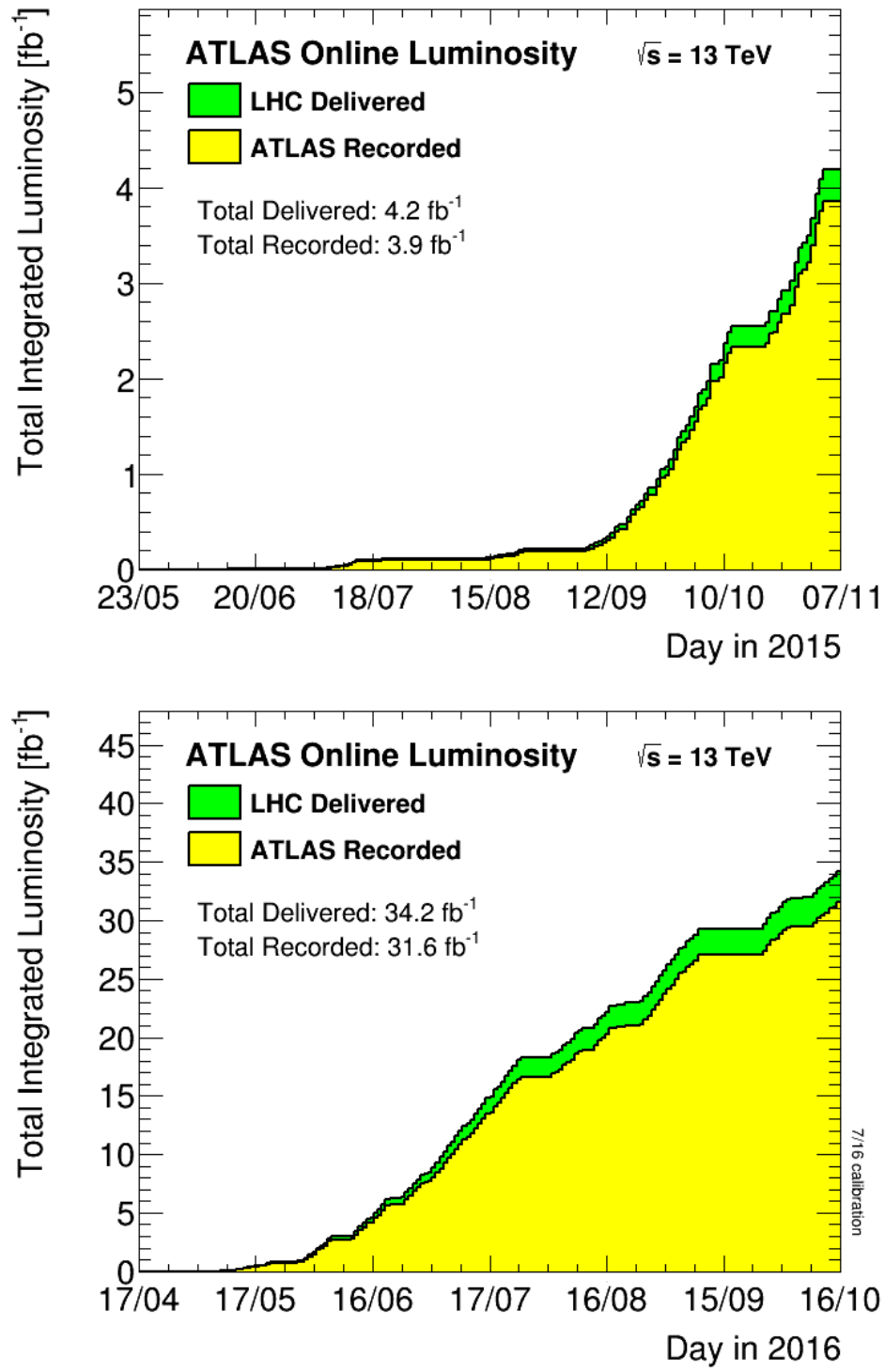
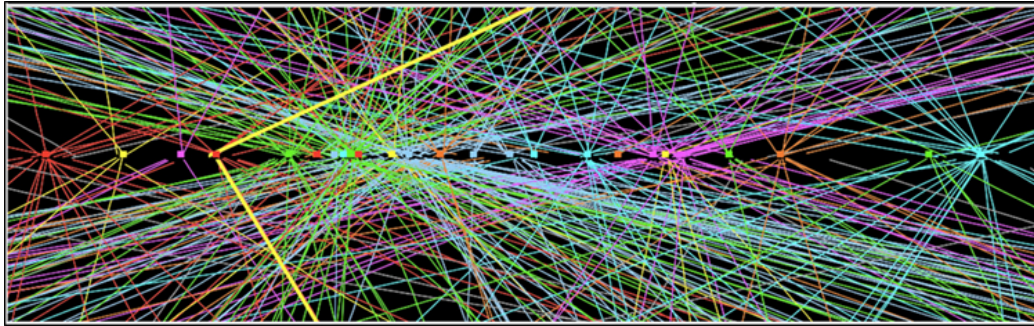


Table 4.1: Beam parameters of the Large Hadron Collider.

Parameter	Injection	Extraction
Energy (GeV)	450	7000
Rigidity (T-m)	3.8	23353
Bunch spacing (ns)	25	25
Design Luminosity ($\text{cm}^{-2}\text{s}^{-1} \times 10^{34}$)	-	1.0
Bunches per proton beam	2808	2808
Protons per bunch	1.15 e11	1.15 e11
Beam lifetime (hr)	-	10
Normalized Emittance ϵ_N (mm μrad)	3.3	3.75
Betatron function at collision point β^* (cm)	-	55

Figure 4.5: Simulated event with many pileup vertices.



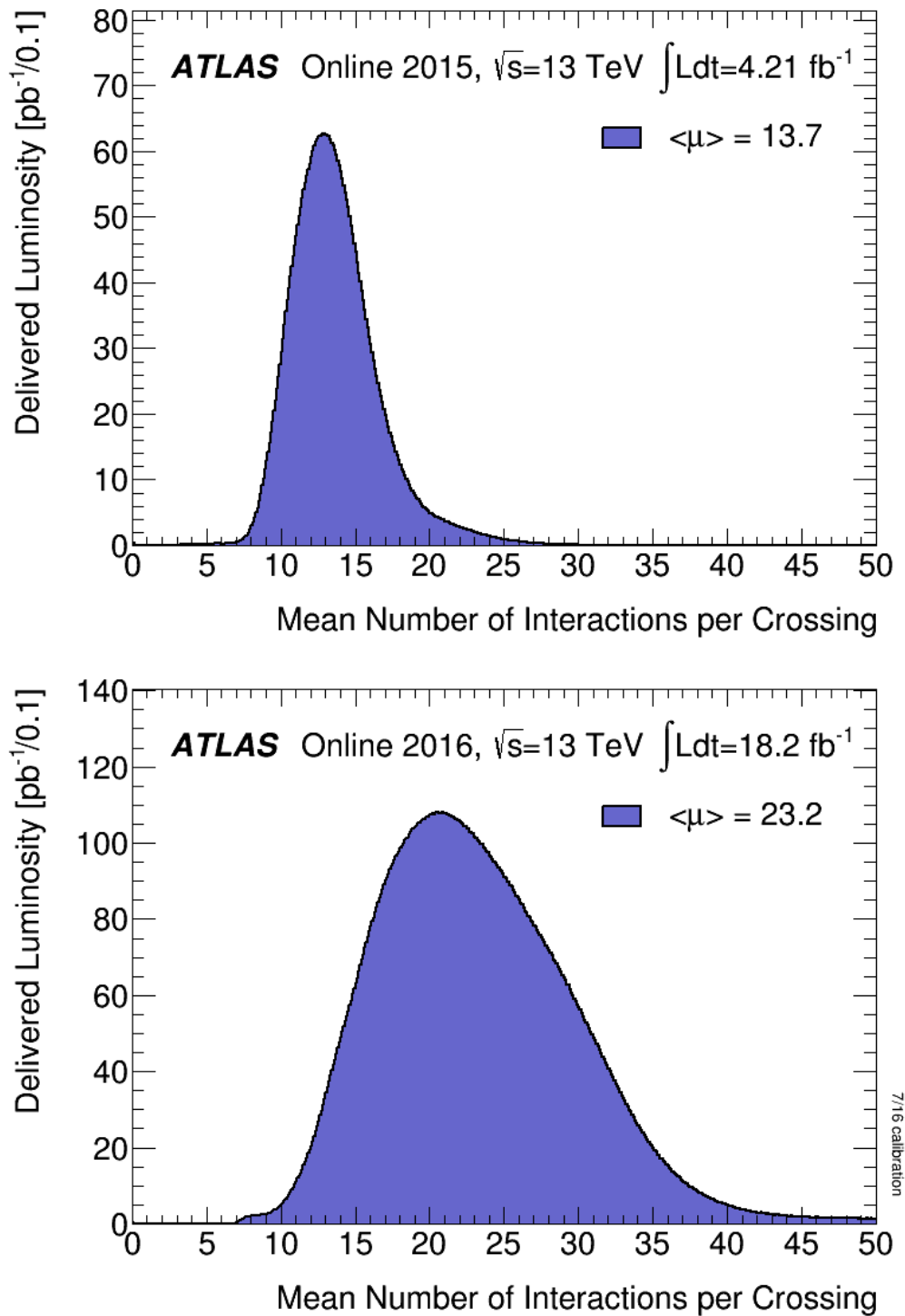
636 Pileup

637 *Pileup* is the term for the additional proton-proton interactions which occur during
 638 each bunch crossing of the LHC. At the beginning of the LHC physics program, there
 639 had not been a collider which averaged more than a single interaction per bunch
 640 crossing. In the LHC, each bunch crossing (or *event*) generally contains multiple
 641 proton-proton interactions. An simulated event with many *vertices* can be seen in
 642 Fig.4.5. The so-called *primary vertex* (or *hard scatter vertex*) refers to the vertex
 643 which has the highest Σp_T^2 ; this summation occurs over the *tracks* in the detector,
 644 which we will describe later[**ATL-INDET-PUB-2009-001**]. We then distinguish
 645 between *in-time* pileup and *out-of-time* pileup. In-time pileup refers to the additional
 646 proton-proton interactions which occur in the event. Out-of-time pileup refers to
 647 effects related to proton-proton interactions previous bunch crossings.

648 We quantify in-time pileup by the number of “primary”² vertices in a particular
649 event. To quantify the out-of-time pileup, we use the average number of interactions
650 per bunch crossing $\langle \mu \rangle$ over some human-scale time. In Figure 4.6, we show the
651 distribution of μ for the dataset used in this thesis.

²The primary vertex is as defined above, but we unfortunately use the same name here.

Figure 4.6: Mean number of interactions per bunch crossing in the 2015 and 2016 datasets.



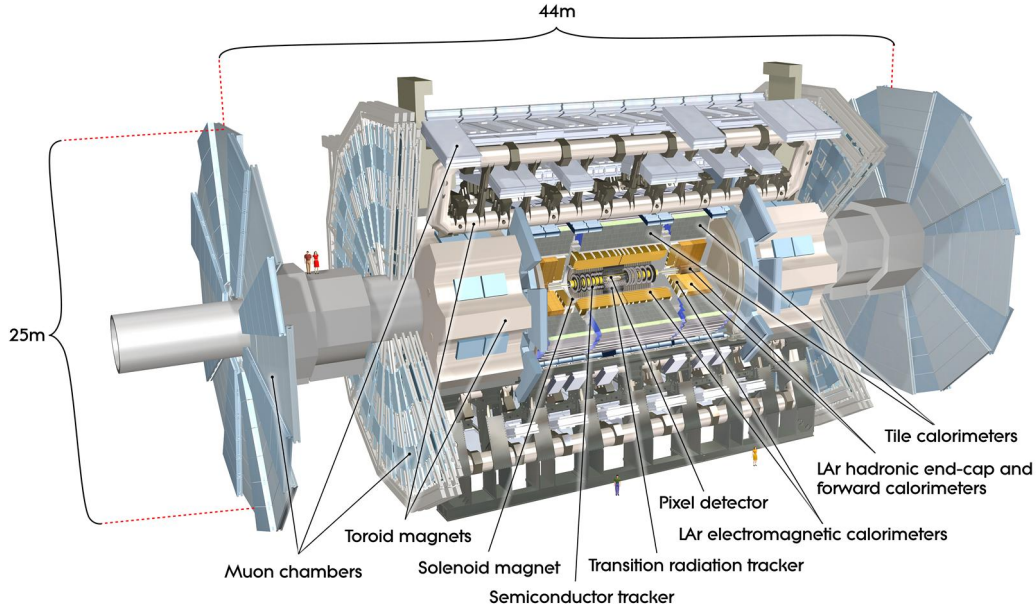
The ATLAS detector

654 The dataset analyzed in this thesis was taken by the ATLAS detector [88], which is
 655 located at the “Point 1” cavern of the LHC beampipe, just across the street from
 656 the main CERN campus. The much-maligned acronym stands for *A Toroidal LHC*
 657 *ApparatuS*. ATLAS is a massive cylindrical detector, with a radius of 12.5 m and a
 658 length of 44 m, with nearly hermitic coverage around the collision point. It consists
 659 of multiple subdetectors; each plays a role in ATLAS’s ultimate purpose of measuring
 660 the energy, momentum, and type of the particles produced in collisions delivered by
 661 the LHC. These subdetectors are immersed in a hybrid solenoid-toroid magnet system
 662 whichs forces charged particles to curve, which allows for precise measurements of
 663 their momenta. These magnetic fields are maximized in the central solenoid magnet,
 664 which contains a magnetic field of 2 T. A schematic of the detector can be seen in
 665 5.1.

666 The *inner detector* (ID) lies closest to the collision point, and contains three
 667 separate subdetectors. It provides pseudorapidity¹coverage of $|\eta| < 2.5$ for charged
 668 particles to interact with the tracking material. The tracks reconstructed from the
 669 inner detector hits are used to reconstruct the primary vertices, as noted in Ch.??,

¹ATLAS uses a right-handed Cartesian coordinate system; the origin is defined by the nominal beam interaction point. The positive- z direction is defined by the incoming beam travelling counterclockwise around the LHC. The positive- x direction points towards the center of the LHC ring from the origin, and the positive- y direction points upwards towards the sky. For particles of transverse (in the $x - y$ plane) momentum $p_T = \sqrt{p_x^2 + p_y^2}$ and energy E , it is generally most convenient fully describe this particle’s kinematics as measured by the detector in the (p_T, ϕ, η, E) basis. The angle $\phi = \arctan(p_y/p_x)$ is the standard azimuthal angle, and $\eta = \ln \tan(\theta/2)$ is known as the pseudorapidity, and defined based on the standard polar angle $\theta = \arccos(p_z/p_T)$. For locations of i.e. detector elements, both (r, ϕ, η) and (z, ϕ, η) can be useful.

Figure 5.1: The ATLAS detector

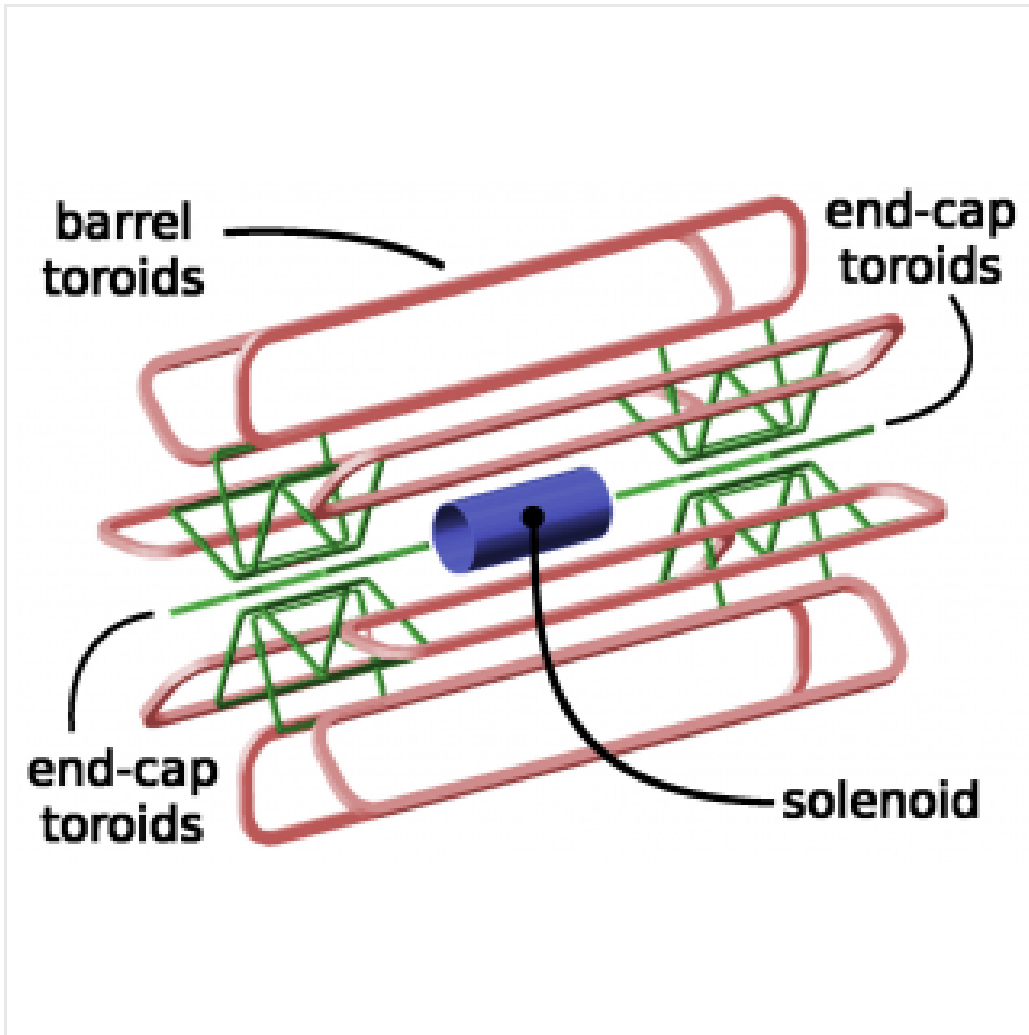


and to determine the momenta of charged particles. The ATLAS *calorimeter* consists of two subdetectors, known as the *electromagnetic* and *hadronic* calorimeters. These detectors stop particles in their detector material, and measure the energy deposition inside, which measures the energy of the particles deposited. The calorimeters provide coverage out to pseudorapidity of $|\eta| < 4.9$. The muon spectrometer is aptly named; it is specifically used for muons, which are the only particles which generally reach the outer portions of the detector. In this region, we have the large tracking systems of the muon spectrometer, which provide precise measurements of muon momenta. The muon spectrometer has pseudorapidity coverage of $|\eta| < 2.7$.

5.1 Magnets

ATLAS contains multiple magnetic systems; primarily, we are concerned with the solenoid, used by the inner detector, and the toroids located outside of the ATLAS calorimeter. A schematic is shown in Fig.5.2. These magnetic fields are used to bend

Figure 5.2: The ATLAS magnet system

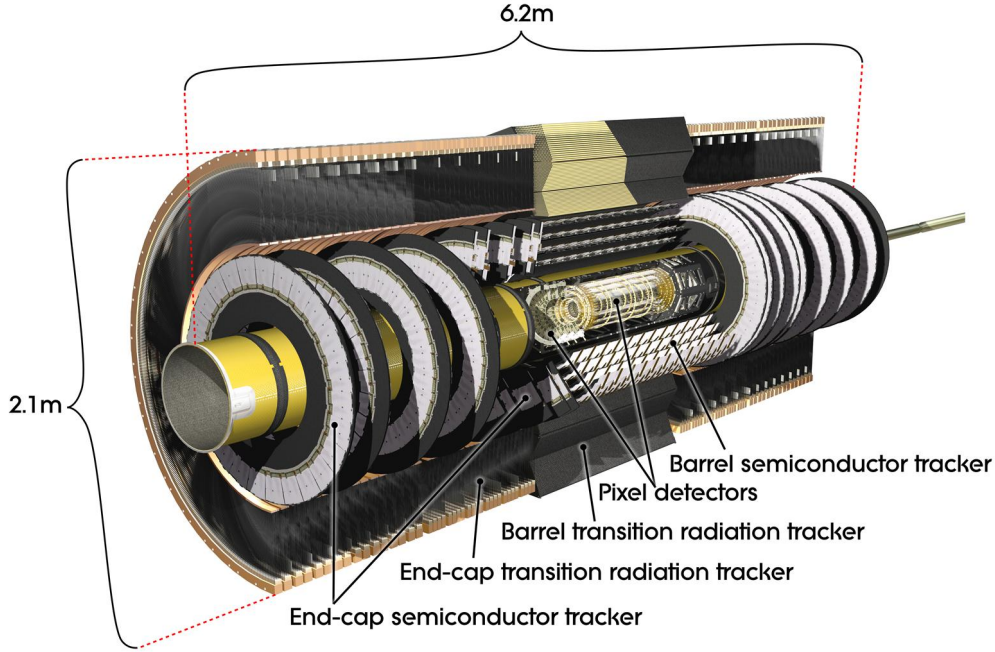


683 charged particles under the Lorentz force, which subsequently allows one to measure
684 their momentum.

685 The ATLAS central solenoid is a 2.3 m diameter, 5.3 m long solenoid at the center
686 of the ATLAS detector. It produces a uniform magnetic field of 2 T; this strong field
687 is necessary to accurately measure the charged particles in this field. An important
688 design constraint for the central solenoid was the decision to place it in between the
689 inner detector and the calorimeters. To avoid excessive impacts on measurements in
690 the calorimetry, the central solenoid must be as transparent as possible².

²This is also one of the biggest functional differences between ATLAS and CMS; in CMS, the

Figure 5.3: The ATLAS inner detector



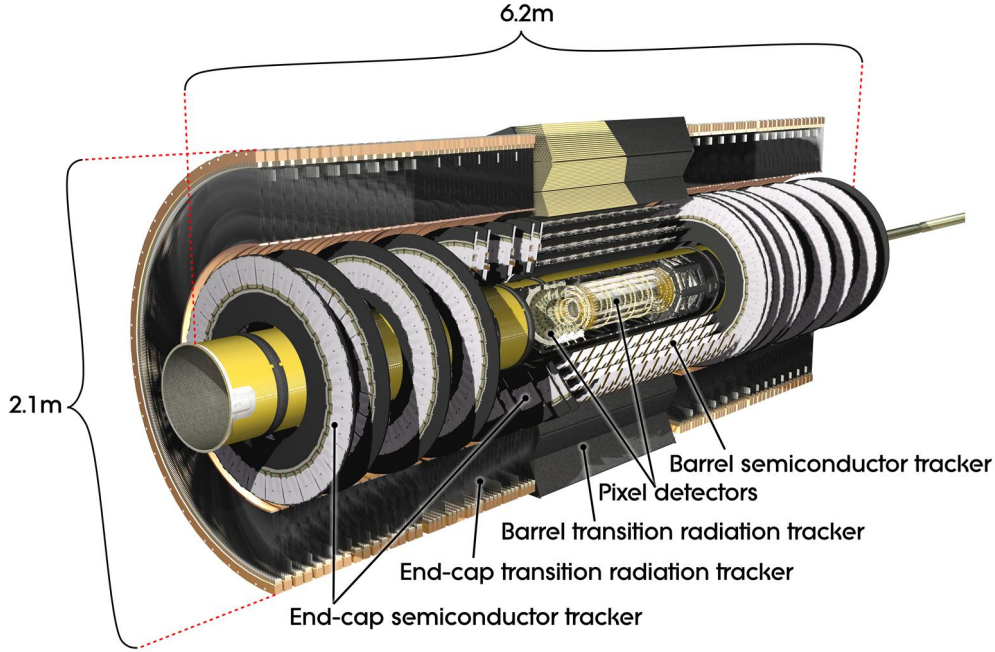
691 The toroid system consists of eight air-core superconducting barrel loops; these
692 give ATLAS its distinctive shape. There are also two endcap air-core magnets. These
693 produce a magnetic field in a region of approximately 26 m in length and 10 m of
694 radius. The magnetic field in this region is non-uniform, due to the prohibitive costs
695 of a solenoid magnet of that size.

696 **5.2 Inner Detector**

697 The ATLAS inner detector consists of three separate tracking detectors, which are
698 known as, in order of increasing distance from the interaction point, the Pixel
699 Detector, Semiconductor Tracker (SCT), and the Transition Radiation Tracker
700 (TRT). When charged particles pass through these tracking layers, they produce
701 *hits*, which using the known 2 T magnetic field, allows the reconstruction of *tracks*.
702 Tracks are used as inputs for reconstruction of many higher-level physics objects,

solenoid is outside of the calorimeters.

Figure 5.4: The ATLAS pixel detector



such as electrons, muons, photons, and E_T^{miss} . Accurate track reconstruction is thus crucial for precise measurements of charged particles.

Pixel Detector

The ATLAS pixel detector consists four layers of silicon “pixels”. This refers to the segmentation of the active medium into the pixels; compare to the succeeding silicon detectors, which will use silicon “strips”. This provides precise 3D hit locations. The layers are known as the “Insertable”³B-Layer (IBL), the B-Layer (or Layer-0), Layer-1, and Layer-2, in order of increasing distance from the interaction point. These layers are very close to the interaction point, and therefore experience a large amount of radiation.

Layer-1, Layer-2, and Layer-3 were installed with the initial construction of ATLAS. They contain front-end integrated electronics (FEI3s) bump-bonded to 1744

³Very often, the IBL is mistakenly called the Inner B-Layer, which would have been a much more sensible name.

715 silicon modules; each module is $250\ \mu\text{m}$ in thickness and contains 47232 pixels. These
716 pixels have planar sizes of $50 \times 400\ \mu\text{m}^2$ or $50 \times 600\ \mu\text{m}^2$, to provide highly accurate
717 location information. The FEI3s are mounted on long rectangular structures known
718 as staves, which encircle the beam pipe. A small tilt to each stave allows full coverage
719 in ϕ even with readout systems which are installed. These layers are at radia of 50.5
720 mm, 88.5 mm, and 122.5 mm from the interaction point.

721 The IBL was added to ATLAS after Run1 in 2012 at a radius of 33 mm from the
722 interaction point. The entire pixel detector was removed from the center of ATLAS
723 to allow an additional pixel layer to be installed. The IBL was required to preserve
724 the integrity of the pixel detector as radiation damage leads to inoperative pixels in
725 the other layers. The IBL consists of 448 FEI4 chips, arranged onto 14 staves. Each
726 FEI4 has 26880 pixels, of planar size $50 \times 250\ \mu\text{m}$. This smaller granularity was
727 required due to the smaller distance to the interaction point.

728 In total, a charged particle passing through the inner detector would expect to
729 leave four hits in the pixel detector.

730 Semiconductor Tracker

731 The SCT is directly beyond Layer-2 of the pixel detector. This is a silicon strip
732 detector, which do not provide the full 3D information of the pixel detector. The
733 dual-sensors of the SCT contain 2×768 individual strips; each strip has area $6.4\ \text{cm}^2$.
734 The SCT dual-sensor is then double-layered, at a relative angle of 40 mrad;
735 together these layers provide the necessary 3D information for track reconstruction.
736 There are four of these double-layers, at radia of 284 mm, 355 mm, 427 mm, and 498
737 mm. These double-layers provide hits comparable to those of the pixel detector, and
738 we have four additional hits to reconstruct tracks for each charged particle.

Figure 5.5: A ring of the Semiconductor Tracker

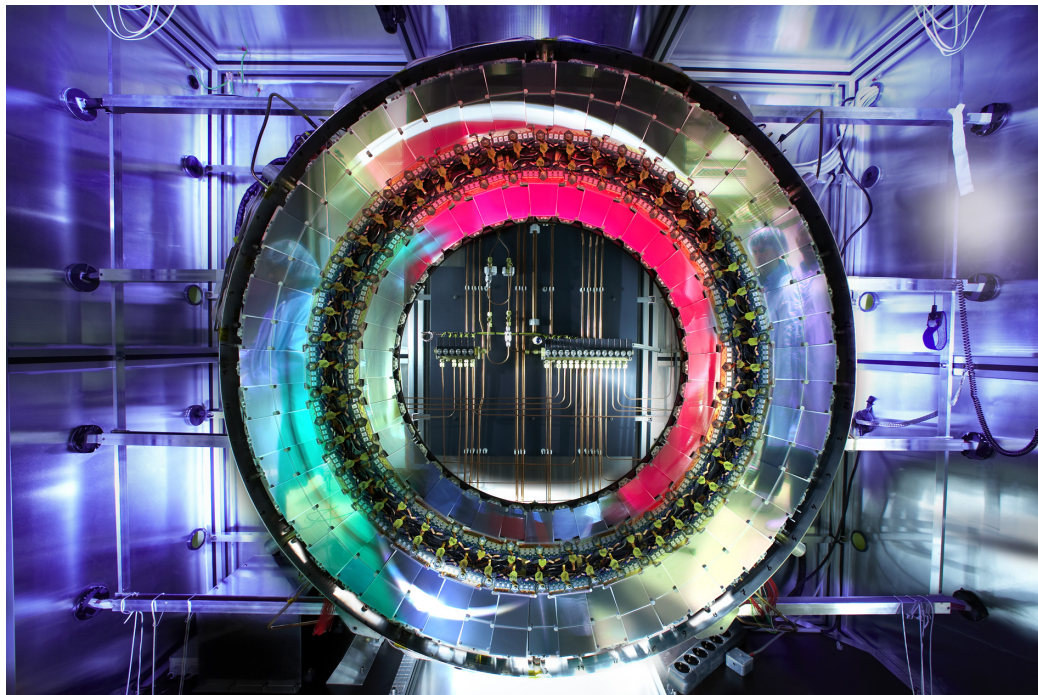
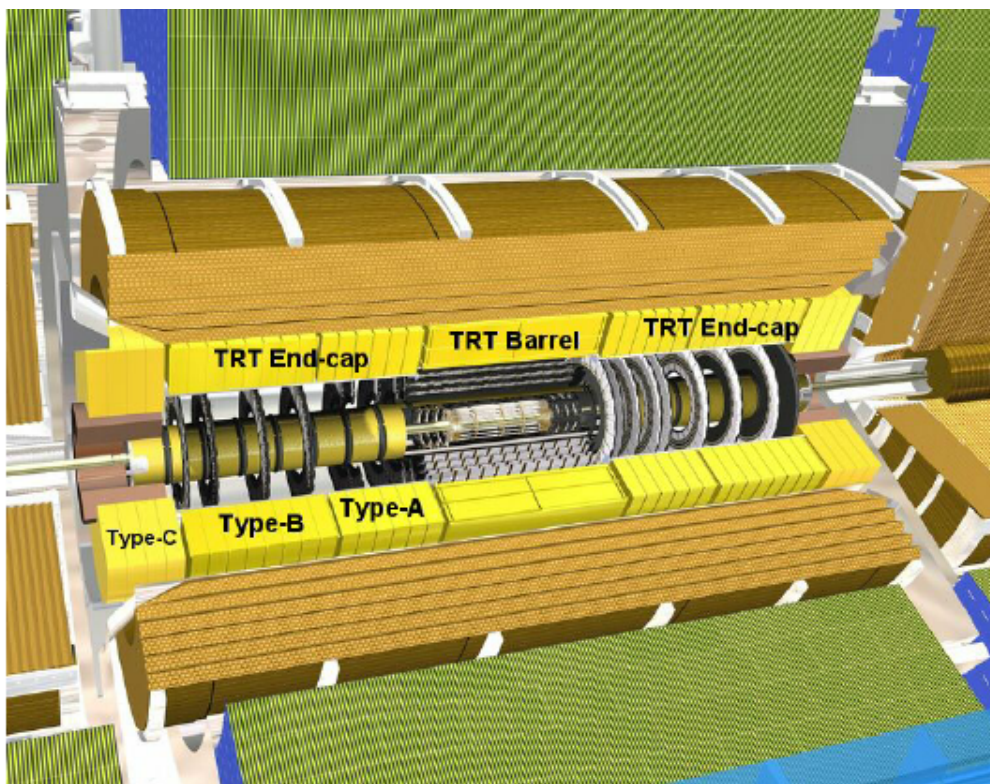


Figure 5.6: A schematic of the Transition Radiation Tracker



739 **Transition Radiation Tracker**

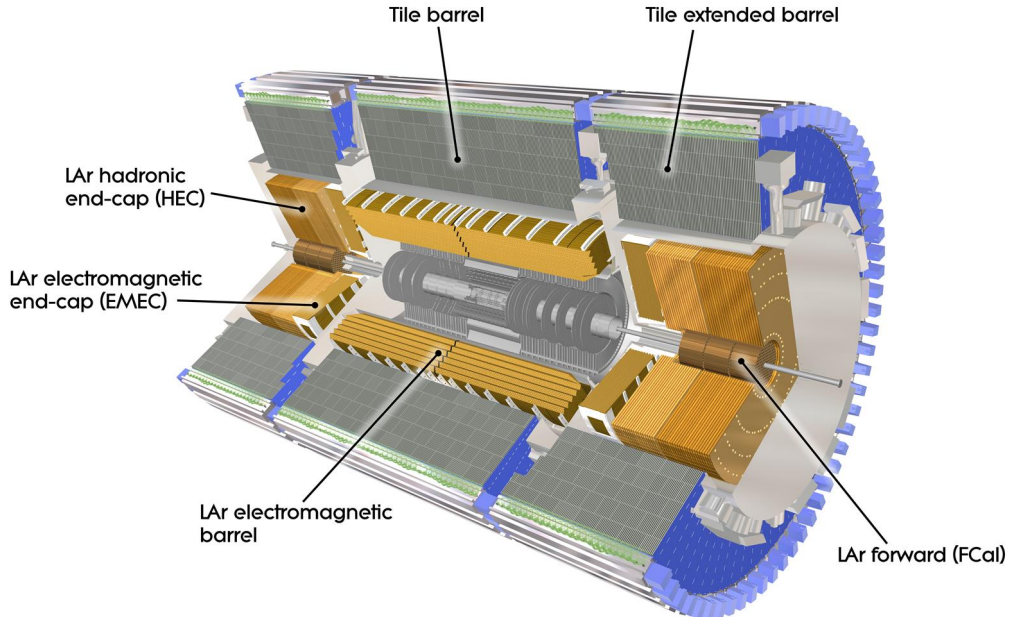
740 The Transition Radiation Tracker is the next detector radially outward from the SCT.
741 It contains straw drift tubes; these contain a tungsten gold-plated wire of $32 \mu\text{m}$
742 diameter held under high voltage (-1530 V) with the edge of the Kapton-aluminum
743 tube. They are filled with a gas mixture of primarily xenon that is ionized when
744 a charged particle passes through the tube. The ions are collected by the “drift”
745 due to the voltage inside the tubes, which is read out by the electronics. This gives
746 so-called “continuous tracking” throughout the tube, due to the large number of ions
747 produced.

748 The TRT is so-named due to the *transition radiation* (TR) it induces. Due to
749 the dielectric difference between the gas and tubes, TR is induced. This is important
750 for distinguishing electrons from their predominant background of minimum ionizing
751 particles. Generally, electrons have a much larger Lorentz factor than minimum
752 ionizing particles, which leads to additional TR. This can be used as an additional
753 handle for electron reconstruction.

754 **5.3 Calorimetry**

755 The calorimetry of the ATLAS detector also includes multiple subdetectors; these sub-
756 detectors allow precise measurements of the electrons, photons, and hadrons produced
757 by the ATLAS detector. Generically, calorimeters work by stopping particles in their
758 material, and measuring the energy deposition. This energy is deposited as a cascade
759 particles induce from interactions with the detector material known *showers*. ATLAS
760 uses *sampling* calorimeters; these alternate a dense absorbing material, which induces
761 showers, with an active layer which measures energy depositions by the induced
762 showers. Since some energy is deposited into the absorption layers as well, the energy
763 depositions must be properly calibrated for the detector.

Figure 5.7: The ATLAS calorimeter

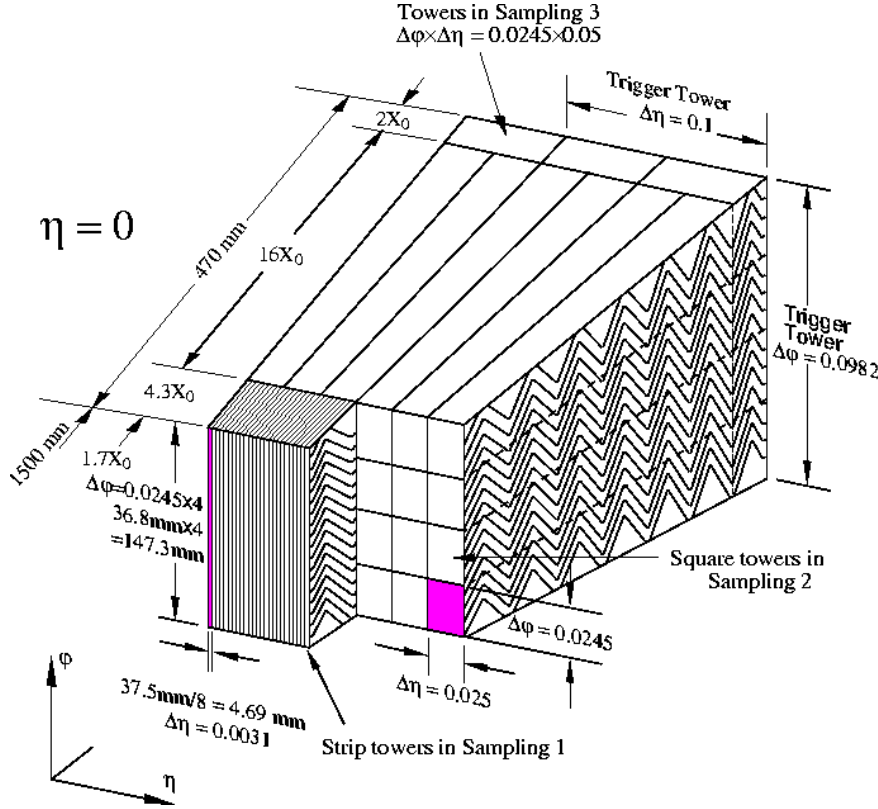


764 Electromagnetic objects (electrons and photons) and hadrons have much different
 765 interaction properties, and thus we need different calorimeters to accurately measure
 766 these different classes of objects; we can speak of the *electromagnetic* and *hadronic*
 767 calorimeters. ATLAS contains four separate calorimeters : the liquid argon (LAr)
 768 electromagnetic barrel calorimeter, the Tile barrel hadronic calorimeter, the LAr
 769 endcap electromagnetic calorimeter, the LAr endcap hadronic calorimeter, and the
 770 LAr Forward Calorimeter (FCal). Combined, these provide full coverage in ϕ up to
 771 $|\eta| < 4.9$, and can be seen in Fig.5.7.

772 Electromagnetic Calorimeters

773 The electromagnetic calorimeters of the ATLAS detector consist of the barrel and
 774 endcap LAr calorimeters. These are arranged into an ingenious ‘‘accordion’’ shape,
 775 shown in 5.8, which allows full coverage in ϕ and exceptional coverage in η while
 776 still allowing support structures for detector operation. The accordion is made of

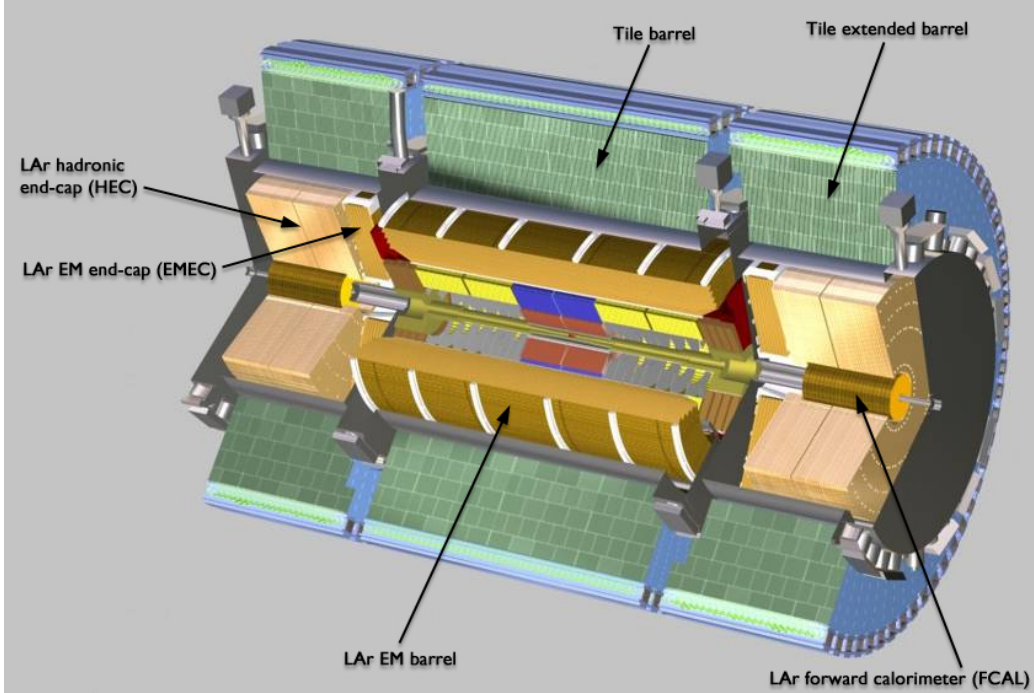
Figure 5.8: A schematic of a subsection of the barrel LAr electromagnetic calorimeter



777 layers with liquid argon (active detection material) and lead (absorber) to induce
 778 electromagnetic showers. The LAr EM calorimeters are each more than 20 radiation
 779 lengths deep, which provides the high stopping power necessary to properly measure
 780 the electromagnetic showers.

781 The barrel component of the LAr EM calorimeter extends from the center of the
 782 detector out to $|\eta| < 1.475$. The calorimeter has a presampler, which measures the
 783 energy of any EM shower induced before the calorimeter. This has segmentation of
 784 $\Delta\eta = 0.025, \Delta\phi = .01$. There are three “standard” layers in the barrel, which have
 785 decreasing segmentation into calorimeter *cells* as one travels radially outward from
 786 the interaction point. The first layer has segmentation of $\Delta\eta = 0.003, \Delta\phi = .1$, and
 787 is quite thin relative to the other layers at only 4 radiation lengths deep. It provides
 788 precise η and ϕ measurements for incoming EM objects. The second layer is the
 789 deepest at 16 radiation lengths, with a segmentation of $\Delta\eta = 0.025, \Delta\phi = 0.025$. It

Figure 5.9: A schematic of Tile hadronic calorimeter



is primarily responsible for stopping the incoming EM particles, which dictates its large relative thickness, and measures most of the energy of the incoming particles. The third layer is only 2 radiation lengths deep, with a rough segmentation of $\Delta\eta = 0.05$, $\Delta\phi = .025$. The deposition in this layer is primarily used to distinguish hadrons interacting electromagnetically and entering the hadronic calorimeter from the strictly EM objects which are stopped in the second layer.

The barrel EM calorimeter has a similar overall structure, but extends from $1.4 < |\eta| < 3.2$. The segmentation in η is better in the endcap than the barrel; the ϕ segmentation is the same. In total, the EM calorimeters contain about 190000 individual calorimeter cells.

Hadronic Calorimeters

The hadronic calorimetry of ATLAS sits directly outside the EM calorimetry. It contains three subdetectors : the barrel Tile calorimeter, the endcap LAr calorimeter,

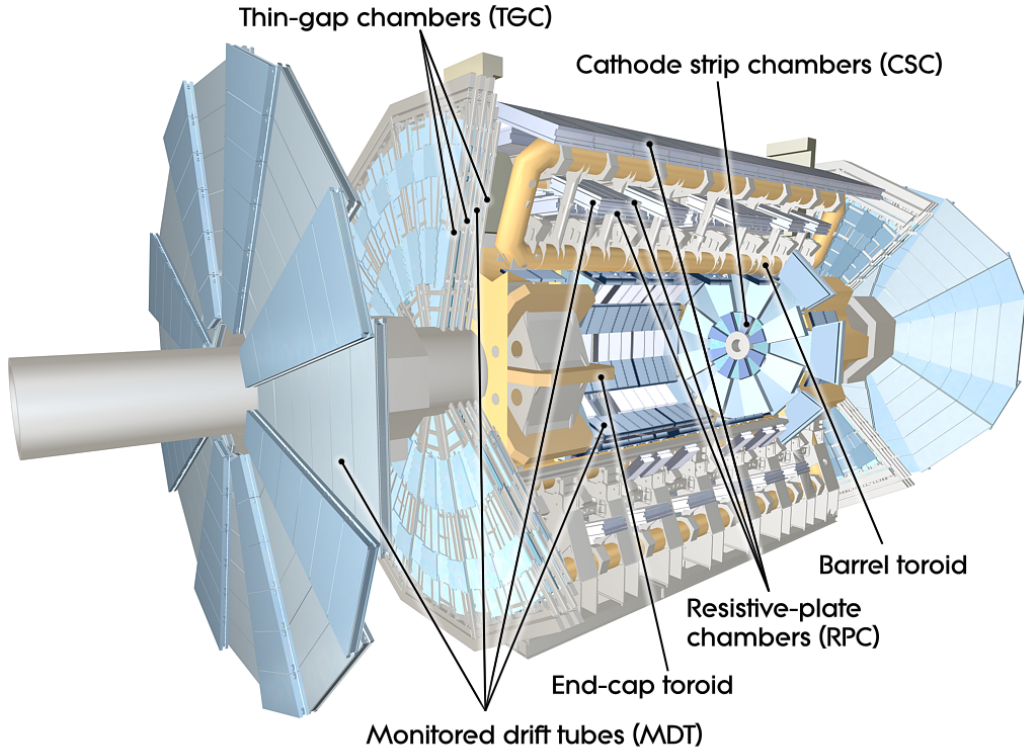
803 and the Forward LAr Calorimeter. Similar to the EM calorimeters, these are
804 sampling calorimeters that alternate steel (dense material) with an active layer
805 (plastic scintillator).

806 The barrel Tile calorimeter extends out to $|\eta| < 1.7$. There are again three layers,
807 which combined give about 10 interactions length of distance, which provides excellent
808 stopping power for hadrons. This is critical to avoid excess *punchthrough* to the muon
809 spectrometer beyond the hadronic calorimeters. The first layer has a depth of 1.5
810 interaction lengths. The second layer is again the thickest at a depth of 4.1 interaction
811 lengths; most of the energy of incoming particle is deposited here. Both the first and
812 second layer have segmentation of about $\Delta\eta = 0.1, \Delta\phi = 0.1$. Generally, one does not
813 need as fine of granularity in the hadronic calorimeter, since the energy depositions
814 in the hadronic calorimeters will be summed into the composite objects we know as
815 jets. The third layer has a thickness of 1.8 interaction lengths, with a segmentation of
816 $\Delta\eta = 0.2, \Delta\phi = 0.1$. The use of multiple layers allows one to understand the induced
817 hadronic shower as it propagates through the detector material.

818 The endcap LAr hadronic calorimeter covers the region $1.5 < |\eta| < 3.2$. It is
819 again a sampling calorimeter; the active material is LAr with a copper absorbed. It
820 does not use the accordion shape of the other calorimeters; it has a “standard” flat
821 shape perpendicular to the interaction point. The segmentation varies with η . For
822 $1.5 < |\eta| < 2.5$, the cells are $\Delta\eta = 0.1, \Delta\phi = 0.1$; in the region $2.5 < |\eta| < 3.2$, the
823 cells are $\Delta\eta = 0.2, \Delta\phi = 0.2$ in size.

824 The final calorimeter in ATLAS is the forward LAr calorimeter. Of those
825 subdetectors which are used for standard reconstruction techniques, the FCal sits
826 at the most extreme values of $3.1 < |\eta| < 4.9$. The FCal itself is made of three
827 subdetectors; FCal1 is actually an electromagnetic module, while FCal2 and FCal3
828 are hadronic. The absorber in FCal1 is copper, with a liquid argon active medium.
829 FCal2 and FCal3 also use a liquid argon active medium, with a tungsten absorber.

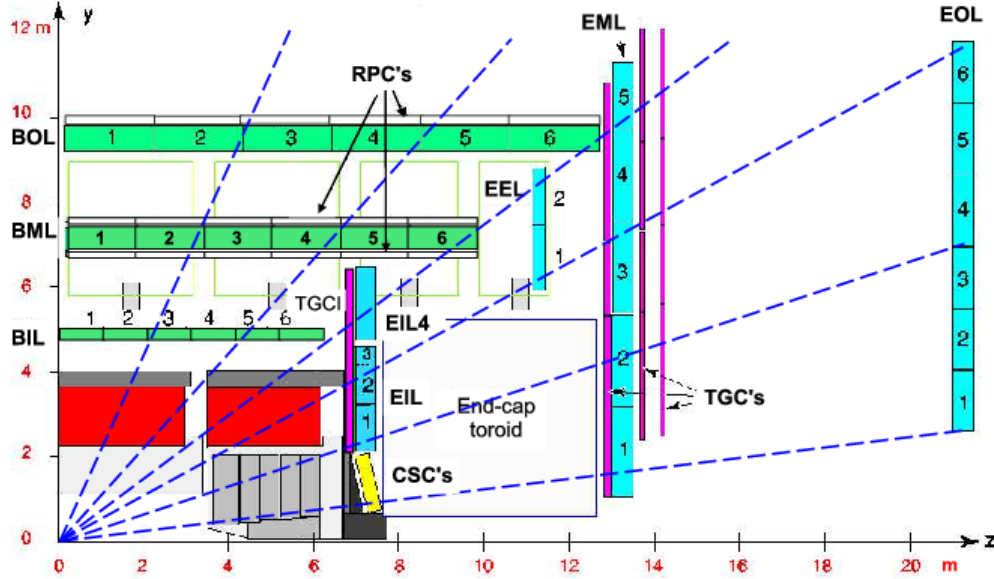
Figure 5.10: The ATLAS muon spectrometer



830 5.4 Muon Spectrometer

831 The muon spectrometer is the final major subdetector of the ATLAS detector.
832 The muon spectrometer sits outside the hadronic calorimetry, with pseudorapidity
833 coverage out to $|\eta| < 2.7$. The MS is a huge detector, with some detector elements
834 existing as far as 11 m in radius from the interaction point. This system is used
835 almost exclusively to measure the momenta of muons; these are the only measured
836 SM particles which consistently exit the hadronic calorimeters. These systems provide
837 a rough measurement, which is used in triggering (described in Ch.5.5), and a precise
838 measurement to be used in offline event reconstruction as described in Ch.???. The
839 MS produces tracks in a similar way to the ID; the hits in each subdetector are
840 recorded and then tracks are produced from these hits. Muon spectrometer tracks are
841 largely independent of the ID tracks due to the independent solenoidal and toroidal
842 magnet systems used in the ID and MS respectively. The MS consists of four separate

Figure 5.11: A schematic in z/η showing the location of the subdetectors of the muon spectrometer

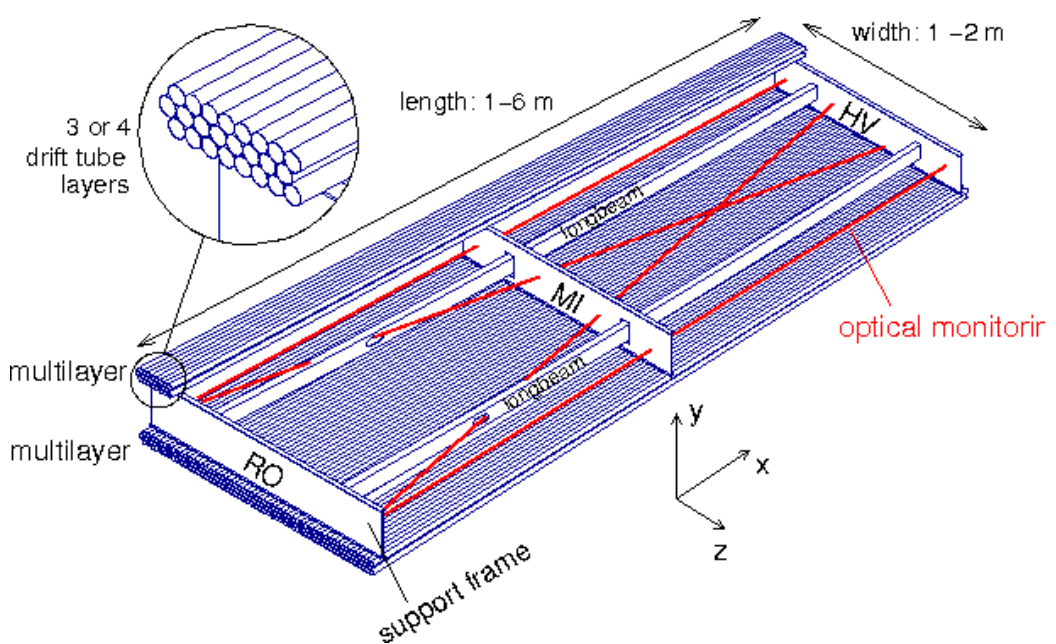


843 subdetectors: the barrel region is covered by the Resistive Plate Chambers (RPCs)
 844 and Monitored Drift Tubes (MDTs) while the endcaps are covered by MDTs, Thin
 845 Gap Chambers (TGCs), and Cathode Strip Chambers (CSCs).

846 Monitored Drift Tubes

847 The MDT system is the largest individual subdetector of the MS. MDTs provide
 848 precision measurements of muon momenta as well as fast measurements used for
 849 triggers. There are 1088 MDT chambers providing coverage out to pseudorapidity
 850 $|\eta| < 2.7$; each consists of an aluminum tube containing an argon- CO_2 gas mixture.
 851 In the center of each tube there $50\mu\text{m}$ diameter tungsten-rhenium wire at a voltage of
 852 3080 V. A muon entering the tube will induce ionization in the gas, which will “drift”
 853 towards the wire due to the voltage. One measures this ionization as a current in the
 854 wire; this current comes with a time measurement related to how long it takes the
 855 ionization to drift to the wire.

Figure 5.12: Schematic of a Muon Drift Tube chamber



856 These tubes are layered in a pattern shown in Fig.5.12. Combining the measure-
857 ments from the tubes in each layer gives good position resolution. The system consists
858 of three subsystems of these layers, at 5 m, 7m, and 9 m from the interaction point.
859 The innermost layer is directly outside the hadronic calorimeter. The combination of
860 these three measurements gives precise momenta measurements for muons.

861 Resistive Plate Chambers

862 The RPC system is alternated with the MDT system in the barrel; the first two layers
863 of RPC detectors surround the second MDT layer while the third is outside the final
864 MDT layer. The RPC system covers pseudorapidity $|\eta| < 1.05$. Each RPC consists
865 of two parallel plates at a distance of 2 mm surrounding a $\text{C}_2\text{H}_2\text{F}_4$ mixture. The
866 electric field between these plates is 4.9k kV/mm. Just as in the MDTs, an incoming
867 muon ionizes the gas, and the deposited ionization is collected by the detector (in this
868 case on the plates). It is quite fast, but with a relatively poor spatial resolution of
869 1 cm. Still, it can provide reasonable ϕ resolution due to its large distance from the
870 interaction point. This is most useful in triggering, where the timing requirements are
871 quite severe. The RPCs are also complement the MDTs by providing a measurement
872 of the non-bending coordinate.

873 Cathode Strip Chambers

874 The CSCs are used in place of MDTs in the first layer of the endcaps. This region, at
875 $2.0 < |\eta| < 2.7$, has higher particle multiplicity at the close distance to the interaction
876 point from low-energy photons and neutrons. The MDTs were not equip to deal with
877 the higher particle rate of this region, so the CSCs were designed to deal with this
878 deficiency.

879 Each CSC consists multiwire proportional chambers, oriented radially outward
880 from the interaction point. These chambers overlap partially in ϕ . The wires contain

Figure 5.13: Photo of the installation of Cathode Strip Chambers and Monitored Drift Tubes



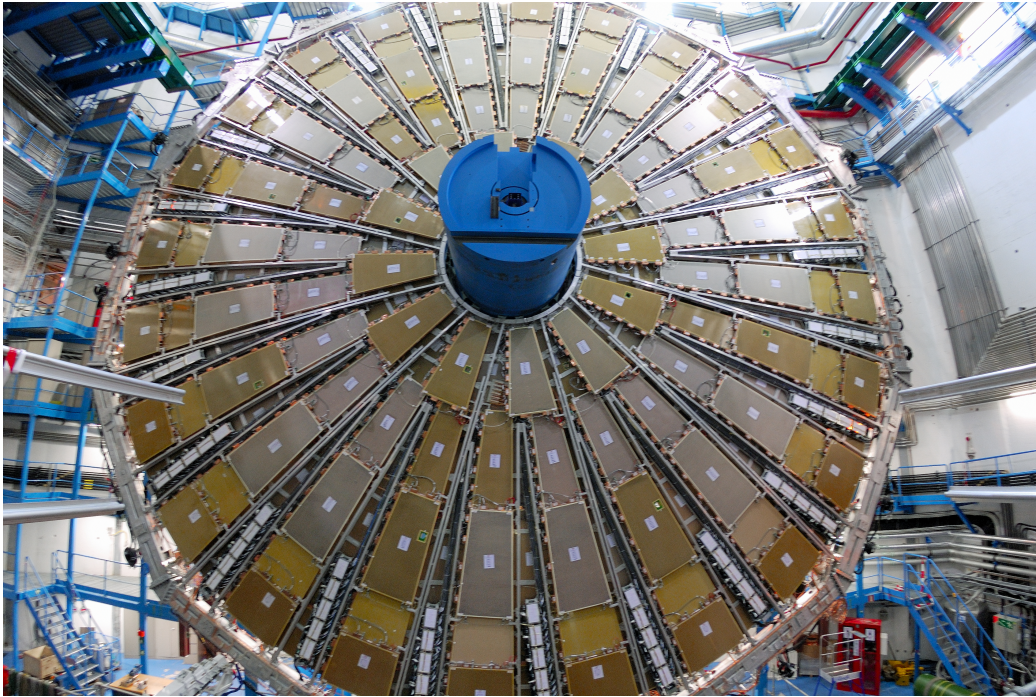
881 a gas mixture of argon and CO₂, which is ionized when muons enter. The detectors
882 operate with a voltage of 1900 V, with much lower drift times than the MDTs. They
883 provide less hits than MDTs, but their lower drift times lower uptime and reduce the
884 amount of detector overload.

885 The CSCs are arranged into four planes on the wheels of the muon spectrometer,
886 as seen in Fig.???. There are 32 CSCs in total, with 16 on each side of the detector
887 in η .

888 **Thin Gap Chambers**

889 The TGCs serve the purpose of the RPCs in the endcap at pseudorapidity of $1.05 <$
890 $|\eta| < 2.4$; they provide fast measurements used in triggering. The TGCs are also
891 multiwire proportional chambers a la the CSCs. The fast readouts necessary for
892 trigger are provided by a high electric field and a small wire-to-wire distance of 1.8
893 mm. These detectors provide both η and ϕ information, allowing the trigger to use
894 as much information as possible when selecting events.

Figure 5.14: Photo of a muon Big Wheel, consisting of Thin Gap Chambers



895 5.5 Trigger System

896 The data rate delivered by the LHC is staggering [89]. In the 2016 dataset, the
897 collision rate was 40 MHz, meaning a *bunch spacing* of 25 ns. In each of the event,
898 as we saw in Ch.??, there are many proton-proton collisions. Most of the collisions
899 are uninteresting, such as elastic scattering of protons, or even inelastic scattering
900 leading to low-energy dijet events. These types of events have been studied in detail
901 in previous experiments.

902 Even if one is genuinely interested in these events, it's *impossible* to save all of
903 the information available in each event. If all events were written "to tape" (as the
904 jargon goes), ATLAS would store terabytes of data per second. We are limited to only
905 about 1000 Hz readout by computing processing time and storage space. We thus
906 implement a *trigger* which provides fast inspection of events to drastically reduce
907 the data rate from the 40 MHz provided by the LHC to the 1000 Hz we can write to
908 tape for further analysis.

909 The ATLAS trigger system consists of a two-level trigger, known as the Level-
910 1 trigger (L1 trigger) and the High-Level Trigger (HLT)⁴. Trigger selections are
911 organized into *trigger chains*, where events passing a particular L1 trigger are passed
912 to a corresponding HLT trigger. For example, one would require a particular high- p_T
913 muon at L1, with additional quality requirements at HLT. One can also use HLT
914 triggers as prerequisites for each other, as is done in some triggers requiring both jets
915 and E_T^{miss} .

916 **Level-1 Trigger**

917 The L1 trigger is hardware-based, and provides the very fast rejection needed to
918 quickly select events of interest. The L1 trigger uses only what is known as *prompt*
919 data to quickly identify interesting events. Only the calorimeters and the triggering
920 detectors (RPCs and TGCs) of the MS are fast enough to be considered at L1,
921 since the tracking reconstruction algorithms used by the ID and the more precise
922 MS detectors are very slow. This allows quick identification of events with the
923 most interesting physical objects : large missing transverse momentum and high-
924 p_T electrons, muons, and jets.

925 L1 trigger processing is done locally. This means that events are selected without
926 considering the entire available event. Energy deposits over some threshold are
927 reconstructed as *regions of interest*. These RoIs are then compared using pattern
928 recognition hardware to “expected” patterns for the given RoIs. Events with RoIs
929 matching these expected patterns are then handed to the HLT through the Central
930 Trigger Processor. This step alone lowers the data rate down by about three orders
931 of magnitude.

⁴In Run1, ATLAS ran with a three-level trigger system. The L1 was essentially as today; the HLT consisted of two separate systems known as the L2 trigger and the Event Filter (EF). This was changed to the simpler system used today during the shutdown between Run1 and Run2.

932 **High-Level Trigger**

933 The HLT performs the next step, taking the incoming data rate from the L1 trigger
934 of ~ 75 kHz down to the ~ 1 kHz that can be written to tape. The HLT really
935 performs much like a simplified offline reconstruction, using many common quality
936 and analysis cuts to eliminate uninteresting events. This is done by using computing
937 farms located close to the detector, which process events in parallel. Individually, each
938 event which enters the computing farms takes about 4 seconds to reconstruct; the
939 HLT reconstruction time also has a long tail, which necessitates careful monitoring
940 of the HLT to ensure smooth operation.

941 HLT triggers are targetted to a particular physics process, such as a E_T^{miss} trigger,
942 single muon trigger, or multijet trigger. The collection of all triggers is known as
943 the trigger *menu*. Since many low-energy particles are produced in collisions, it is
944 necessary to set a *trigger threshold* on the object of interest; this is really just a fancy
945 naming for a trigger p_T cut. Due to the changing luminosity conditions of the LHC,
946 these thresholds change constantly, mostly by increasing thresholds with increasing
947 instantaneous luminosity. This allows an approximately constant number of events to be
948 written for further analysis. Triggers which have rates higher than those designated
949 by the menu are *prescaled*. This means writing only some fraction of the triggered
950 events. Of course, for physics analyses, one wishes to investigate all data events
951 passing some set of analysis cuts, so often one uses the “lowest threshold unprescaled
952 trigger”. *Turn-on curves* allow one to select the needed offline analysis cut to ensure
953 the trigger is fully efficient. An example turn-on curve for the E_T^{miss} triggers used in
954 the signal region of this analysis is shown in ??.

955 The full set of the lowest threshold unprescaled triggers considered here can be
956 found in Table 5.1. These are the lowest unprescaled triggers associated to the SUSY
957 signal models and Standard Model backgrounds considered in this thesis. More
958 information can be found in [89].

Table 5.1: High-Level Triggers used in this thesis. Descriptions of loose, medium, tight, and isolated can be found in [89]. The d_0 cut refers to a quality cut on the vertex position; this was removed from many triggers in 2016 to increase sensitivity to displaced vertex signals. For most triggers, the increased thresholds in 2016 compared to 2015 were designed to keep the rate approximately equal. The exception is the E_T^{miss} triggers; see 5.5.

Physics Object	Trigger	p_T (GeV)	Threshold	Level-1 Seed	Additional Requirements	Approximate Rate (Hz)
2015 Data						
E_T^{miss}	HLT_xe70	70		L1_XE50	-	60
	HLT_mu24_iloose_L1 M145			L1_MU15	isolated, loose	130
Muon	HLT_mu50	50		L1_MU15	-	30
Muon	HLT_e24_1hmedium_l1 B4se_L1EM20VH			L1_EM20VH	medium OR isolated, loose	140
Electron	HLT_e60_1hmedium	60		L1_EM20VH	medium	10
Electron	HLT_e120_1hloose	120		L1_EM20VH	loose	<10
Electron	HLT_g120_loose	120		L1_EM20VH	loose	20
2016 Data						
E_T^{miss}	HLT_xe100_mht_L1 XE500			L1_XE50	-	180
	HLT_mu24_ivarmedium 4			L1_MU20	medium	120
Muon	HLT_mu50	50		L1_MU20	-	40
Muon	HLT_e24_l1tight_no d4ivarloose			L1_EM22VHT	tight with no d_0 or loose	110
Electron	HLT_e60_1hmedium_no d0			L1_EM22VHT	medium with no d_0	10
Electron	HLT_e140_1hloose_no d0			L1_EM22VHT	loose with no d_0	<10
Electron	HLT_g140_loose	140		L1_EM22VHT	loose	20

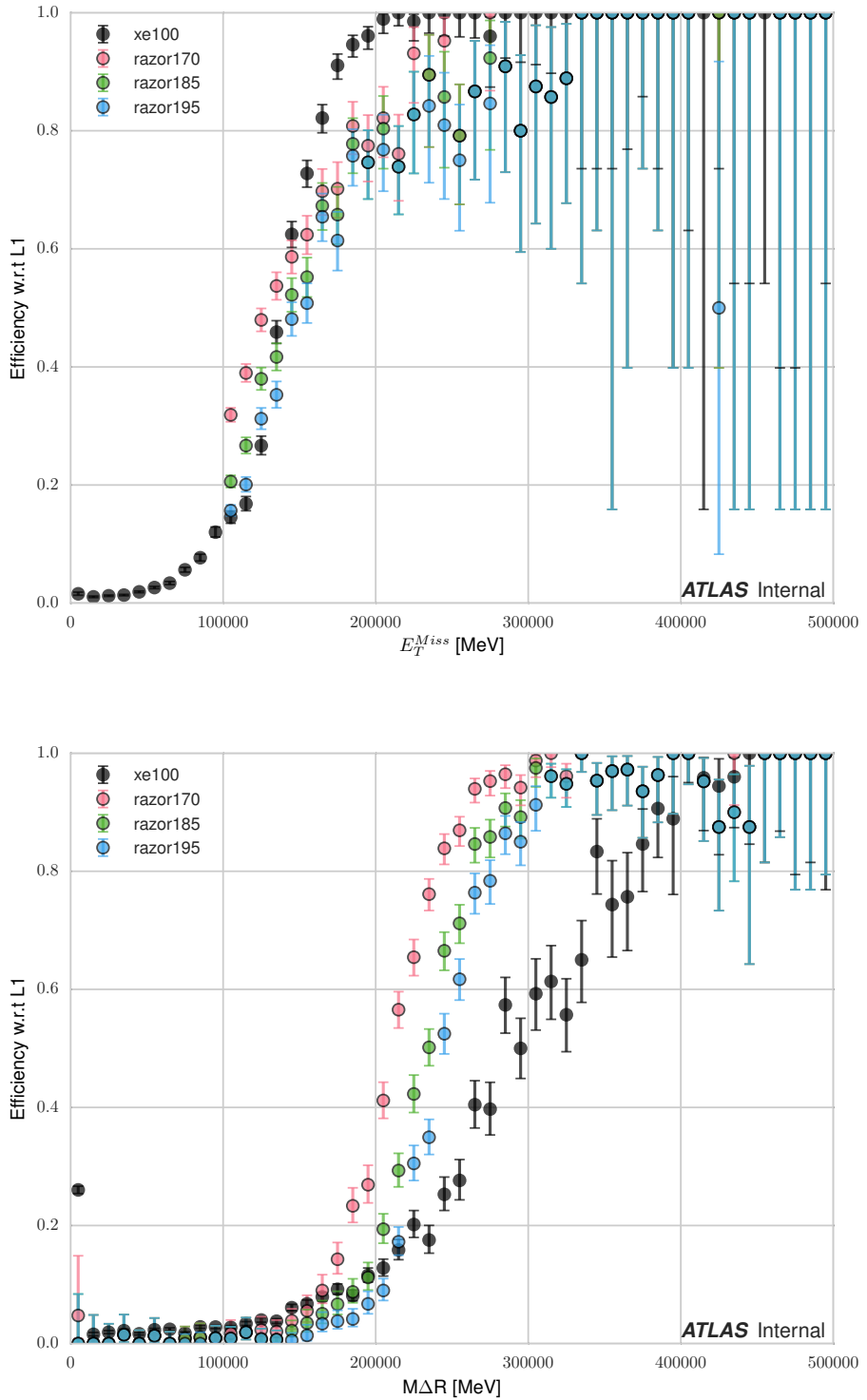
959 **Razor Triggers**

960 For the analysis presented in this thesis, the *razor triggers* were developed. These are
961 topological triggers, combining both jet and E_T^{miss} information to select interesting
962 events. In particular, they use the razor variable M_{Δ}^R which will be described in
963 Chapter ??.

964 Based on 2015 run conditions, these triggers would have allowed the use of a lower
965 offline E_T^{miss} cut with a similar rate to the nominal E_T^{miss} triggers. This can be seen
966 in the turn-on curves shown in Figure 5.15. The razor triggers are fully efficient at
967 nearly 100 GeV lower than the corresponding E_T^{miss} triggers in M_{Δ}^R .

968 There was a quite big change in the 2016 menu, which increased the rate given to
969 E_T^{miss} triggers drastically. This can be seen in the difference in rate shown between
970 E_T^{miss} triggers in 2015 and 2016 in Table 5.1. This allowed the E_T^{miss} triggers to
971 maintain a lower threshold throughout the dataset used in this thesis.

Figure 5.15: Turn-on curves for the razor triggers and nominal E_T^{miss} trigger. The razor triggers show a much sharper turn-on in M_{Δ}^R relative to the E_T^{miss} trigger. The converse is true for the E_T^{miss} triggers.



Event Reconstruction

974 This chapter describes the reconstruction algorithms used within ATLAS.[TODO: cite](#)
975 [fermilab lectures](#) We will make the distinction between the “primitive” objects which
976 are reconstructed from the detector signals from the “composite” physics objects we
977 use in measurements and searches for new physics.

978 6.1 Primitive Object Reconstruction

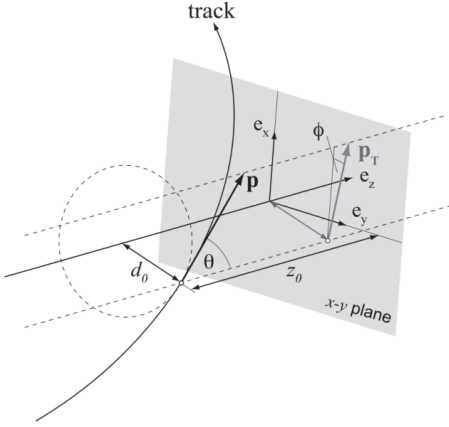
979 The primitive objects reconstructed by ATLAS are *tracks* and (calorimeter) *clusters*.
980 These are reconstructed directly from tracking hits and calorimeter energy deposits
981 into cells. Tracks can be further divided into inner detector and muon spectrom-
982 eter tracks. Calorimeter clusters can be divided into sliding-window clusters and
983 topological clusters (topoclusters).

984 Inner Detector Tracks

985 [TODO: cite paper/note](#)

986 Inner detector tracks are reconstructed from hits in the inner detector. These hits
987 indicate that a charged particle has passed through the detector material. Due to the
988 2 T solenoid in the inner detector, the hits associated with any individual particle
989 will be curved; this allows one to measure the momentum of the particle. In any
990 given event, there is upwards of [TODO: number](#), making it impossible to do any sort
991 of combinatorics to reconstruct tracks¹. There are two algorithms used by ATLAS

Figure 6.1: The parameters associated to a track.



992 track reconstruction, known as *inside-out* and *outside-in*.

993 ATLAS first employs the inside-out algorithm. First, one assumes the track begins
 994 at the interaction point. Moving out from the interaction point, one creates track
 995 seeds. Track seeds are proto-tracks constructed from three hits; these hits can be
 996 distributed as three pixel hits, two pixel hits and one SCT hit, or three SCT hits.
 997 One extrapolates the track and uses a combinatorial Kalman filter **TODO: cite**, which
 998 adds the rest of the pixel and SCT hits to the seeds. This is done seed by seed, so it
 999 avoids the combinatorial complexity involved with checking all hits with all seeds. At
 1000 this point, the algorithm applies an additional filter to avoid ambiguities from nearby
 1001 tracks. The TRT hits are then added to the seeds in the same procedure; in this way,
 1002 all hits are associated to a track.

1003 The next step is to figure out the correct kinematics of the track. This is
 1004 done by applying a fitting algorithm which outputs the best-fit track parameters
 1005 by minimizing the track distance from hits, weighted by each hit's resolution. These
 1006 parameters are $(d_0, z_0, \eta, \phi, q/p)$ where d_0 (z_0) is the transverse (longitudinal) impact
 1007 parameter and q/p is the charge over the track momenta. This set of parameters
 1008 uniquely defines the trajectory of the charged particle associated to the track; an
 1009 illustration of a track with these parameters is shown in Fig.6.1.

1010 The other track reconstruction algorithm is the outside-in algorithm. As the name
1011 implies, in this case, we start from the outside of the inner detector, in the TRT, and
1012 extend the tracks in. One begins by seeding from TRT hits, and extending the track
1013 back towards the center of the detector. The same fitting procedure is used as in
1014 the inside-out algorithm to find the optimal track parameters. This algorithm is
1015 particularly important for finding tracks which originate from interactions with the
1016 detector material, especially the SCT. For tracks from primary vertices, this often
1017 finds the same tracks as the inside-out algorithm, providing an important check on
1018 the consistency of the tracking procedure.

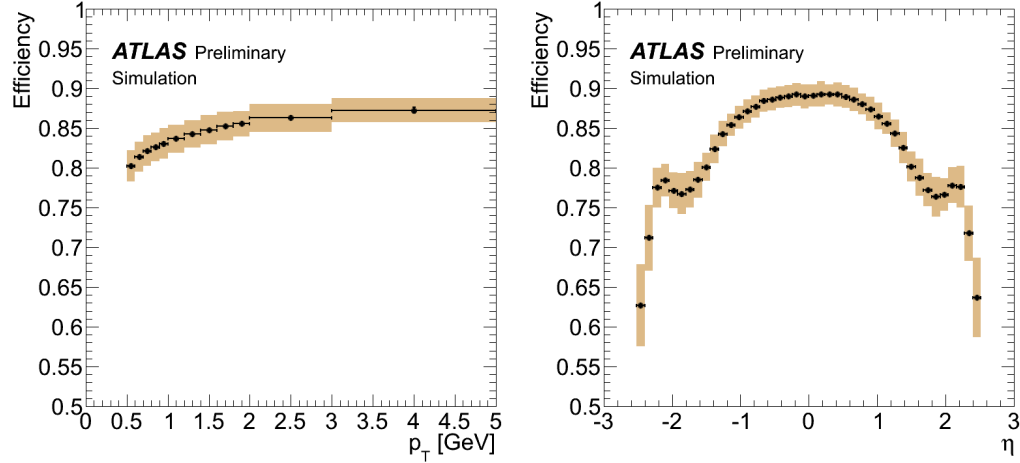
1019 In the high luminosity environment of the LHC, even the tracks reconstructed
1020 from precision detectors such as those of ATLAS inner detector can sometimes lead
1021 to fake tracks from simple combinatoric chance. Several quality checks are imposed
1022 after track fitting which reduce this background. Seven silicon (pixel + SCT) hits
1023 are required for all tracks. No more than two holes are allowed in the pixel detector;
1024 holes are expected measurements from the track that are missing in the pixel detector.
1025 Finally, tracks with poor fit quality, as measured by χ^2/ndf , are also rejected. Due
1026 to the high quality of the silicon measurements in the pixel detector and SCT, these
1027 requirements give good track reconstruction efficiency, as seen in Fig.6.2 for simulated
1028 events[[ATL-COM-PHYS-2012-1541](#)].

1029 Sliding-window clusters

1030 The sliding-window algorithm is a way to combine calorimeter cells into composite
1031 objects (clusters) to be used as inputs for other algorithms[[90](#)]. Sliding-window
1032 clusters are the primary inputs to electron and photon reconstruction, as described
1033 below. As described in Ch.??, the electromagnetic calorimeter has high granularity,
1034 with a cell size of $(\eta, \phi) = (.025, .025)$ in the coarsest second layer throughout most
1035 of the calorimeter. The “window” consists of 3 by 5 cells in the (η, ϕ) space; all

Figure 6.2: Track reconstruction efficiency as a function of track p_T and η . The efficiency is defined as the number of reconstructed tracks divided by the number of generate charged particles.

(a) Track reconstruction as a function of p_T . (b) Track reconstruction as a function of η .



1036 layers are added on this same 2D space. One translates this window over the space
 1037 and seeds a cluster whenever the energy sum of the cells is maximized. If the seed
 1038 energy is greater than 2.5 GeV, this seed is called a sliding-window cluster. This
 1039 choice was motivated to optimize the reconstruction efficiency of proto-electrons and
 1040 proto-photons while rejecting fakes from electronic noise and additional particles from
 1041 pileup vertices.

1042 Topological clusters

1043 Topoclusters are the output of the algorithm used within ATLAS to combine
 1044 hadronic and electromagnetic calorimeter cells in a way which extracts signal from
 1045 a background of significant electronic noise[91]. They are the primary input to the
 1046 algorithms which reconstruct jets.

1047 Topological clusters are reconstructed from calorimeter cells in the following way.
 1048 First, one maps all cells onto a single $\eta - \phi$ plane so one can speak of *neighboring*
 1049 cells. Two cells are considered neighboring if they are in the same layer and directly

1050 adjacent, or if they are in adjacent layers and overlap in $\eta - \phi$ space. The *significance*
1051 ξ_{cell} of a cell during a given event is

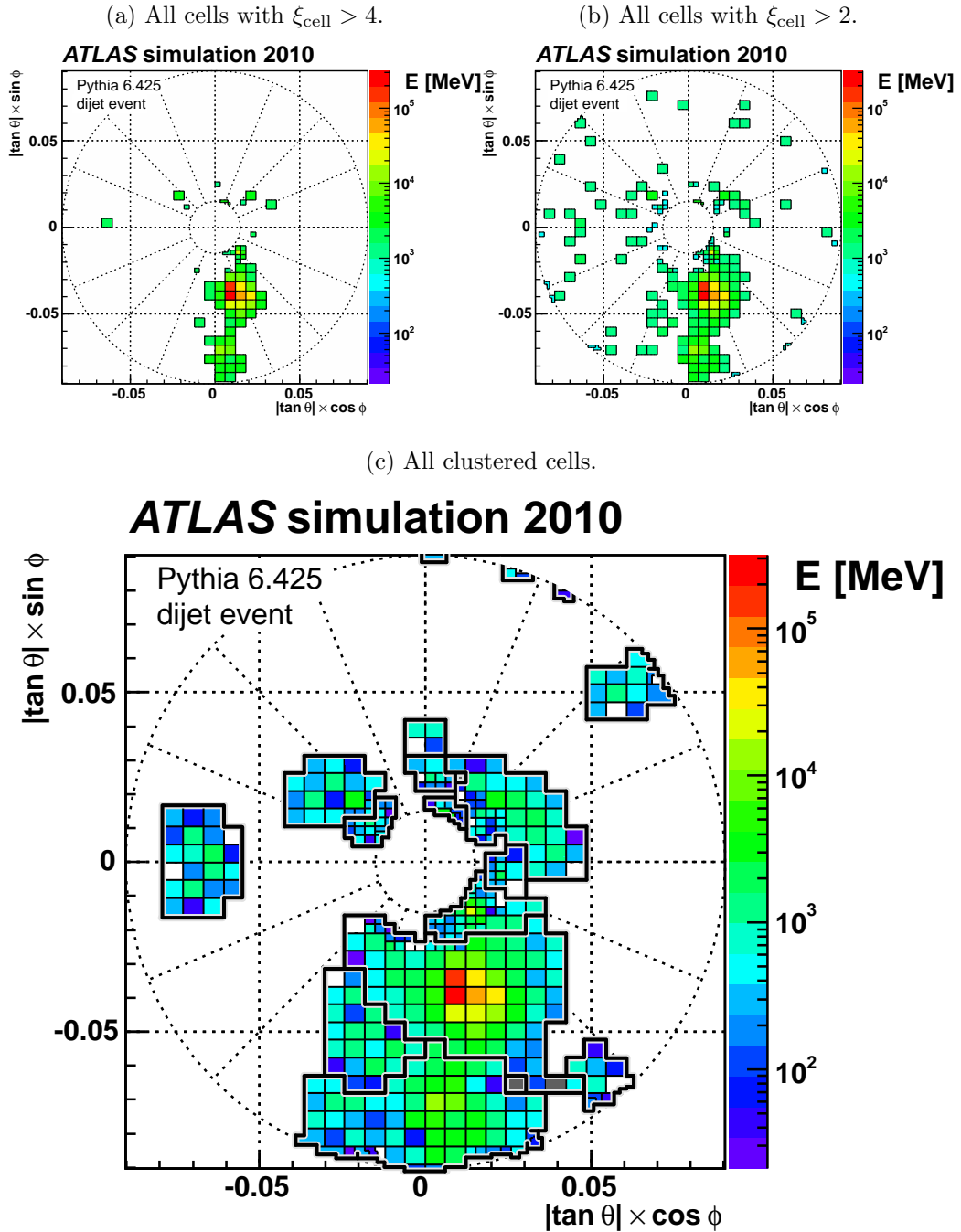
$$\xi_{\text{cell}} = \frac{E_{\text{cell}}}{\sigma_{\text{noise,cell}}} \quad (6.1)$$

1052 where $\sigma_{\text{noise,cell}}$ is measured for each cell in ATLAS and E_{cell} measures the current
1053 energy level of the cell. One thinks of this as the measurement of the energy *over*
1054 *threshold* for the cell.

1055 Topocluster *seeds* are defined as calorimeter cells which have a significance $\xi_{\text{cell}} >$
1056 4. These are the inputs to the algorithm; one iteratively tests all cells adjacent to these
1057 seeds for $\xi_{\text{cell}} > 2$. Each cells passing this selection is then added to the topocluster,
1058 and the procedure is repeated. When the algorithm reaches the point where there
1059 are no additional adjacent cells with $\xi_{\text{cell}} > 2$, every positive-energy cell adjacent to
1060 the current proto-cluster is added. This collection of cells is summed; the summed
1061 object is known as a topocluster. An example of this procedure for a simulation dijet
1062 event is shown in Fig.6.3.

1063 There are two calibrations used for clusters.**TODO: cite** These are known as the
1064 electromagnetic (EM) scale and the local cluster weighting (LCW) scale. The EM
1065 scale is the energy read directly out of the calorimeters as described. This scale is
1066 appropriate for electromagnetic processes. The LCW scale applies additional scaling
1067 to the clusters based on the shower development. This allows the cluster energy to be
1068 corrected for calorimeter non-compensation and the differences in the hadronic and
1069 electromagnetic calorimeters' responses. This scale provides additional corrections
1070 that improve the accuracy of hadronic energy measurements. This thesis only uses the
1071 EM scale corrections unfortunately; LCW scaling requires additional measurements
1072 that only became available with additional data. Due to the jet calibration procedure
1073 that we will describe below, it is also a relatively complicated procedure to rederive
1074 the “correct” jet energy.

Figure 6.3: Example of topoclustering on a simulated dijet event.



1075 **Muon Spectrometer Tracks**

1076 Muon spectrometer tracks are fit using the same algorithms as the ID tracks, but
1077 different subdetectors. The tracks are seeded by hits in the MDTs or CSCs. After
1078 seeding in the MDTs and CSCs, the hits from all subsystems are refit as the final
1079 MS track. These tracks are used as inputs to the muon reconstruction, as we will see
1080 below.

1081 **6.2 Physics Object Reconstruction and Quality**
1082 **Identification**

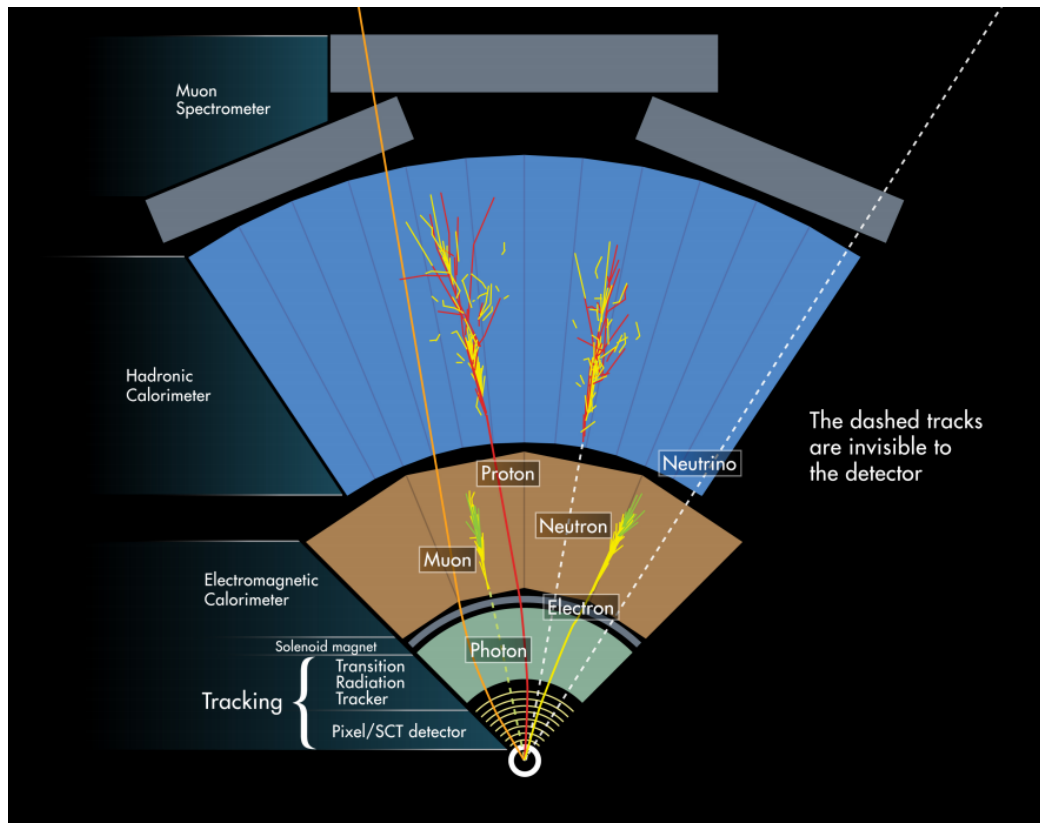
1083 There are essentially six objects used in ATLAS searches for new physics: electrons,
1084 photons, muons, τ -jets, jets, and E_T^{miss} . The reconstruction of these objects is
1085 described here; in this thesis, τ lepton jets are not treated differently from other
1086 hadronic jets. A very convenient summary plot is shown in Fig.6.4. This process
1087 produces candidate objects, which are then identified by quality.

1088 One often wishes to understand “how certain” we are that a particular object
1089 is truly the underlying physics object. In ATLAS, we often generically consider, in
1090 order, *very loose*, *loose*, *medium*, and *tight* objects². These are ordered in terms of
1091 decreasing object efficiency, or equivalently, decreasing numbers of fake objects. We
1092 will also describe briefly the classification of objects into these categories.

1093 In this thesis, we present a search for new physics in a zero lepton final state; we
1094 will provide additional details about jet and E_T^{miss} reconstruction.

² These are not all used for all objects, but it’s conceptually useful to think of these different categories.

Figure 6.4: The interactions of particles with the ATLAS detector. Solid lines indicate the particle is interacting with the detector, while dashed lines are shown where the particle does not interact.



1095 Electrons and Photons

1096 Reconstruction

1097 The reconstruction of electrons and photons (often for brevity called “electromagnetic
 1098 objects”) is very similar [PERF-2013-03 , 92, 93]. This is because the reconstruction
 1099 begins with the energy deposit in the calorimeter in the form of an electromagnetic
 1100 shower. For any incoming e/γ , this induces many more electrons and photons in the
 1101 shower; the measurement in the calorimeter is similar for these two objects.

1102 One thus begins the reconstruction of electromagnetic objects from the sliding-
 1103 window clusters reconstructed from the EM calorimeter, as described in Sec.6.1.
 1104 These $E > 2.5$ GeV clusters provide the primary seed for electrons and photons. One then
 1105 looks for all ID tracks within $\Delta R < 0.3$.**TODO: check delta R defined somewhere**

1106 We “match” the track and cluster if they are within $\Delta\phi < 0.2$ in the direction of
1107 track curvature, or $\Delta\phi < 0.05$ in the direction opposite the track curvature. Those
1108 track-cluster seeds with tracks pointing to the primary vertex are reconstructed as
1109 electrons.

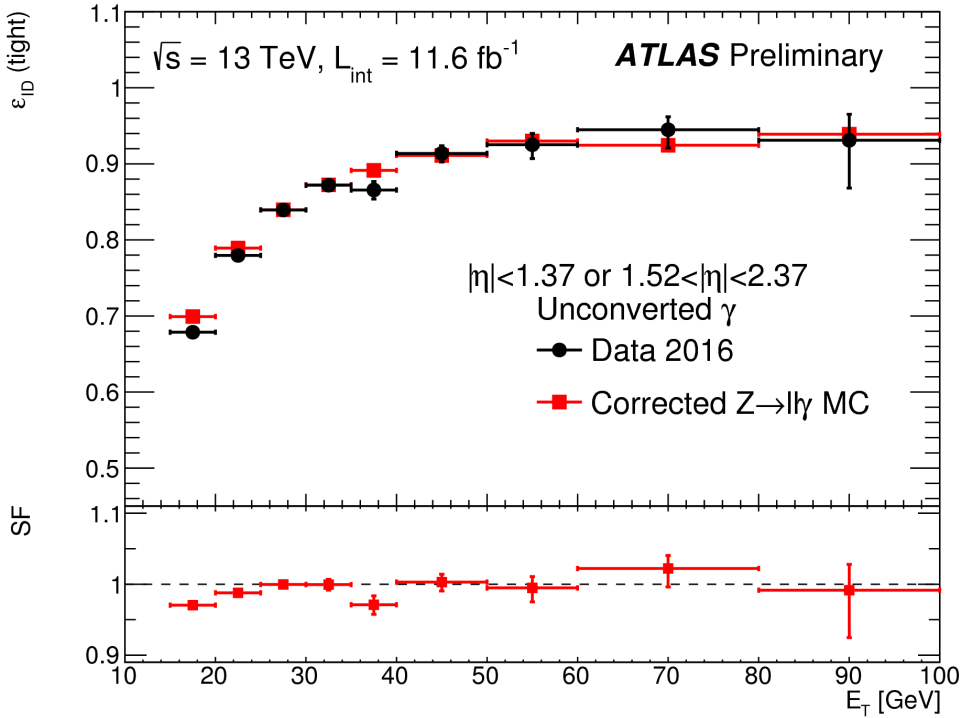
1110 For photons, we have two options to consider, known as *converted* and *unconverted*
1111 photons. Due to the high energy of the LHC collisions, typical photons have energy
1112 ~ 1 GeV; at this scale, photons interact almost exclusively via pair-production in the
1113 presence of the detector material **TODO: DIAGRAM**. If the track-cluster seed has
1114 a track which does not point at the primary vertex, we reconstruct this object as a
1115 converted photon. This happens since the photon travels a distance before decay into
1116 two electrons, and see the tracks coming from this secondary vertex. Those clusters
1117 which do not have any associated tracks are then reconstructed as an unconverted
1118 photon.

1119 The final step in electromagnetic object reconstruction is the final energy value
1120 assigned to these objects; this process is different between electrons and photons due
1121 to their differing signatures in the EM calorimeter. In the barrel, electrons energies
1122 are assigned as the sum of the 3 clusters in η and 7 clusters in ϕ to account for the
1123 electron curving in the ϕ direction. Barrel photons are assigned the energy sum of
1124 (3, 5) clusters in (η, ϕ) space. In the endcap, the effect of the magnetic field on the
1125 electrons is smaller, and there is a coarser granularity. Both objects sum the (5, 5)
1126 clusters for their final energy value.

1127 Quality Identification

1128 Electrons have a number of important backgrounds which can give fakes. Fake
1129 electrons come primarily from secondary vertices in hadron decays or misidentified
1130 hadronic jets. To reduce these backgrounds, quality requirements are imposed on
1131 electron candidates. Loose electrons have requirements imposed on the shower

Figure 6.5: Unconverted photon efficiency as measured in [ATL-PHYS-PUB-2016-015].



1132 shapes in the electromagnetic calorimeter and on the quality of the associated ID
 1133 track. There is also a requirement that there is a small energy deposition in the
 1134 hadronic calorimeter behind the electron, to avoid jets being misidentified as electrons
 1135 (low hadronic leakage). Medium and tight electrons have increasingly stronger
 1136 requirements on these variables, and additional requirements on the isolation (as
 1137 measured by ΔR) and matching of the ID track momentum and the calorimeter
 1138 energy deposit.

1139 Photons are relatively straightforward to measure, since there are few background
 1140 processes[ATL-PHYS-PUB-2016-015]. The primary one is pion decays to two
 1141 photons, which can cause a jet to be misidentified as photon. Loose photons have
 1142 requirements on the shower shape and hadronic leakage. Tight photons have tighter
 1143 shower shape cuts, especially on the high granularity first layer of the EM calorimeter.
 1144 The efficiency for unconverted tight photons as a function of p_T is shown in

1145 **Muons**

1146 **Reconstruction**

1147 Muons are reconstructed using measurements from all levels of the ATLAS detec-
1148 tor[94]. They leave a ID track, a small, characteristic deposition in the EM calorime-
1149 ter, and then a track in the muon spectrometer. The primary reconstruction technique
1150 produces a so-called *combined* muon. “Combined” means using a combination of the
1151 ID and MS tracks to produce the final reconstructed muon kinematics. This is done
1152 by refitting the hits associated to both tracks, and using this refit track for the muon
1153 kinematics. This process produces the best measured muons, although several other
1154 worse algorithms are used when the full detector information is missing. An example
1155 is in the region $2.5 < |\eta| < 2.7$ outside the ID acceptance; in this region, MS tracks
1156 are used without the corresponding ID tracks.

1157 **Quality Identification**

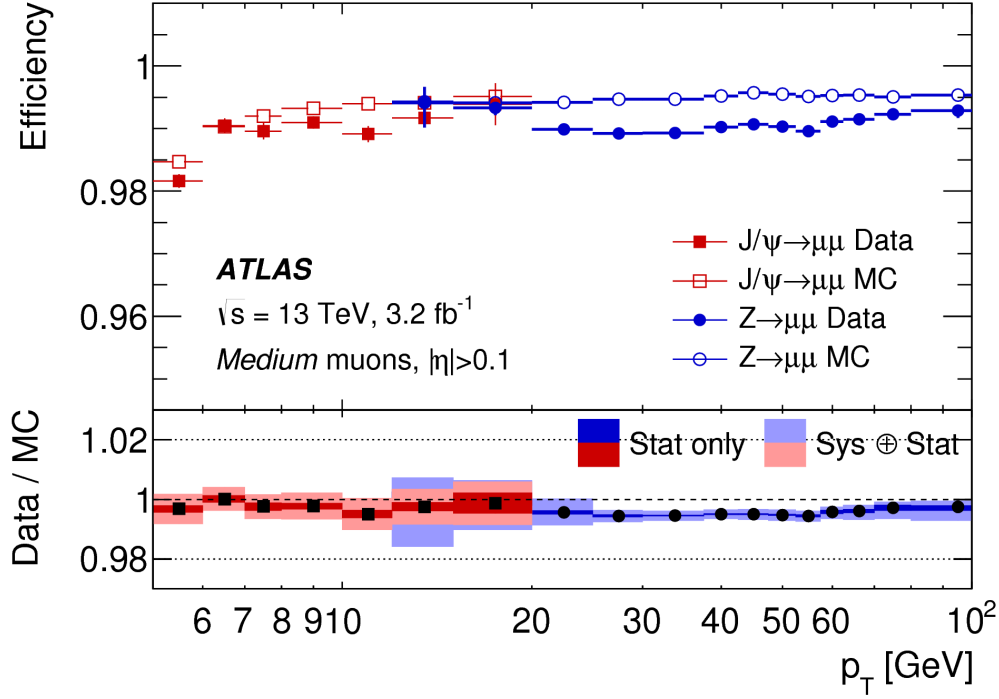
Several additional criteria are used to assure muon measurements are free of significant background contributions, especially from pion and kaon decays to muons. Muons produced via these decay processes are often characterized by a “kink”. Candidate muons with a poor fit quality, characterized by $\chi^2/\text{n.d.f.}$, are thus rejected. Additionally, the absolute difference in momentum measurements between the ID and MS provide another handle, since the other decay products from hadron decays carry away some amount of the initial hadron momentum. This is measured by

$$\rho' = \frac{|p_T^{\text{ID}} - p_T^{\text{MS}}|}{p_T^{\text{Combined}}}. \quad (6.2)$$

Additionally, there is a requirement on the q/p significance, defined as

$$S_{q/p} = \frac{|(q/p)^{\text{ID}} - (q/p)^{\text{MS}}|}{\sqrt{\sigma_{\text{ID}}^2 + \sigma_{\text{MS}}^2}}. \quad (6.3)$$

Figure 6.6: Medium muon efficiency as measured in [94].



1158 The $\sigma_{ID,MS}$ in the denominator of Eq.6.3 are the uncertainties on the corresponding
 1159 quantity from the numerator. Finally, cuts are placed on the number of hits in the
 1160 various detector elements.

1161 Subsequently tighter cuts on these variables allow one to define the different muon
 1162 identification criteria. Loose muons have the highest reconstruction efficiency, but
 1163 the highest number of fake muons, since there are no requirements on the number
 1164 of subdetector hits and the loosest requirements on the suite of quality variables.
 1165 Medium muons consist of Loose muons with tighter cuts on the quality variables;
 1166 they also require more than three MDT hits in at least two MDT layers. These are
 1167 the default used by ATLAS analyses. Tight muons have stronger cuts than those of
 1168 the medium selection, and reducing the reconstruction efficiency. The reconstruction
 1169 efficiency as a function of p_T can be seen for Medium muons in Fig.6.6.

1170 **Jets**

1171 **TODO: cite paper/note**

1172 Jets are composite objects corresponding to many physical particles. This is a
1173 striking difference from the earlier particles. Fortunately, we normally (and in this
1174 thesis) care about the original particle produced in primary collision. In the SM, this
1175 corresponds to quarks and gluons; due to the hadronization process described in 2, free
1176 quarks and gluons spontaneously hadronize and produce a hadronic shower, which
1177 we call a jet. These showers can be measured by the EM and hadronic calorimeters,
1178 and the charged portions can be measured in the ID. The first question is how to
1179 combine these measurements into a composite object representing the underlying
1180 physical parton. This is done via jet algorithms.

1181 **Jet Algorithms**

1182 It might seem straightforward to combine the underlying physical particles into a
1183 jet. There are three important characteristics required for any jet reconstruction
1184 algorithm to be used by ATLAS.

1185 • Collinear safety - if any particle with four-vector p is replaced by two particles
1186 of p_1, p_2 with $p = p_1 + p_2$, the subsequent jet should not change

1187 • Radiative (infrared) safety - if any particle with four-vector p radiates a particle
1188 of energy $\alpha \rightarrow 0$, the subsequent jet should not change

1189 • Fast - the jet algorithm should be “fast enough” to be useable by ATLAS
1190 computing resources

1191 The first two requirements can be seen in terms of requirements on soft gluon emission.
1192 Since partons emit arbitrarily soft gluons freely, one should expect the algorithms

1193 to not be affected by this emission. The final requirement is of course a practical
1194 limitation.

The algorithms in use by ATLAS (and CMS) which satisfies these requirements are collectively known as the k_T algorithms [95–97]. These algorithms iteratively combine the “closest” objects, defined using the following distance measures :

$$d_{ij} = \min(k_{T,i}^{2p}, k_{T,j}^{2p}) \frac{\Delta_{ij}^2}{R^2} \quad (6.4)$$
$$d_{iB} = k_{Ti}^{2p}$$

1195 In Eq.6.4, k_T , i is the transverse momentum of i -th jet *constituent*, Δ_{ij} is the angular
1196 distance between the constituents. Both R and p are adjustable parameters; R is
1197 known as the (jet) *cone size* and p regulates the power of the energy vs the geometrical
1198 scales. The algorithm sequence, for a given set of objects i with four-vector k :

- 1199 1. Find the minimum distance in the set of all d_{ij} and d_{iB} .
- 1200 2. If the distance is one of the d_{ij} , combine the input pair of object i, j and return
1201 to (1). If the distance is one of the d_{iB} , remove the object from the list, call it
1202 a jet, and return to (1).

1203 This process ends when all objects i have been added to a jet.

1204 Any choice of (p, R) has the requirements of collinear and radiative safety. In
1205 essence, the choice is then to optimize based on speed and the potential for new
1206 physics discoveries. In ATLAS, we make the choice of $p = -1$; this is also known as
1207 the *anti- k_T* algorithm. The choice of $R = 0.4$ is used for the distance parameter of
1208 the jets.

1209 The primary “nice” quality of this algorithm can be seen with the following
1210 example. Consider three inputs to an anti- k_T algorithm, all with $\eta = 0$:

- 1211 • Object 1 : $(p_T, \phi) = (30 \text{ GeV}, 0)$
- 1212 • Object 2 : $(p_T, \phi) = (20 \text{ GeV}, -0.2)$

- 1213 • Object 3 : $(p_T, \phi) = (10 \text{ GeV}, 0.2)$

- 1214 • Object 4 : $(p_T, \phi) = (1 \text{ GeV}, 0.5)$

1215 . In the case shown, it seems natural to first combine the “bigger” objects 1 and 2.
1216 These then pick up the extra small object 3, and object 4 is not included in the jet.
1217 This is exactly what is done by the anti- k_T algorithm. The (normal) k_T algorithm with
1218 $p = 1$ instead combines the smallest objects, 3 and 4, first. Object 1 and 2 combine
1219 to form their own jet, instead of these jets picking up object 3. This behavior is not
1220 ideal due to the effects of pileup, as we will see in the next section.

1221 Jet Reconstruction

1222 In ATLAS, jets are reconstructed using multiple different objects as inputs, including
1223 tracks, “truth” objects, calorimeter clusters, and *particle flow objects* (PFOs) **TODO:**
1224 **cite pflow paper**. For physics analyses, ATLAS primarily uses jets reconstructed from
1225 calorimeter clusters, but we will describe the others here, as they are often used for
1226 derivations of systematic uncertainties or future prospects.

1227 Calorimeter jets are reconstructed using topoclusters using the anti- k_T algorithm
1228 with $R = 0.4$. The jet reconstruction algorithm is run on the collection of all
1229 topoclusters reconstructed as in Sec.6.1. Both EM and LCW scale clusters are used
1230 in the ATLAS reconstruction software and produce two sets of jets for analysis. As
1231 stated above, this thesis presents an analysis using jets reconstructed using EM scale
1232 clusters; we refer to these as *EM jets*.

1233 Tracks can be used as inputs to jet reconstruction algorithms. Jets reconstructed
1234 from tracks are known as *track jets*. Since the ID tracks do not measure neutral
1235 objects, these jets measure an incorrect energy. However, these are still useful for
1236 checks and derivations of systematic uncertainties.

1237 *Truth* jets are reconstructed from *truth* particles. In this case, truth is jargon
1238 for simulation; in simulation, the actual simulated particles are available and used as
1239 inputs to the jet reconstruction algorithms. Similarly to track jets, these are not useful
1240 in and of themselves. Instead, truth jets are used for comparisons and derivations of
1241 systematic uncertainties.

1242 The last object generally used as inputs to jet reconstruction algorithms are
1243 *particle flow objects* (PFOs) *TODO: cite atlas paper and theory paper maybe?*
1244 Particle flow objects are reconstructed by associating tracks and clusters through
1245 a combination of angular distance measures and detector response measurements
1246 to create a composite object which contains information from both the ID and the
1247 calorimeters. For calorimeter clusters which do not have any associated ID track,
1248 the cluster is simply the PFO. The natural association between tracks and clusters
1249 provides easy pileup subtraction since tracks are easily associated to the primary
1250 vertex. This technique is generally used in CMS, and ATLAS has been slow to
1251 adopt the same. As pileup has increased, the utility of using PFOs as inputs to jet
1252 reconstruction has increased as well.

1253 Jet Calibration

1254 Jets as described in the last section are still *uncalibrated*. Even correcting the cluster
1255 energies using the LCW does not fully correct the jet energy, due to particles losing
1256 energy in the calorimeters. The solution to this is the *jet energy scale* (JES). The
1257 JES is a series of calibrations which on average restore the correct truth jet energy
1258 for a given reconstructed jet. These steps are shown in Fig.6.7 and described here.

1259 The first step is the origin correction; this adjusts the jet to point at the primary
1260 vertex. Next, is the jet-area based pileup correction. This step subtracts the
1261 “average” pileup as measured by the energy density ρ outside of the jets and assumes
1262 this is a good approximation for the pileup inside the jet. One then removes energy

1263 $\Delta E = \rho \times A_{\text{jet}}$ in this step. The residual pileup correction makes a final offset
1264 correction by parametrizing the change in jet energy as a function of the number of
1265 primary vertices N_{PV} and the average number of interactions μ .

1266 The next step is the most important single correction; it is known as the
1267 AbsoluteEtaJES step. Due to the use of non-compensation and sampling calorimeters
1268 in ATLAS, the measured energy of a jet is a fraction of the true energy of the outgoing
1269 parton. Additionally, due to the use of different technologies and calorimeters
1270 throughout the detector, there are directional biases induced by these effects. The
1271 correction bins a multiplicative factor in p_{T} and η which scales the reconstructed jets
1272 to corresponding truth jet p_{T} . This step does not entirely correct the jets, since it is
1273 entirely a simulation-based approach.

1274 The final steps are known as the global sequential calibration (GSC) and the
1275 residual in-situ calibration. The GSC uses information about the jet showering shape
1276 to apply additional corrections based on the expected shape of gluon or quark jets.
1277 The final step is the residual in-situ calibration, which is only applied to data. This
1278 step uses well-measured objects recoiling off a jet to provide a final correction to the
1279 jets in data. In the low p_{T} region ($20 \text{ GeV} \sim < p_{T,\text{jet}} \sim < 200 \text{ GeV}$), $Z \rightarrow ll$ events are
1280 used as a reference object. In the middle p_{T} region ($100 \text{ GeV} \sim < p_{T,\text{jet}} \sim < 600 \text{ GeV}$),
1281 the reference object is a photon, while in the high p_{T} region ($p_{T,\text{jet}} \sim > 200 \text{ GeV}$), the
1282 high p_{T} jet is compared to multiple smaller p_{T} jets; the reference object is this group
1283 of multijets. After this final correction, the data and MC scales are identical up to
1284 the corresponding uncertainties; the combined JES uncertainty as a function of p_{T} is
1285 shown in Fig.??.

1286 Jet Vertex Tagger

1287 The *jet vertex tagger* (JVT) TODO: cite technique is used to separate pileup jets
1288 from those associated to the hard primary vertex. The technique for doing so

Figure 6.7: The steps used by ATLAS to calibrate jets

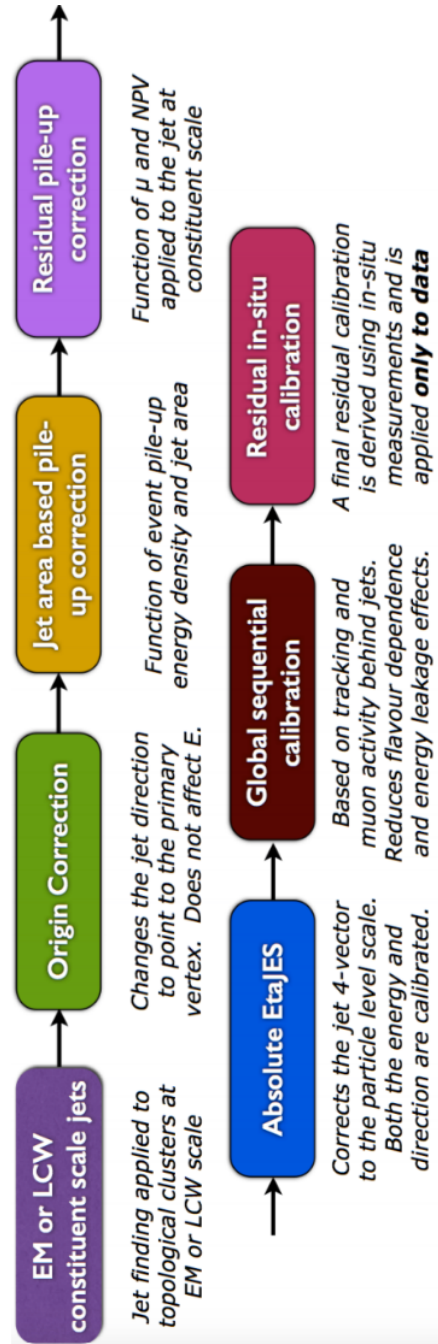
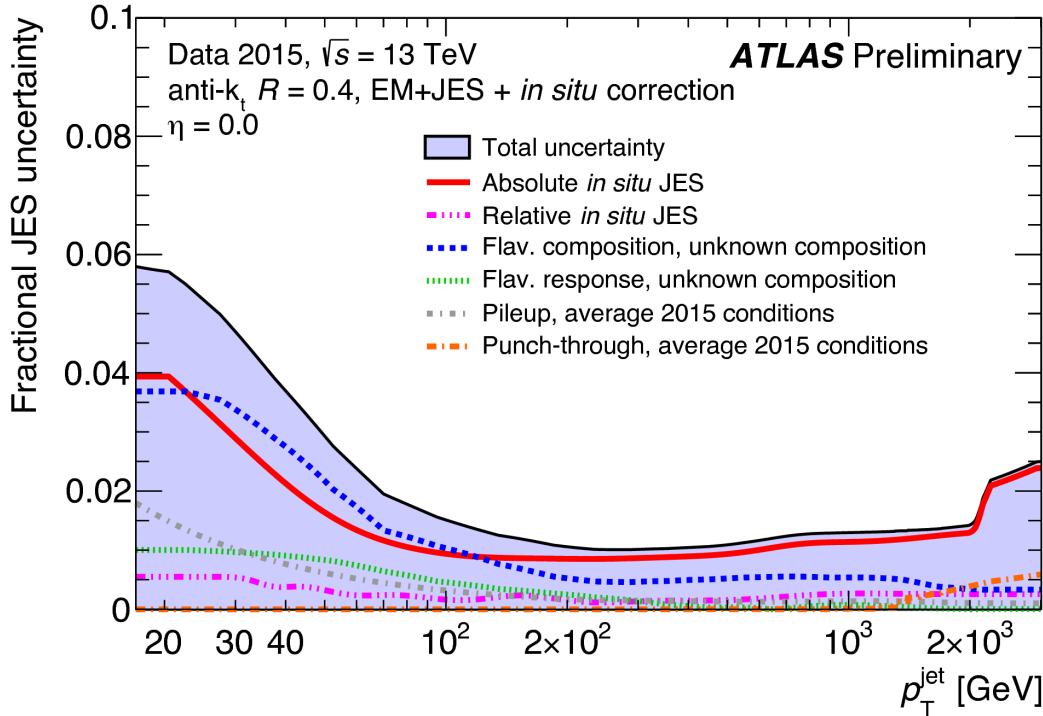


Figure 6.8: Combined jet energy scale uncertainty as a function of p_T at $\eta = 0$.



1289 first involves *ghost association*[TODO: cite](#). Ghost association runs the anti- k_T jet
 1290 clustering algorithm on a combined collection of the topoclusters and tracks. The
 1291 tracks *only* momenta are set to zero³; only the directional information is included.
 1292 As discussed above, the anti- k_T algorithm is “big to small”; this allows the tracks to be
 1293 associated to the “biggest” jet near them in (η, ϕ) . This method uniquely associates
 1294 each track to a jet, without changing the final jet kinematics.

1295 The JVT technique uses a combination of these track variables to determine the
 1296 likelihood that the jet originated at the primary vertex.

1297 This

³Well, not exactly zero, since zero momentum tracks wouldn't have a well-defined (η, ϕ) coordinate, but set to a value obeying $p_{T,\text{track}} << 400\text{MeV} = p_{\text{track,min}}$. This is the minimum momentum for a track to reach the ATLAS inner detector.

1298 **B-jets**

1299 **Missing Transverse Momentum**

1300 **TODO: cite paper/notes**

1301 Missing transverse momentum E_T^{miss} is a key observable in searches for new
1302 physics, especially in SUSY searches. However, E_T^{miss} is not a uniquely defined
1303 object when considered from the detector perspective (as compared to the Feynammn
1304 diagram), and it is useful to understand the choices that affect the performance of
1305 this observable in searches for new physics.

1306 **E_T^{miss} Definitions**

Hard objects refers to all physical objects as defined in the previous sections. The
 E_T^{miss} reconstruction procedure uses these hard objects and the *soft term* to provide
a value and direction of the missing transverse momentum. The $E_{x(y)}^{\text{miss}}$ components
are calculated as:

$$E_{x(y)}^{\text{miss}} = E_{x(y)}^{\text{miss, } e} + E_{x(y)}^{\text{miss, } \gamma} + E_{x(y)}^{\text{miss, jets}} + E_{x(y)}^{\text{miss, } \mu} + E_{x(y)}^{\text{miss, soft}}, \quad (6.5)$$

1307 where each value $E_{x(y)}^{\text{miss, } i}$ is the negative vectorial sum of the calibrated objects defined
1308 in the previous sections.

1309 For purposes of E_T^{miss} reconstruction, we must assign an ordering of *overlap*
1310 *removal*. This is to avoid double counting of the underlying primitive objects (clusters
1311 and tracks) which are inputs to the reconstruction of the physics objects. We resolve
1312 this in the following order : electrons, photons , jets and muons. This is motivated
1313 by the performance of the reconstruction of these objects in the calorimeters.

1314 The soft term $E_{x(y)}^{\text{miss, soft}}$ contains all of the primitive objects which are not
1315 associated to any of the reconstructed physics objects. Of course, we need to choose
1316 which primitive object to use. The primary choices which have been used within
1317 ATLAS are the *calorimeter-based soft term* (CST) and the *track-based soft term*

1318 (TST). Based on the soft term choice, we then call E_T^{miss} built with a CST (TST)
1319 soft term simply CST (TST) E_T^{miss} . An additional option, which will be important
1320 as pileup continues to increase, particle flow E_T^{miss} (PFlow E_T^{miss}).

1321 The CST E_T^{miss} was used for much of the early ATLAS data-taking. CST E_T^{miss} is
1322 built from the calibrated hard objects, combined with the calorimeter clusters which
1323 are *not* assigned to any of those hard objects. In the absence of pileup, it provides the
1324 best answer for the “true” E_T^{miss} in a given event, due to the impressive hermiticity of
1325 the calorimeters. Unfortunately, the calorimeters do not know “where” from where
1326 their energy deposition came, and thus CST is susceptible to drastically reduced
1327 performance as pileup is increased.

1328 TST E_T^{miss} is the standard for ATLAS searches as currently performed by ATLAS.
1329 TST E_T^{miss} is built by using the calibrated hard objects and the soft term is built from
1330 the tracks which are not assigned to any of those hard objects. In particular, due
1331 to the impressive track-vertex association efficiency, one chooses tracks which only
1332 come from the primary vertex. This drastically reduces the pileup contributions to
1333 the E_T^{miss} measurement. However, since the ID tracking system is unable to measure
1334 neutral objects, the TST E_T^{miss} is “wrong”. This bias is important to understand;
1335 however, in most searches for new physics, the soft E_T^{miss} is generally a small fraction
1336 of the total E_T^{miss} , and thus this bias is not particularly hurtful.

1337 PFlow E_T^{miss} uses the PFOs described above to build the E_T^{miss} . The PFOs which
1338 are assigned to hard objects are calibrated, and the PFOs which are not assigned
1339 to any hard object are added to the soft term. In this context, it is convenient to
1340 distinguish between “charged” and “neutral” PFOs. Charged PFOs can be seen as a
1341 topocluster which has an associated track, while neutral PFOs do not. This charged
1342 PFO is essentially a topocluster that we are “sure” comes from the primary vertex.
1343 The neutral PFOs are in the same status as the original topoclusters. Thus a “full”
1344 PFlow E_T^{miss} should have performance somewhere between TST E_T^{miss} and CST E_T^{miss} ⁴.

1345 A *charged* PFlow E_T^{miss} should for sanity be the same as TST.

1346 **E_T^{miss} Performance Metrics**

1347 The question is now straightforward; how do we compare these different algorithms?

1348 There are two main ingredients to investigate : the E_T^{miss} resolution and the E_T^{miss}

1349 scale. These components are measured in $Z \rightarrow \ell\ell$ and $W \rightarrow \ell\nu$ events. These two

1350 “standard candles” are well-m

1351 The E_T^{miss} resolution relies on the fact that the bulk of the distributions associated

1352 to $E_{x(y)}^{\text{miss}}$ are Gaussian distributed.

1353 **6.3 Maybe PFlow?**

⁴Naively, due to approximate isospin symmetry, about 2/3 of the hadrons will be charged and 1/3 will be neutral.

1354

Chapter 7

1355

The Recursive Jigsaw Technique

1356 Here you can write some introductory remarks about your chapter. I like to give each
1357 sentence its own line.

1358 When you need a new paragraph, just skip an extra line.

1359 **7.1 Razor variables**

1360 By using the asterisk to start a new section, I keep the section from appearing in the
1361 table of contents. If you want your sections to be numbered and to appear in the
1362 table of contents, remove the asterisk.

1363 **7.2 SuperRazor variables**

1364 **7.3 The Recursive Jigsaw Technique**

1365 **7.4 Variables used in the search for zero lepton**

1366 **SUSY**

1367

Chapter 8

1368

Title of Chapter 1

1369

Chapter 9

1370

Title of Chapter 1

1371 Here you can write some introductory remarks about your chapter. I like to give each
1372 sentence its own line.

1373 When you need a new paragraph, just skip an extra line.

1374 **9.1 Object reconstruction**

1375 **Photons, Muons, and Electrons**

1376 **Jets**

1377 **Missing transverse momentum**

1378 Probably longer, show some plots from the PUB note that we worked on

₁₃₇₉ **9.2 Signal regions**

₁₃₈₀ **Gluino signal regions**

₁₃₈₁ **Squark signal regions**

₁₃₈₂ **Compressed signal regions**

₁₃₈₃ **9.3 Background estimation**

₁₃₈₄ **Z vv**

₁₃₈₅ **W ev**

₁₃₈₆ **ttbar**

1387

Chapter 10

1388

Title of Chapter 1

1389 Here you can write some introductory remarks about your chapter. I like to give each
1390 sentence its own line.

1391 When you need a new paragraph, just skip an extra line.

1392 **10.1 Statistical Analysis**

1393 maybe to be moved to an appendix

1394 **10.2 Signal Region distributions**

1395 **10.3 Pull Plots**

1396 **10.4 Systematic Uncertainties**

1397 **10.5 Exclusion plots**

Conclusion

1399 Here you can write some introductory remarks about your chapter. I like to give each
1400 sentence its own line.

1401 When you need a new paragraph, just skip an extra line.

1402 **10.6 New Section**

1403 By using the asterisk to start a new section, I keep the section from appearing in the
1404 table of contents. If you want your sections to be numbered and to appear in the
1405 table of contents, remove the asterisk.

Bibliography

- 1407 [1] O. Perdereau, *Planck 2015 cosmological results*,
1408 AIP Conf. Proc. **1743** (2016) p. 050014.
- 1409 [2] N. Aghanim et al.,
1410 *Planck 2016 intermediate results. LI. Features in the cosmic microwave*
1411 *background temperature power spectrum and shifts in cosmological parameters*
1412 (2016), arXiv: [1608.02487 \[astro-ph.CO\]](https://arxiv.org/abs/1608.02487).
- 1413 [3] J. S. Schwinger,
1414 *On Quantum electrodynamics and the magnetic moment of the electron*,
1415 Phys. Rev. **73** (1948) p. 416.
- 1416 [4] S. Laporta and E. Remiddi,
1417 *The Analytical value of the electron (g-2) at order alpha**3 in QED*,
1418 Phys. Lett. **B379** (1996) p. 283, arXiv: [hep-ph/9602417 \[hep-ph\]](https://arxiv.org/abs/hep-ph/9602417).
- 1419 [5] S. Schael et al., *Precision electroweak measurements on the Z resonance*,
1420 Phys. Rept. **427** (2006) p. 257, arXiv: [hep-ex/0509008 \[hep-ex\]](https://arxiv.org/abs/hep-ex/0509008).
- 1421 [6] S. L. Glashow, *Partial Symmetries of Weak Interactions*,
1422 Nucl. Phys. **22** (1961) p. 579.
- 1423 [7] S. Weinberg, *A Model of Leptons*, Phys. Rev. Lett. **19** (1967) p. 1264.
- 1424 [8] A. Salam, *Weak and Electromagnetic Interactions*,
1425 Conf. Proc. **C680519** (1968) p. 367.
- 1426 [9] M. Gell-Mann, *A Schematic Model of Baryons and Mesons*,
1427 Phys. Lett. **8** (1964) p. 214.
- 1428 [10] G. Zweig, “An SU(3) model for strong interaction symmetry and its breaking.
1429 Version 2,” *DEVELOPMENTS IN THE QUARK THEORY OF HADRONS.*
1430 *VOL. 1. 1964 - 1978*, ed. by D. Lichtenberg and S. P. Rosen, 1964 p. 22,
1431 URL: <http://inspirehep.net/record/4674/files/cern-th-412.pdf>.

- 1432 [11] S. Weinberg, *Implications of Dynamical Symmetry Breaking*,
 1433 Phys. Rev. **D13** (1976) p. 974.
- 1434 [12] S. Weinberg, *Implications of Dynamical Symmetry Breaking: An Addendum*,
 1435 Phys. Rev. **D19** (1979) p. 1277.
- 1436 [13] E. Gildener, *Gauge Symmetry Hierarchies*, Phys. Rev. **D14** (1976) p. 1667.
- 1437 [14] L. Susskind,
 1438 *Dynamics of Spontaneous Symmetry Breaking in the Weinberg-Salam Theory*,
 1439 Phys. Rev. **D20** (1979) p. 2619.
- 1440 [15] S. P. Martin, “A Supersymmetry Primer,” 1997,
 1441 eprint: [arXiv:hep-ph/9709356](https://arxiv.org/abs/hep-ph/9709356).
- 1442 [16] V. C. Rubin and W. K. Ford Jr., *Rotation of the Andromeda Nebula from a*
 1443 *Spectroscopic Survey of Emission Regions*, Astrophys. J. **159** (1970) p. 379.
- 1444 [17] M. S. Roberts and R. N. Whitehurst,
 1445 “*The rotation curve and geometry of M31 at large galactocentric distances*,
 1446 Astrophys. J. **201** (1970) p. 327.
- 1447 [18] V. C. Rubin, N. Thonnard, and W. K. Ford Jr.,
 1448 *Rotational properties of 21 SC galaxies with a large range of luminosities and*
 1449 *radii, from NGC 4605 /R = 4kpc/ to UGC 2885 /R = 122 kpc/*,
 1450 Astrophys. J. **238** (1980) p. 471.
- 1451 [19] V. C. Rubin et al., *Rotation velocities of 16 SA galaxies and a comparison of*
 1452 *Sa, Sb, and SC rotation properties*, Astrophys. J. **289** (1985) p. 81.
- 1453 [20] A. Bosma,
 1454 *21-cm line studies of spiral galaxies. 2. The distribution and kinematics of*
 1455 *neutral hydrogen in spiral galaxies of various morphological types.*,
 1456 Astron. J. **86** (1981) p. 1825.
- 1457 [21] M. Persic, P. Salucci, and F. Stel, *The Universal rotation curve of spiral*
 1458 *galaxies: 1. The Dark matter connection*,
 1459 Mon. Not. Roy. Astron. Soc. **281** (1996) p. 27,
 1460 arXiv: [astro-ph/9506004](https://arxiv.org/abs/astro-ph/9506004) [[astro-ph](#)].
- 1461 [22] M. Lisanti, “Lectures on Dark Matter Physics,” 2016,
 1462 eprint: [arXiv:1603.03797](https://arxiv.org/abs/1603.03797).
- 1463 [23] H. Miyazawa, *Baryon Number Changing Currents*,
 1464 Prog. Theor. Phys. **36** (1966) p. 1266.

- 1465 [24] J.-L. Gervais and B. Sakita, *Generalizations of dual models*,
 1466 Nucl. Phys. **B34** (1971) p. 477.
- 1467 [25] J.-L. Gervais and B. Sakita,
 1468 *Field Theory Interpretation of Supergauges in Dual Models*,
 1469 Nucl. Phys. **B34** (1971) p. 632.
- 1470 [26] Yu. A. Golfand and E. P. Likhtman, *Extension of the Algebra of Poincare
 1471 Group Generators and Violation of p Invariance*,
 1472 JETP Lett. **13** (1971) p. 323, [Pisma Zh. Eksp. Teor. Fiz. 13, 452 (1971)].
- 1473 [27] A. Neveu and J. H. Schwarz, *Factorizable dual model of pions*,
 1474 Nucl. Phys. **B31** (1971) p. 86.
- 1475 [28] A. Neveu and J. H. Schwarz, *Quark Model of Dual Pions*,
 1476 Phys. Rev. **D4** (1971) p. 1109.
- 1477 [29] D. V. Volkov and V. P. Akulov, *Is the Neutrino a Goldstone Particle?*
 1478 Phys. Lett. **B46** (1973) p. 109.
- 1479 [30] J. Wess and B. Zumino,
 1480 *A Lagrangian Model Invariant Under Supergauge Transformations*,
 1481 Phys. Lett. **B49** (1974) p. 52.
- 1482 [31] A. Salam and J. A. Strathdee, *Supersymmetry and Nonabelian Gauges*,
 1483 Phys. Lett. **B51** (1974) p. 353.
- 1484 [32] S. Ferrara, J. Wess, and B. Zumino, *Supergauge Multiplets and Superfields*,
 1485 Phys. Lett. **B51** (1974) p. 239.
- 1486 [33] J. Wess and B. Zumino, *Supergauge Transformations in Four-Dimensions*,
 1487 Nucl. Phys. **B70** (1974) p. 39.
- 1488 [34] J. D. Lykken, “Introduction to supersymmetry,” *Fields, strings and duality. Proceedings, Summer School, Theoretical Advanced Study Institute in Elementary Particle Physics, TASI’96, Boulder, USA, June 2-28, 1996*,
 1489 p. 85, arXiv: [hep-th/9612114 \[hep-th\]](https://arxiv.org/abs/hep-th/9612114),
 1490 URL: http://lss.fnal.gov/cgi-bin/find_paper.pl?pub-96-445-T.
- 1493 [35] A. Kobakhidze, “Intro to SUSY,” 2016, URL:
 1494 <https://indico.cern.ch/event/443176/page/5225-pre-susy-programme>.
- 1495 [36] G. R. Farrar and P. Fayet, *Phenomenology of the Production, Decay, and
 1496 Detection of New Hadronic States Associated with Supersymmetry*,
 1497 Phys. Lett. **B76** (1978) p. 575.

- 1498 [37] ATLAS Collaboration,
 1499 *Search for the electroweak production of supersymmetric particles in*
 1500 *$\sqrt{s} = 8 \text{ TeV}$ pp collisions with the ATLAS detector,*
 1501 *Phys. Rev. D* **93** (2016) p. 052002, arXiv: [1509.07152 \[hep-ex\]](#).
- 1502 [38] ATLAS Collaboration, *Summary of the searches for squarks and gluinos using*
 1503 *$\sqrt{s} = 8 \text{ TeV}$ pp collisions with the ATLAS experiment at the LHC,*
 1504 *JHEP* **10** (2015) p. 054, arXiv: [1507.05525 \[hep-ex\]](#).
- 1505 [39] ATLAS Collaboration, *ATLAS Run 1 searches for direct pair production of*
 1506 *third-generation squarks at the Large Hadron Collider,*
 1507 *Eur. Phys. J. C* **75** (2015) p. 510, arXiv: [1506.08616 \[hep-ex\]](#).
- 1508 [40] CMS Collaboration,
 1509 *Search for supersymmetry with razor variables in pp collisions at $\sqrt{s} = 7 \text{ TeV}$,*
 1510 *Phys. Rev. D* **90** (2014) p. 112001, arXiv: [1405.3961 \[hep-ex\]](#).
- 1511 [41] CMS Collaboration, *Inclusive search for supersymmetry using razor variables*
 1512 *in pp collisions at $\sqrt{s} = 7 \text{ TeV}$, Phys. Rev. Lett.* **111** (2013) p. 081802,
 1513 arXiv: [1212.6961 \[hep-ex\]](#).
- 1514 [42] CMS Collaboration, *Search for Supersymmetry in pp Collisions at 7 TeV in*
 1515 *Events with Jets and Missing Transverse Energy,*
 1516 *Phys. Lett. B* **698** (2011) p. 196, arXiv: [1101.1628 \[hep-ex\]](#).
- 1517 [43] CMS Collaboration, *Search for Supersymmetry at the LHC in Events with*
 1518 *Jets and Missing Transverse Energy, Phys. Rev. Lett.* **107** (2011) p. 221804,
 1519 arXiv: [1109.2352 \[hep-ex\]](#).
- 1520 [44] CMS Collaboration, *Search for supersymmetry in hadronic final states using*
 1521 *M_{T2} in pp collisions at $\sqrt{s} = 7 \text{ TeV}$, JHEP* **10** (2012) p. 018,
 1522 arXiv: [1207.1798 \[hep-ex\]](#).
- 1523 [45] CMS Collaboration, *Searches for supersymmetry using the M_{T2} variable in*
 1524 *hadronic events produced in pp collisions at 8 TeV, JHEP* **05** (2015) p. 078,
 1525 arXiv: [1502.04358 \[hep-ex\]](#).
- 1526 [46] CMS Collaboration, *Search for new physics with the M_{T2} variable in all-jets*
 1527 *final states produced in pp collisions at $\sqrt{s} = 13 \text{ TeV}$ (2016),*
 1528 arXiv: [1603.04053 \[hep-ex\]](#).
- 1529 [47] ATLAS Collaboration, *Multi-channel search for squarks and gluinos in*
 1530 *$\sqrt{s} = 7 \text{ TeV}$ pp collisions with the ATLAS detector at the LHC,*
 1531 *Eur. Phys. J. C* **73** (2013) p. 2362, arXiv: [1212.6149 \[hep-ex\]](#).

- 1532 [48] Y. Grossman, “Introduction to the SM,” 2016, URL: <https://indico.fnal.gov/sessionDisplay.py?sessionId=3&confId=11505#20160811>.
- 1533
- 1534 [49] ()�.
- 1535 [50] P. W. Higgs, *Broken Symmetries and the Masses of Gauge Bosons*,
1536 *Phys. Rev. Lett.* **13** (1964) p. 508.
- 1537 [51] ATLAS Collaboration, *Observation of a new particle in the search for the*
1538 *Standard Model Higgs boson with the ATLAS detector at the LHC*,
1539 *Phys. Lett. B* **716** (2012) p. 1, arXiv: [1207.7214 \[hep-ex\]](https://arxiv.org/abs/1207.7214).
- 1540 [52] CMS Collaboration, *Observation of a new boson at a mass of 125 GeV with*
1541 *the CMS experiment at the LHC*, *Phys. Lett. B* **716** (2012) p. 30,
1542 arXiv: [1207.7235 \[hep-ex\]](https://arxiv.org/abs/1207.7235).
- 1543 [53] A. Chodos et al., *A New Extended Model of Hadrons*,
1544 *Phys. Rev. D* **9** (1974) p. 3471.
- 1545 [54] A. Chodos et al., *Baryon Structure in the Bag Theory*,
1546 *Phys. Rev. D* **10** (1974) p. 2599.
- 1547 [55] J. C. Collins, D. E. Soper, and G. F. Sterman,
1548 *Factorization of Hard Processes in QCD*,
1549 *Adv. Ser. Direct. High Energy Phys.* **5** (1989) p. 1,
1550 arXiv: [hep-ph/0409313 \[hep-ph\]](https://arxiv.org/abs/hep-ph/0409313).
- 1551 [56] K. A. Olive et al., *Review of Particle Physics*,
1552 *Chin. Phys. C* **38** (2014) p. 090001.
- 1553 [57] N. Cabibbo, *Unitary Symmetry and Leptonic Decays*,
1554 *Phys. Rev. Lett.* **10** (1963) p. 531, [,648(1963)].
- 1555 [58] M. Kobayashi and T. Maskawa,
1556 *CP Violation in the Renormalizable Theory of Weak Interaction*,
1557 *Prog. Theor. Phys.* **49** (1973) p. 652.
- 1558 [59] W. F. L. Hollik, *Radiative Corrections in the Standard Model and their Role*
1559 *for Precision Tests of the Electroweak Theory*,
1560 *Fortsch. Phys.* **38** (1990) p. 165.
- 1561 [60] D. Yu. Bardin et al.,
1562 *ELECTROWEAK RADIATIVE CORRECTIONS TO DEEP INELASTIC*
1563 *SCATTERING AT HERA! CHARGED CURRENT SCATTERING*,
1564 *Z. Phys. C* **44** (1989) p. 149.

- 1565 [61] D. C. Kennedy et al., *Electroweak Cross-Sections and Asymmetries at the Z0*,
 1566 Nucl. Phys. **B321** (1989) p. 83.
- 1567 [62] A. Sirlin, *Radiative Corrections in the SU(2)-L x U(1) Theory: A Simple*
 1568 *Renormalization Framework*, Phys. Rev. **D22** (1980) p. 971.
- 1569 [63] S. Fanchiotti, B. A. Kniehl, and A. Sirlin,
 1570 *Incorporation of QCD effects in basic corrections of the electroweak theory*,
 1571 Phys. Rev. **D48** (1993) p. 307, arXiv: [hep-ph/9212285](https://arxiv.org/abs/hep-ph/9212285) [hep-ph].
- 1572 [64] C. Quigg, “Cosmic Neutrinos,” *Proceedings, 35th SLAC Summer Institute on*
 1573 *Particle Physics: Dark matter: From the cosmos to the Laboratory (SSI 2007):*
 1574 *Menlo Park, California, July 30- August 10, 2007*, 2008,
 1575 arXiv: [0802.0013](https://arxiv.org/abs/0802.0013) [hep-ph],
 1576 URL: http://lss.fnal.gov/cgi-bin/find_paper.pl?conf=07-417.
- 1577 [65] S. R. Coleman and J. Mandula, *All Possible Symmetries of the S Matrix*,
 1578 Phys. Rev. **159** (1967) p. 1251.
- 1579 [66] R. Haag, J. T. Lopuszanski, and M. Sohnius,
 1580 *All Possible Generators of Supersymmetries of the s Matrix*,
 1581 Nucl. Phys. **B88** (1975) p. 257.
- 1582 [67] A. Salam and J. A. Strathdee, *On Superfields and Fermi-Bose Symmetry*,
 1583 Phys. Rev. **D11** (1975) p. 1521.
- 1584 [68] S. Dimopoulos and H. Georgi, *Softly Broken Supersymmetry and SU(5)*,
 1585 Nucl. Phys. **B193** (1981) p. 150.
- 1586 [69] S. Dimopoulos, S. Raby, and F. Wilczek,
 1587 *Supersymmetry and the Scale of Unification*, Phys. Rev. **D24** (1981) p. 1681.
- 1588 [70] L. E. Ibanez and G. G. Ross,
 1589 *Low-Energy Predictions in Supersymmetric Grand Unified Theories*,
 1590 Phys. Lett. **B105** (1981) p. 439.
- 1591 [71] W. J. Marciano and G. Senjanovic,
 1592 *Predictions of Supersymmetric Grand Unified Theories*,
 1593 Phys. Rev. **D25** (1982) p. 3092.
- 1594 [72] L. Girardello and M. T. Grisaru, *Soft Breaking of Supersymmetry*,
 1595 Nucl. Phys. **B194** (1982) p. 65.

- 1596 [73] D. J. H. Chung et al.,
 1597 *The Soft supersymmetry breaking Lagrangian: Theory and applications*,
 1598 *Phys. Rept.* **407** (2005) p. 1, arXiv: [hep-ph/0312378 \[hep-ph\]](#).
- 1599 [74] J. Hisano et al., *Lepton flavor violation in the supersymmetric standard model*
 1600 *with seesaw induced neutrino masses*, *Phys. Lett.* **B357** (1995) p. 579,
 1601 arXiv: [hep-ph/9501407 \[hep-ph\]](#).
- 1602 [75] F. Gabbiani et al., *A Complete analysis of FCNC and CP constraints in*
 1603 *general SUSY extensions of the standard model*,
 1604 *Nucl. Phys.* **B477** (1996) p. 321, arXiv: [hep-ph/9604387 \[hep-ph\]](#).
- 1605 [76] F. Gabbiani and A. Masiero, *FCNC in Generalized Supersymmetric Theories*,
 1606 *Nucl. Phys.* **B322** (1989) p. 235.
- 1607 [77] J. S. Hagelin, S. Kelley, and T. Tanaka, *Supersymmetric flavor changing*
 1608 *neutral currents: Exact amplitudes and phenomenological analysis*,
 1609 *Nucl. Phys.* **B415** (1994) p. 293.
- 1610 [78] J. S. Hagelin, S. Kelley, and V. Ziegler, *Using gauge coupling unification and*
 1611 *proton decay to test minimal supersymmetric SU(5)*,
 1612 *Phys. Lett.* **B342** (1995) p. 145, arXiv: [hep-ph/9406366 \[hep-ph\]](#).
- 1613 [79] D. Choudhury et al.,
 1614 *Constraints on nonuniversal soft terms from flavor changing neutral currents*,
 1615 *Phys. Lett.* **B342** (1995) p. 180, arXiv: [hep-ph/9408275 \[hep-ph\]](#).
- 1616 [80] R. Barbieri and L. J. Hall, *Signals for supersymmetric unification*,
 1617 *Phys. Lett.* **B338** (1994) p. 212, arXiv: [hep-ph/9408406 \[hep-ph\]](#).
- 1618 [81] B. de Carlos, J. A. Casas, and J. M. Moreno,
 1619 *Constraints on supersymmetric theories from mu —> e gamma*,
 1620 *Phys. Rev.* **D53** (1996) p. 6398, arXiv: [hep-ph/9507377 \[hep-ph\]](#).
- 1621 [82] J. A. Casas and S. Dimopoulos,
 1622 *Stability bounds on flavor violating trilinear soft terms in the MSSM*,
 1623 *Phys. Lett.* **B387** (1996) p. 107, arXiv: [hep-ph/9606237 \[hep-ph\]](#).
- 1624 [83] C. Borschensky et al., *Squark and gluino production cross sections in pp*
 1625 *collisions at $\sqrt{s} = 13, 14, 33$ and 100 TeV*, *Eur. Phys. J.* **C74** (2014) p. 3174,
 1626 arXiv: [1407.5066 \[hep-ph\]](#).
- 1627 [84] M. Klasen, M. Pohl, and G. Sigl, *Indirect and direct search for dark matter*,
 1628 *Prog. Part. Nucl. Phys.* **85** (2015) p. 1, arXiv: [1507.03800 \[hep-ph\]](#).

- 1629 [85] L. Evans and P. Bryant, *LHC Machine*, JINST **3** (2008) S08001.
- 1630 [86] V. Shiltsev, “Accelerator Physics and Technology,” 2016,
1631 URL: [https://indico.fnal.gov/sessionDisplay.py?sessionId=3&](https://indico.fnal.gov/sessionDisplay.py?sessionId=3&confId=11505#20160811)
1632 [confId=11505#20160811](#).
- 1633 [87] *LEP design report*, Copies shelved as reports in LEP, PS and SPS libraries,
1634 Geneva: CERN, 1984, URL: <https://cds.cern.ch/record/102083>.
- 1635 [88] ATLAS Collaboration,
1636 *The ATLAS Experiment at the CERN Large Hadron Collider*,
1637 JINST **3** (2008) S08003.
- 1638 [89] ATLAS Collaboration, *2015 start-up trigger menu and initial performance*
1639 *assessment of the ATLAS trigger using Run-2 data*,
1640 ATL-DAQ-PUB-2016-001, 2016,
1641 URL: <https://cds.cern.ch/record/2136007/>.
- 1642 [90] ATLAS Collaboration,
1643 *Electron reconstruction and identification efficiency measurements with the*
1644 *ATLAS detector using the 2011 LHC proton–proton collision data*,
1645 Eur. Phys. J. C **74** (2014) p. 2941, arXiv: [1404.2240 \[hep-ex\]](https://arxiv.org/abs/1404.2240).
- 1646 [91] ATLAS Collaboration, *Topological cell clustering in the ATLAS calorimeters*
1647 *and its performance in LHC Run 1* (2016), arXiv: [1603.02934 \[hep-ex\]](https://arxiv.org/abs/1603.02934).
- 1648 [92] M. Aaboud et al., *Measurement of the photon identification efficiencies with*
1649 *the ATLAS detector using LHC Run-1 data* (2016),
1650 arXiv: [1606.01813 \[hep-ex\]](https://arxiv.org/abs/1606.01813).
- 1651 [93] ATLAS Collaboration, *Electron and photon energy calibration with the*
1652 *ATLAS detector using LHC Run 1 data*, Eur. Phys. J. C **74** (2014) p. 3071,
1653 arXiv: [1407.5063 \[hep-ex\]](https://arxiv.org/abs/1407.5063).
- 1654 [94] ATLAS Collaboration, *Muon reconstruction performance of the ATLAS*
1655 *detector in proton–proton collision data at $\sqrt{s} = 13 \text{ TeV}$* (2016),
1656 arXiv: [1603.05598 \[hep-ex\]](https://arxiv.org/abs/1603.05598).
- 1657 [95] S. D. Ellis and D. E. Soper,
1658 *Successive combination jet algorithm for hadron collisions*,
1659 Phys. Rev. **D48** (1993) p. 3160, arXiv: [hep-ph/9305266 \[hep-ph\]](https://arxiv.org/abs/hep-ph/9305266).
- 1660 [96] M. Cacciari and G. P. Salam, *Dispelling the N^3 myth for the k_t jet-finder*,
1661 Phys. Lett. **B641** (2006) p. 57, arXiv: [hep-ph/0512210 \[hep-ph\]](https://arxiv.org/abs/hep-ph/0512210).

- 1662 [97] M. Cacciari, G. P. Salam, and G. Soyez,
1663 *The Anti- $k(t)$ jet clustering algorithm*, JHEP **04** (2008) p. 063,
1664 arXiv: [0802.1189 \[hep-ph\]](https://arxiv.org/abs/0802.1189).

1665

The Standard Model

1666 In this appendix, we provide a brief overview of the basic ingredients involved in
1667 construction of the Standard Model Lagrangian : quantum field theory, symmetries,
1668 and symmetry breaking.

1669 Quantum Field Theory

1670 **TODO: cite Yuval's lectures and notes somehow**

1671 In this section, we provide a brief overview of the necessary concepts from
1672 Quantum Field Theory (QFT).

1673 In modern physics, the laws of nature are described by the “action” S , with the
1674 imposition of the principle of minimum action. **TODO: cite** The action is the integral
1675 over the spacetime coordinates of the “Lagrangian density” \mathcal{L} , or Lagrangian for
1676 short. The Lagrangian is a function of “fields”; general fields will be called $\phi(x^\mu)$,
1677 where the indices μ run over the space-time coordinates. We can then write the action
1678 S as

$$S = \int d^4x \mathcal{L}[\phi_i(x^\mu), \partial_\mu \phi_i(x^\mu)] \quad (10.1)$$

1679 where we have an additional summation over i (of the different fields). Generally,
1680 we impose the following constraints on the Lagrangian :

1681 1. Translational invariance - The Lagrangian is only a function of the fields ϕ and
1682 their derivatives $\partial_\mu \phi$

1683 2. Locality - The Lagrangian is only a function of one point x_μ in spacetime.

1684 3. Reality condition - The Lagrangian is real to conserve probability.

1685 4. Lorentz invariance - The Lagrangian is invariant under the Poincarégroup of
1686 spacetime.

1687 5. Analyticity - The Lagrangian is an analytical function of the fields; this is to
1688 allow the use of perturbation theory.

1689 6. Invariance and Naturalness - The Lagrangian is invariant under some internal
1690 symmetry groups; in fact, the Lagrangian will have *all* terms allowed by the
1691 imposed symmetry groups. **TODO: maybe add in ref here**

1692 7. Renormalizability - The Lagrangian will be renormalizable - in practice, this
1693 means there will not be terms with more than power 4 in the fields.

1694 The key item from the point of view of this thesis is that of “Invariance and
1695 Natural”. We impose a set of “symmetries” and then our Lagrangian is the most
1696 general which is allowed by those symmetries.

1697 **Symmetries**

1698 Symmetries can be seen as the fundamental guiding concept of modern physics.
1699 Symmetries are described by “groups”. **TODO: cite?**. To illustrate the importance
1700 of symmetries and their mathematical description, groups, we start here with two of
1701 the simplest and most useful examples : \mathbb{Z}_2 and $U(1)$.

1702 **\mathbb{Z}_2 symmetry**

1703 \mathbb{Z}_2 symmetry is the simplest example of a “discrete” symmetry. Consider the most
1704 general Lagrangian of a single real scalar field $\phi(x_\mu)$

$$\mathcal{L}_\phi = \frac{1}{2}\partial_\mu\phi\partial^\mu\phi - \frac{m^2}{2}\phi^2 - \frac{\mu}{2\sqrt{2}}\phi^3 - \lambda\phi^4 \quad (10.2)$$

Now we *impose* the symmetry

$$\mathcal{L}(\phi) = \mathcal{L}(-\phi) \quad (10.3)$$

1705 This has the effect of restricting the allowed terms of the Lagrangian. In particular,
 1706 we can see the term $\phi^3 \rightarrow -\phi^3$ under the symmetry transformation, and thus must
 1707 be disallowed by this symmetry. This means under the imposition of this particular
 1708 symmetry, our Lagrangian should be rewritten as

$$\mathcal{L}_\phi = \frac{1}{2}\partial_\mu\phi\partial^\mu\phi - \frac{m^2}{2}\phi^2 - \lambda\phi^4 \quad (10.4)$$

1709 The effect of this symmetry is that the total number of ϕ particles can only change
 1710 by even numbers, since the only interaction term $\lambda\phi^4$ is an even power of the field.
 1711 This symmetry is often imposed in supersymmetric theories, as we will see in Chapter
 1712 3.

1713 **$U(1)$ symmetry**

1714 $U(1)$ is the simplest example of a continuous (or *Lie*) group. Now consider a theory
 1715 with a single complex scalar field $\phi = \text{Re } \phi + i \text{Im } \phi$

$$\mathcal{L}_\phi = \delta_{i,j} \frac{1}{2}\partial_\mu\phi_i\partial^\mu\phi_j - \frac{m^2}{2}\phi_i\phi_j - \frac{\mu}{2\sqrt{2}}\phi_i\phi_j\phi_k\phi_l - \lambda\phi_i\phi_j\phi_k\phi_l \quad (10.5)$$

1716 where $i, j, k, l = \text{Re}, \text{Im}$. In this case, we impose the following $U(1)$ symmetry
 1717 : $\phi \rightarrow e^{i\theta}, \phi^* \rightarrow e^{-i\theta}$. We see immediately that this again disallows the third-order
 1718 terms, and we can write a theory of a complex scalar field with $U(1)$ symmetry as

$$\mathcal{L}_\phi = \partial_\mu\phi\partial^\mu\phi^* - \frac{m^2}{2}\phi\phi^* - \lambda(\phi\phi^*)^2 \quad (10.6)$$

1719 **Local symmetries**

1720 The two examples considered above are “global” symmetries in the sense that the
1721 symmetry transformation does not depends on the spacetime coordinate x_μ . We know
1722 look at local symmetries; in this case, for example with a local $U(1)$ symmetry, the
1723 transformation has the form $\phi(x_\mu) \rightarrow e^{i\theta(x_\mu)}\phi(x_\mu)$. These symmetries are also known
1724 as “gauge” symmetries; all symmetries of the Standard Model are gauge symmetries.

There are wide-ranging consequences to the imposition of local symmetries. To begin, we note that the derivative terms of the Lagrangian 10.2 are *not* invariant under a local symmetry transformation

$$\partial_\mu \phi(x_\mu) \rightarrow \partial_\mu(e^{i\theta(x_\mu)}\phi(x_\mu)) = (1 + i\theta(x_\mu))e^{i\theta(x_\mu)}\phi(x_\mu) \quad (10.7)$$

1725 **TODO: GET THIS RIGHT**

1726 This leads us to note that the kinetic terms of the Lagrangian are also not invariant
1727 under a gauge symmetry. This would lead to a model with no dynamics, which is
1728 clearly unsatisfactory.

1729 Let us take inspiration from the case of global symmetries. We need to define a
1730 so-called “covariant” derivative D^μ such that

$$D^\mu \phi \rightarrow e^{iq\theta(x^\mu)D^\mu}\phi \quad (10.8)$$

$$D^\mu \phi^* \rightarrow e^{-iq\theta(x^\mu)D^\mu}\phi^* \quad (10.9)$$

$$(10.10)$$

1731 Since ϕ and ϕ^* transforms with the opposite phase, this will lead the invariance
1732 of the Lagrangian under our local gauge transformation. This D^μ is of the following
1733 form

$$D^\mu = \partial_\mu - igqA^\mu \quad (10.11)$$

1734 where A^μ is a vector field we introduce with the transformation law

$$A^\mu \rightarrow A^\mu - \frac{1}{g} \partial_\mu \theta \quad (10.12)$$

1735 and g is the coupling constant associated to vector field. This vector field A^μ is
1736 also known as a “gauge” field.

1737 Since we need to add all allowed terms to the Lagrangian, we define

$$F^{\mu\nu} = A^\mu A^\nu - A^\nu A^\mu \quad (10.13)$$

1738 and then we must also add the kinetic term :

$$\mathcal{L}_{\text{gauge}} = -\frac{1}{4} F^{\mu\nu} F_{\mu\nu} \quad (10.14)$$

1739 The most general renormalizable Lagrangian with fermion and scalar fields can
1740 be written in the following form

$$\mathcal{L} = \mathcal{L}_{\text{kin}} + \mathcal{L}_\phi + \mathcal{L}_\psi + \mathcal{L}_{\text{Yukawa}} \quad (10.15)$$

1741 Symmetry breaking and the Higgs mechanism

1742 Here we view some examples of symmetry breaking. We investigate breaking of a
1743 global $U(1)$ symmetry and a local $U(1)$ symmetry. The SM will break the electroweak
1744 symmetry $SU(2)xU(1)$, and in Chapter 3 we will see how supersymmetry must also
1745 be broken.

1746 There are two ideas of symmetry breaking

- 1747 • Explicit symmetry breaking by a small parameter - in this case, we have a small
1748 parameter which breaks an “approximate” symmetry of our Lagrangian. An
1749 example would be the theory of the single scalar field 10.2, when $\mu \ll m^2$ and

1750 $\mu \ll \lambda$. In this case, we can often ignore the small term when considering
 1751 low-energy processes.

1752 • Spontaneous symmetry breaking (SSB) - spontaneous symmetry breaking
 1753 occurs when the Lagrangian is symmetric with respect to a given symmetry
 1754 transformation, but the ground state of the theory is *not* symmetric with respect
 1755 to that transformation. This can have some fascinating consequences, as we
 1756 will see in the following examples

1757 Symmetry breaking a

1758 **U(1) global symmetry breaking**

Consider the theory of a complex scalar field under the $U(1)$ symmetry, or the transformation

$$\phi \rightarrow e^{i\theta} \phi \quad (10.16)$$

The Lagrangian for this theory is

$$\mathcal{L} = \partial^\mu \phi^\dagger \partial_\mu \phi + \frac{\mu^2}{2} \phi^\dagger \phi + \frac{\lambda}{4} (\phi^\dagger \phi)^2 \quad (10.17)$$

Let us write this theory in terms of two scalar fields, h and ξ : $\phi = (h + i\xi)/\sqrt{2}$.

The Lagrangian can then be written as

$$\mathcal{L} = \partial^\mu h \partial_\mu h + \partial^\mu \xi d\mu \xi - \frac{\mu^2}{2} (h^2 + \xi^2) - \frac{\lambda}{4} (h^2 + \xi^2)^2 \quad (10.18)$$

First, note that the theory is only stable when $\lambda > 0$. To understand the effect of SSB, we now enforce that $\mu^2 < 0$, and define $v^2 = -\mu^2/\lambda$. We can then write the scalar potential of this theory as :

$$V(\phi) = \lambda(\phi^\dagger \phi - v^2/2)^2 \quad (10.19)$$

Minimizing this equation with respect to ϕ , we can see that the “vacuum expectation value” of the theory is

$$2 < \phi^\dagger \phi > = < h^2 + \xi^2 > = v^2 \quad (10.20)$$

1759 We now reach the “breaking” point of this procedure. In the (h, ξ) plane, the
 1760 minima form a circle of radius v . We are free to choose any of these minima to expand
 1761 our Lagrangian around; the physics is not affected by this choice. For convenience,
 1762 choose $\langle h \rangle = v, \langle \xi^2 \rangle = 0$.

Now, let us define $h' = h - v, \xi' = \xi$ with VEVs $\langle h' \rangle = 0, \langle \xi' \rangle = 0$. We can
 then write our spontaneously broken Lagrangian in the form

$$\mathcal{L} = \frac{1}{2}\partial_\mu h'\partial^\mu h' + \frac{1}{2}\partial_\mu \xi'\partial^\mu \xi' - \lambda v^2 h'^2 - \lambda v h'(h'^2 + \xi'^2) - \lambda(h'^2 + \xi'^2)^2 \quad (10.21)$$